DOI:10.15774/PPKE.ITK.2018.009

The role of intramolecular vibrations in photosynthetic exciton energy transfer

Imre Benedek Juhász

Supervisor:
Dr. Árpád Csurgay

This dissertation is submitted for the degree of
Doctor of Philosophy

Pázmány Péter Catholic University
Faculty of Information Technology and Bionics
Roska Tamás Doctoral School of Sciences and Technology

Budapest, 2017

DOI:10.15774/PPKE.ITK.2018.009

"Then God said: Let there be light, and there was light.
God saw that the light was good."

(Genesis 1:3–4)

DOI:10.15774/PPKE.ITK.2018.009

Abstract

More and more theoretical and experimental results suggest that quantum effects, such as quantum coherence and quantum entanglement, play a significant role in certain physiological functions—at room temperature, in the vibrant medium comprised of living matter. Among these physiological functions, photosynthetic exciton energy transfer receives special attention. During this process, the energy of the photons that has been absorbed by the antenna complexes is transferred to the reaction center with high efficiency.

The comprehension of the process is also important from the engineering point of view, since the principles learned from nature might be applied later during the design of artificial photosynthetic systems and bionic sensors.

Former models of the photosynthetic exciton energy transfer focused exclusively on the electronic states of the participating molecules. In recent years, however, the role of intramolecular vibrations attracted increasing interest, and numerous papers concluded that these vibrations can enhance the exciton energy transfer. To study further how the intramolecular vibrational modes influence the dynamics and the efficiency of the transfer process, I elaborated a new, Lindblad-type model, and implemented a simulator program. Using dimer and heptamer model arrangements, I confirmed that undamped intramolecular vibrational modes can improve the exciton energy transfer. In addition, I demonstrated that the damping of these vibrational modes (*i.e.,* vibrational relaxation induced by the environment) can considerably and robustly increase the transfer efficiency further in wide ranges of the investigated parameters.

DOI:10.15774/PPKE.ITK.2018.009

Összefoglalás

Egyre több elméleti és kísérleti eredmény utal arra, hogy az olyan kvantumeffektusok, mint a kvantumkoherencia és a kvantumösszefonódás, fontos szerepet játszanak bizonyos élettani működésekben – szobahőmérsékleten, az élő anyag alkotta nyüzsgő közegben. Ezek között az élettani jelenségek között kiemelt érdeklődés övezi a fotoszintetikus excitonenergia-transzfert. E folyamat során az antenna komplexek által elnyelt fotonok energiája nagy hatékonysággal a reakciócentrumba szállítódik.

A folyamat megértése mérnöki szempontból is fontos, hiszen a természettől eltanult elveket később esetleg felhasználhatjuk mesterséges fotoszintetitus rendszerek és bionikus szenzorok tervezése során.

A fotoszintetikus excitonenergia-transzfer korábbi modelljei a résztvevő molekuláknak kizárólag az elektronikus állapotaira összpontosítottak. Az elmúlt években azonban a molekulákon belüli vibrációkra növekvő figyelem irányult, és számos cikk jutott arra a következtetésre, hogy ezek a rezgések fokozhatják az excitonenergia-transzfert. Abból a célból, hogy tovább tanulmányozzam az intramolekuláris vibrációs módusoknak a transzfer folyamat dinamikájára és hatékonyságára kifejtett hatását, kidolgoztam egy új, Lindblad-típusú modellt, illetve készítettem egy szimulátor programot. Dimer és heptamer modellelrendezéseket használva megerősítettem, hogy a csillapítatlan vibrációs módusok javíthatják az excitonenergia-transzfert. Megmutattam továbbá, hogy ezen vibrációs módusok csillapítása (azaz a környezet hatására végbemenő vibrációs relaxáció) jelentős mértékben és robusztus módon tovább fokozhatja a transzfer hatékonyságát, mégpedig a vizsgált paraméterek széles tartományában.

DOI:10.15774/PPKE.ITK.2018.009

Acknowledgements

I thank my supervisor, *Professor Árpád Csurgay,* for the many years of guidance and even more for his friendship. I am grateful for our long and deep conversations. I am also grateful to his wife, *Ildikó Csurgay*, who always had a kind word for me and even hosted me in their home.

I thank *Professor Tamás Roska* and *Professor Péter Szolgay,* former and present heads of the Doctoral School, for creating the technical and financial background of the research work, as well as the administrative staff of the Faculty, especially *Tivadarné Vida*, for their assistance.

I thank *Ádám Fekete, Máté Handbauer, Gergely Csány, József Mák, Ádám Nagy,* and *Zoltán Rácz* for the inspiring discussions and common thinking about physics, as well as *Mátyás Jani, János Juhász,* and *Attila Jády* for their fellowship. I am also grateful to the students whom I taught as a demonstrator. I enjoyed the common work, and I learned a lot in its course.

Most of all, I am grateful to my *Mother* and *Father*, who supported me all along with their love and care.

This research has been partially supported by the European Union, co-financed by the European Social Fund (EFOP-3.6.3-VEKOP-16-2017-00002).

DOI:10.15774/PPKE.ITK.2018.009

Contents

DOI:10.15774/PPKE.ITK.2018.009

DOI:10.15774/PPKE.ITK.2018.009

DOI:10.15774/PPKE.ITK.2018.009

List of Figures

DOI:10.15774/PPKE.ITK.2018.009

DOI:10.15774/PPKE.ITK.2018.009

List of Tables

DOI:10.15774/PPKE.ITK.2018.009

List of Abbreviations

ATP	adenosine triphosphate
BChl	bacteriochlorophyll
DNA	deoxyribonucleic acid
ENAQT	environment-assisted quantum transport
FMO	Fenna–Matthews–Olson (complex)
HEOM	hierarchical equation of motion
NAD^+	nicotinamide adenine dinucleotide (oxidized form)
$NADP^+$	nicotinamide adenine dinucleotide phosphate (oxidized form)
QuTiP	Quantum Toolbox in Python
RC	reaction center
sim(s).	simulation(s)
VREEET	vibrational-relaxation-enhanced exciton energy transfer

DOI:10.15774/PPKE.ITK.2018.009

List of Symbols

Physical constants

$\hbar$	reduced Planck constant, $1.054\,571\,596 \times 10^{-34}\,\mathrm{J \cdot s^2}$
e	elementary charge, $1.602\,176\,462 \times 10^{-19}\,\mathrm{C}$
k_B	Boltzmann constant, $1.380\,6503 \times 10^{-23}\,\mathrm{J/K}$
m_{el}	electron rest mass, $9.109\,381\,88 \times 10^{-31}\,\mathrm{kg}$

Quantum mechanical operators and superoperators

$\hat{A}_j$, $\hat{A}_{nm}$	Lindblad operator, describing the system–bath interaction
$\hat{C}_{nm}$	collapse operator, describing the system–bath interaction
$\mathcal{D}(\hat{\rho}_S)$	dissipator of the system with density matrix $\hat{\rho}_S$
$\hat{H}$, $\hat{H}^{(\mathrm{I})}$	Hamiltonian in the Schrödinger and in the interaction picture
$\hat{H}_0$	Hamiltonian of the system and the bath (in the Schrödinger picture) when they do not interact
$\hat{H}_B$	Hamiltonian of the bath (in the Schrödinger picture)
$\hat{H}_S$, $\hat{H}_S^{(\mathrm{I})}$	Hamiltonian of the system in the Schrödinger and in the interaction picture
$\hat{H}_{LS}$, $\hat{H}_{LS}^{(\mathrm{I})}$	Lamb shift Hamiltonian in the Schrödinger and in the interaction picture
$\hat{H}_{SB}$, $\hat{H}_{SB}^{(\mathrm{I})}$	Hamiltonian of the system–bath interaction in the Schrödinger and in the interaction picture
$\hat{I}$	identity operator
$\hat{L}$	quantum mechanical operator (in general)
$\hat{T}$	kinetic energy operator

DOI:10.15774/PPKE.ITK.2018.009

$\hat{U}(t, t_0)$	unitary time-evolution operator
$\hat{V}$	potential energy operator

Further operators and operations

$\hat{A}^\dagger$	conjugate transpose of operator $\hat{A}$
$\langle\psi_a\|\psi_b\rangle$	inner product of wave functions ψ_a and ψ_b
$\left[\hat{A}, \hat{B}\right]$	commutator of operators $\hat{A}$ and $\hat{B}$, defined as $\left[\hat{A}, \hat{B}\right] = \hat{A}\hat{B} - \hat{B}\hat{A}$
$\langle L\rangle$	expectation value of observable L
$\mathcal{O}(f(x))$	denotes a function that is obtained as $f(x)$ multiplied by a positive constant and that provides un upper bound
$\mathrm{tr}\hat{A}$	trace of operator $\hat{A}$
$\mathrm{tr}_B\hat{A}$	partial trace of operator $\hat{A}$ with respect to subsystem B
∇	nabla operator; in Cartesian coordinates, it is equal to $\frac{\partial}{\partial x}\mathbf{i} + \frac{\partial}{\partial y}\mathbf{j} + \frac{\partial}{\partial z}\mathbf{k}$
$\otimes$	tensor product
$\overline{x}$	average value of x
ψ^*	complex conjugate of wave function ψ

Notations of quantum states in general

$\hat{\rho}$	density matrix (density operator)
$\hat{\rho}_S$, $\hat{\rho}_S^{(\mathrm{I})}$	density matrix of the system in the Schrödinger and in the interaction picture
$\hat{\rho}_{B,0}$	density matrix of the bath at $t = 0$
$\langle\psi\|$	bra, representing the complex conjugate of a wave function (in general)
ψ	wave function (in general)
$\|\psi\rangle$	ket, representing a wave function (in general)

Notations of quantum states in the simulation model

$\|\chi_{\varepsilon\nu}^{(i)}\rangle$	ν-th ($\nu = 0, 1, \ldots, V-1$) vibrational basis state of the i-th site, being in the ground ($\varepsilon = g$) or excited ($\varepsilon = e$) electronic state

DOI:10.15774/PPKE.ITK.2018.009

$\lvert\phi_{\varepsilon}^{(i)}\rangle$	ground ($\varepsilon = g$) or excited ($\varepsilon = e$) electronic basis state of the i-th site
$\lvert\Psi\rangle$	arbitrary state of the system
$\lvert\Psi_m\rangle$	m-th basis state of the system
$\lvert\varphi^{(i)}\rangle$	arbitrary state of the i-th site
$\lvert\varphi_{\varepsilon\nu}^{(i)}\rangle$	vibronic basis state of the i-th site, being in electronic state ε and vibrational state ν

Parameters and variables in the simulation model

η	efficiency of the energy transfer
γ	rate constant
$\lambda^{(i)}$	reorganization energy of the i-th site
$\omega_{vib}^{(i)}$	frequency of the vibrational mode of the i-th site
τ_{eg}	time constant of the electronic relaxation
τ_{RC}	time constant of the sink effect of the reaction center
τ_{vib}	time constant of the vibrational relaxation
τ_{pd}	time constant of the pure dephasing
$E_{eg}^{(i)}$	the energy difference between the excited and the ground electronic state of the i-th site
$J^{(ij)}$	coupling between the i-th and j-th sites
N	number of sites in the model system
$S^{(i)}$	Huang–Rhys factor of the i-th site
T	temperature
$V^{(i)}$	number of the considered vibrational levels at the i-th site

Other symbols

$\mathbf{R}$	spatial coordinate vector
$\mathbf{r}$	spatial coordinate vector

DOI:10.15774/PPKE.ITK.2018.009

ξ	dimensionless coordinate
D	dimension of the Hilbert space made up by the possible states of the system
t	time

DOI:10.15774/PPKE.ITK.2018.009

Chapter 1

Introduction

1.1 Context and motivation: quantum biology and the second quantum revolution

In the microscopic world, phenomena that contradict our experience obtained in everyday life are ubiquitous: particles can occur at a place to the reach of which they do not have enough energy classically (this effect is called quantum tunneling), they can be in different states simultaneously (quantum superposition) and can behave as if they were connected—even if they are far away from each other (quantum entanglement). But do these quantum effects also play a role in physiological processes, taking place in the vibrant medium of living matter at high ($\gg 0\,\mathrm{K}$) temperature?

The question is still open [11], albeit it has been examined for a long time within the multidisciplinary field called now quantum biology. Erwin Schrödinger speculated on the quantum mechanical background of the mutation of the genetic code in his famous book *What is life?* as early as 1944 [12], anticipating the description of the structure of deoxyribonucleic acid (DNA) by Watson and Crick [13]. Since then, the occurrence of quantum effects was supposed in several physiological functions [11], [14]–[16]. For instance, it is assumed that proton tunneling plays an important role in the emergence of the mutations of DNA molecules [17], and hydrogen tunneling, in enzyme-catalyzed reactions [18], [19]. It was also suggested that olfactory receptors are activated through electron tunneling that is assisted by odorant molecules with appropriate vibrational properties [20]. Moreover, according to a fashionable model, birds sense the magnetic field of Earth by a molecular compass based on radical pairs [21]–[23], being possibly in an entangled state [24], [25]. Nevertheless, the most intensely studied topic of quantum biology is probably

DOI:10.15774/PPKE.ITK.2018.009

the energy transport taking place during the first stage of photosynthesis, which is also the main subject of this dissertation.

As the above examples demonstrate, quantum biology is a colorful area, which is exciting *per se*. Nevertheless, it is also of great importance from the engineering point of view. During the first quantum revolution, which took place at the beginning of the 20^{th} century, humanity discovered the physical laws of the quantum world. Now, engineers are making efforts to construct machines that exploit quantum coherence and entanglement. The design principles learned from quantum biological systems might provide guidance on this road. If successful, these endeavors can constitute the overture to the second quantum revolution [26], which might bring along quantum computers as well as new types of solar cells and bionic sensors.

1.2 Fundamentals of photosynthetic exciton energy transfer

The energy of living organisms on Earth is predominantly provided by photosynthesis, carried out by plants, algae, and certain types of bacteria [27]. As the first step of the process, a pigment molecule (chromophore) of a light-harvesting complex (also known as an antenna complex) absorbs a photon of sunlight. As a result, the pigment is raised to an excited state—or, in other words, a quasiparticle called Frenkel exciton is created on the pigment. Then, the Coulomb interaction between the pigments moves the exciton from molecule to molecule: while the originally excited molecule returns to the ground state, another molecule is raised to an excited state. The light-harvesting complex behaves, in effect, as a molecular wire, which transfers the energy of the captured sunlight to a pigment–protein complex called a reaction center with a strikingly high efficiency: depending on the type of the antenna complex and on the light conditions, 50–90% of the energy of an absorbed photon is converted into the energy of a pair of separated charges in the reaction center [28].

The energy transfer was explained for long by the Förster theory [29], according to which the exciton hops from pigment to pigment incoherently [30], [31]. The first decade of the present century nevertheless brought surprising findings: quantum states maintaining their coherence for a long time were observed experimentally in photosynthetic systems [32], even at physiological temperature [33], [34]. Shortly thereafter, it was also reported that such states play a part in the energy transfer [35]. The presumed role of quantum coherence is to surmount local energy traps and to promote the trapping of energy at sites connected to the reaction center [36]. The topic is, however, still un-

DOI:10.15774/PPKE.ITK.2018.009

der vigorous debate; some authors dispute even the occurrence of long-lasting quantum coherence in photosynthetic systems [37].

Coherence is a central but nevertheless ambiguous concept. In the present thesis, I shall refer to a state of a quantum system as coherent if it is a linear superposition of two or more basis states.[1] (As it follows from this definition, coherence can be base-dependent.) It is important to add that such a superposition and thus coherence are often related to transitions between the involved basis states, and these transitions frequently lead to oscillatory state dynamics. Nevertheless, the interaction between the pigments and the environment destroys coherence after a while. If, however, (contrary to the assumptions of the Förster theory) coherence lasts long enough, then it can enable the exciton to become delocalized between multiple pigments, resulting in a wavelike energy transfer [31], [32].

The Schrödinger equation provides a general description of the behavior of non-relativistic atomic systems, but its practical applicability is fundamentally limited by two factors: on the one hand, the dimension of the state space (called a Hilbert space) increases exponentially with the number of particles, and on the other hand, the equation is valid only for closed quantum systems, which—contrary to open quantum systems—do not interact with their environment[2], nevertheless, strictly speaking, the only close system is the universe itself. Consequently, *ab initio* modeling of the exciton energy transfer is utterly hopeless. Instead, we have to lean on approximate models, in which the system is restricted to a small number of molecules, characterized by a few states, whereas the rest of the molecules are taken into account as the environment of the system. The main point of this division is that while the state dynamics of the system is treated explicitly, the environment—since we are interested only in the effect it exerts on the system—is modeled in a simplified, averaged manner, for instance, as a heat bath.

1.3 Objectives

In former publications on the photosynthetic exciton energy transfer, pigment molecules were usually modeled as sites with two electronic states, while the molecular vibrations

[1] Note that the off-diagonal elements of the density matrix (see Sec. 2.7.3) are also called coherences, as each of them expresses the superposition of two basis states.

[2] In this dissertation, I distinguish open and closed quantum systems depending on whether they do or do not interact with their environment. Note, however, that some authors call a system closed even if it is exposed to external drives provided that the system dynamics can be described by a time-dependent Hamiltonian, and they use the term isolated for systems governed by a time-independent Hamiltonian [38]. Other authors, in turn, define closedness and openness with the reversibility and irreversibility of the system–environment interaction, respectively, while referring to systems not interacting with the environment at all as isolated [39].

DOI:10.15774/PPKE.ITK.2018.009

were merged into a heat bath. In recent years, however, more and more studies treated some intramolecular modes explicitly as the part of the system. How does the presence of these modes influence the exciton energy transfer? Many papers related intramolecular vibrations to long-lasting coherence [40]–[42] or to enhanced exciton energy transfer [43]–[52], albeit there were also a few reports which inferred that the enhancement is small if the system interacts with its environment [49], [53]. At this point, another question also arises, concerning which I have found only scarce and conflicting statements in the literature [45], [47], [50], [52], [54]: how does the damping of intramolecular vibrations affect the dynamics and the efficiency of the transfer process? Or, putting it another way, can vibrational relaxation induced by the interaction with the environment contribute to the experimentally observed excellent efficiency of the photosynthetic exciton energy transfer?

In this dissertation I examine the above problems. In Chapter 2, I review the theoretical and experimental background of the topic, with special emphasis on the Lindblad master equation. This chapter also serves as a concise summary of the notions occurring in my dissertation, as many of them (*e.g.,* closed and open system, coherence and decoherence) are ambiguously used in the emerging literature of quantum technology. Specialists of the subject can skip these sections (namely, Secs. 2.7, 2.8, and 2.9) and look them up later if they need it during the reading of the subsequent chapters.

In Chapter 3, I present a new general approximate model formulated as a Lindblad-type master equation. Based on this model, I implemented a simulator program, outlined in Chapter 4. By means of the simulator, I investigated dimer and heptamer model arrangements varying several parameters in a systematic manner. I present the results of the simulations in Chapters 5 and 6, respectively. After a short discussion in Chapter 7, I conclude my new scientific results in the form of concise statements in Chapter 8.

Section 2.5, Chapters 3, 5, 6, and 8 as well as the Appendix also form part of a journal article, accepted for publication in *AIP Advances* [1].

DOI:10.15774/PPKE.ITK.2018.009

Chapter 2

Theoretical and Experimental Background

2.1 Photosynthesis in a nutshell

In order to place exciton energy transfer in a broader context, let us review briefly the stages of photosynthesis. Albeit there are significant differences between the phylogenetic groups, the main scheme of photosynthesis is the same in every organism. The process begins with the absorption of sunlight, then the captured energy is transferred to the reaction-center. The arriving energy raises a special pigment of the reaction center to the excited state, as a consequence of which the pigment molecule ejects an electron. The electron then passes through a transfer chain, which—depending on the organism and on the circumstances—leads to the reduction of $NADP^{+}$[1], NAD^{+}[2], or other molecules. At the same time, protons are carried through a membrane, generating a proton gradient, which drives the synthesis of ATP[3] molecules. In the last stage of photosynthesis, carbohydrate molecules of high-energy content are synthesized from CO_2 molecules utilizing the previously produced reductants and ATP molecules [27].

2.2 The light-harvesting apparatus of green sulfur bacteria

Living under extremely low light conditions [27], green sulfur bacteria possess large antenna complexes, called chlorosomes, built up of about 200 000 bacteriocholorophyll (BChl) *c, d,* or *e* pigment molecules. Each chlorosome is linked to a baseplate, which is

[1] nicotinamide adenine dinucleotide phosphate
[2] nicotinamide adenine dinucleotide
[3] adenosine triphosphate

DOI:10.15774/PPKE.ITK.2018.009

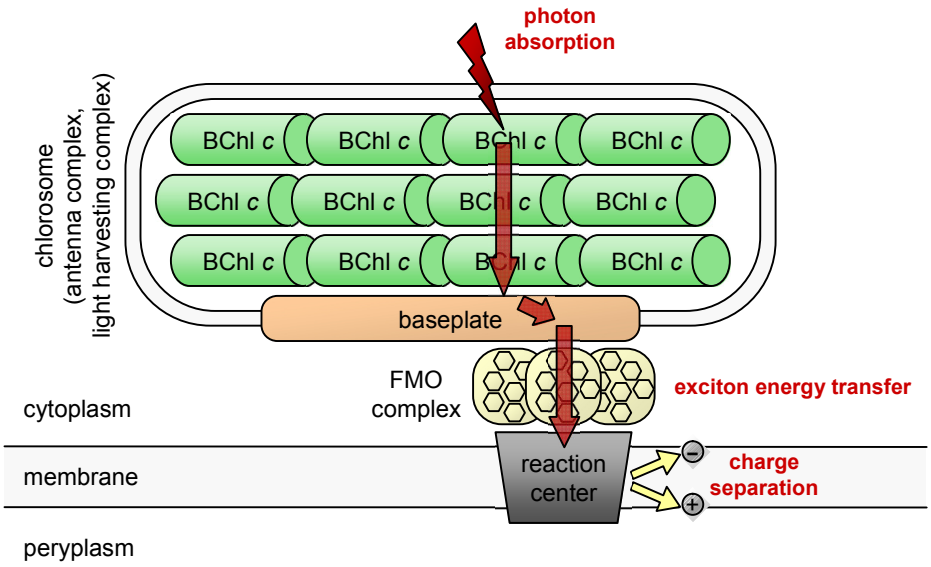

Figure 2.1: The light-harvesting apparatus of green sulfur bacteria. The sunlight is absorbed by the BChl *c* molecules of the chlorosome. Then the captured energy is transferred through the baseplate and the FMO complex to the reaction center, where it provokes a charge separation process. Adapted from Refs. [16] and [55].

in turn connected to about 40 reaction centers by BChl *a*-proteins [55] (Fig. 2.1), also known as Fenna–Matthews–Olson (FMO) protein [56] and as FMO complex. The complex consists of three identical subunits, each of which is composed of a protein chain and seven (according to subsequent results, eight [57]) embedded BChl *a*-molecules [58]. Unlike practically all other chlorophyll-containing components of the light-harvesting systems, the FMO protein is water-soluble, which facilitated its X-ray crystallographic and spectroscopic investigation [59]. Accordingly, this relatively simple complex was the first member of the aforementioned group whose structure was determined [58], and later on, it also became a popular model system of the research of photosynthetic energy transfer. Accordingly, as an example, I also used a heptamer model of the FMO complex in the simulations presented in Chapter 6.

2.3 Two-dimensional electronic spectroscopy

Two-dimensional electronic spectroscopy plays a key role in the research of photosynthetic light-harvesting. During the measurements performed by this technique, the sample is illuminated with three consecutive ultrashort laser pulses. The first pulse gets the molecules into a coherent, oscillating superposition of the ground and an excited state.

DOI:10.15774/PPKE.ITK.2018.009

After a period τ, the second pulse arrives and brings the system to the excited state. Thereafter, the molecules are let to relax over time T. The third pulse then generates a coherent superposition again. Finally, the electric field of the signal emitted by the sample is measured as a function of time t elapsed since the third pulse. Repeating the experiment with different values of τ and performing Fourier transformations with respect to τ and t, one obtains the two-dimensional spectrum [60], [61].

The diagonal peaks of the spectrum correspond to the linear spectrum [60], while the off-diagonal, so called cross peaks indicate electronic couplings between the states [62]. Besides the energy levels and couplings, the two-dimensional spectrum also provides information about excitonic coherence, the spatial properties of excitonic states as well as the transport pathways and the relaxation processes [62]–[64]. As already mentioned in the Introduction, it is this technique that revealed long-lasting coherence in light-harvesting complexes [32]–[35].

2.4 The mechanism of exciton energy transfer—hopping vs. coherent transport

As the pigment molecules participating in the exciton energy transfer interact with their surroundings, it is a standard method to treat them as an open quantum system (Fig. 2.2). Besides the molecules constituting the system of interest, the model of an open quantum system also has to take the environment of the system into account. Since directly one is not interested in its state, only in the effect it has on the system, it is enough to describe the environment in a simplified manner. Accordingly, in this context, the terms system and environment do not necessarily reflect spatial partitioning; they refer, instead, to the conceptual separation of the explicitly and implicitly treated degrees of freedom. For instance, intramolecular vibrational modes can be either the part of the system or that of the environment depending on the model.

When modeling exciton energy transfer, one can distinguish three regimes (Table 2.1). In the first limiting case, where the coupling between the chromophores is much weaker than their coupling to the environment, the inter-chromophore coupling can be treated as a perturbation. In this regime, the interaction with the environment abolishes those states in which the exciton spreads over multiple chromophores. The exciton is thus localized to one pigment, and it hops incoherently from molecule to molecule taking a random walk [31], [65]. This process is described by the Förster theory, which assumes

DOI:10.15774/PPKE.ITK.2018.009

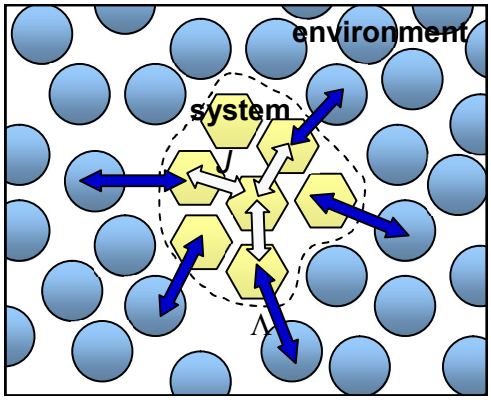

Figure 2.2: Sketch of an open quantum system. The system is composed of the molecules of interest (yellow hexagons), while the surrounding molecules (blue circles) constitute the environment. The blue arrows and J denote the couplings between the molecules of the system, whereas the white arrows and Λ, the system–environment couplings.

Table 2.1: Regimes of the exciton energy transfer with respect to the relation of the coupling strength J between the cromophores (pigment molecules) and the coupling strength Λ between the cromophores and the environment.

Regime	Character of the exciton transfer	Descriptive model
$J \ll \Lambda$	incoherent hopping of localized excitons	Förster theory
$J \sim \Lambda$	partially coherent exciton transfer	more complicated models (*e.g.*, hierarchical equation of motion)
$J \gg \Lambda$	coherent, wavelike motion of delocalized excitons	Schrödinger equation (in theory), Redfield and Lindblad equations (in practice)

that the energy transfer occurs between energetically resonant states, and concludes that the transfer rate of the exciton is proportional to the overlap of the emission spectrum of the donor and the absorption spectrum of the acceptor molecule [29].

In the other limit, where the inter-pigment coupling is much stronger than the coupling to the environment, the exciton becomes delocalized, that is, it can simultaneously be present at multiple chromophores, and it propagates coherently in a wavelike manner following the Schrödinger equation [31], [65]. To comprehend the impact of the interaction with the environment, the equation should also include the representation of the environment—besides, of course, the description of the system composed of the pigments. In practice, it can only be done in some approximative manner. Since in this second limiting case the coupling to the environment is weak, it can be treated in a perturbative manner [31], as it is done in Redfield and Lindblad theories, frequently used to describe photosynthetic exciton energy transfer (see Sec. 2.8).

DOI:10.15774/PPKE.ITK.2018.009

Between the two above limiting cases, one finds the intermediate regime, in which the coupling to the environment is comparable with the couplings between the chromophores, and into which light-harvesting complexes typically fall [31]. In this regime, the exciton transfer is partially coherent [65]. Here, neither type of the couplings can be treated perturbatively. Moreover, the state of the environment can vary considerably while interacting with the system, and its changes might react upon the system [31]. Thus, formally exact results can be obtained in this case only by more complicated methods, such as the hierarchical equation of motion (HEOM) [66] (see Sec. 2.10), whose practical applicability is, however, limited by computational complexity [28].

2.5 Former findings on the role of the environment and intramolecular vibrations in exciton energy transfer

Interestingly, the interaction of the photosynthetic complexes with their environment was demonstrated to support the photosynthetic energy transfer significantly [67]. Nevertheless, the relation between the system–environment interaction, quantum coherence, and the efficiency of exciton energy transfer is intricate. On the one hand, environment-induced correlated fluctuations in the transition energies of the chromophores were reported to protect coherence [68], and appropriately correlated fluctuations in electronic couplings, to enhance quantum coherence and increase the energy transfer rate [69]. On the other hand, it was shown that the dephasing noise of the environment can assist the energy transfer [70] as it suppresses destructive interference and broadens the energy levels of the sites, thus increasing their overlap [71]. Furthermore, numerical investigations revealed that the environment-assisted quantum transport (ENAQT) is robust with respect to many system and environmental parameters [72]. The synthesis of the above statements coincides with the conclusions of [73] and [74]: the optimal energy transport is attained through the interplay of coherent and noisy processes.

Light-harvesting complexes usually behave as energy funnels: they transfer the exciton downhill on an energy landscape sloping to the reaction center [27], [36], [45], [75]. The importance of the energy gradient is pointed out by the finding that the FMO complex, interacting with its environment, reaches higher energy transfer efficiency with its funnel-like (thus off-resonant) site energy arrangement, than it would reach with resonant site energies [76]. The directionality of the exciton transfer on the energy slope is provided by thermal equilibration (heat loss) [27], [45], [75]. Accordingly, temperature consider-

DOI:10.15774/PPKE.ITK.2018.009

ably influences the exciton transfer [36], [51], [53], [74], [76]. The influence prevails in several ways: the raise of the temperature usually speeds up vibrational relaxation [77], [78] and dephasing [74], and it also shifts the thermal equilibrium.

In recent years, vibronic models, which consider the coupling of vibrational and electronic degrees of freedom, proved to be capable of explaining the long-lasting coherence observed by two-dimensional electronic spectroscopy in natural light-harvesting complexes [40], [41] and in an artificial light harvester [42]. It was demonstrated that molecular vibrations—especially those whose frequency is resonant with the energy gap between the electronic states of the sites—can enhance exciton energy transfer [43]–[49], and, moreover, that the nature of these vibrations is non-classical [50]. Some authors explained the improvement of the transfer by the speed up of the "original" pathways [51]; others, by the opening of new coherent transport channels [43], [46], [52]. In addition, the increase of energy transfer was brought into connection with the expansion of the delocalization of the vibronic states [45], [48]. Nonetheless, certain studies—questioning the significance of this design principle—inferred that resonant vibronic states enhance the energy transfer only to a small degree in systems interacting with their environment [49], [53].

Concerning the effect of the damping of intramolecular vibrational modes on the exciton transfer, I have found only few, conflicting statements in the literature. Nalbach *et al.* got enhanced energy transfer when they included an underdamped intramolecular vibrational mode in their model, but they found no enhancement when the mode—treated this time as the part of the spectrum of the environment—was strongly damped [52]. O'Reilly and Olaya-Castro obtained slower transfer for stronger coupling between the prototype dimer and a low-energy thermal bath [50]. (Nevertheless, the presence of the quasi-resonant intramolecular vibrational mode raised the transfer efficiency in this case also.) In contrast, Zhang and Wang showed that increasing the coupling strength between the system and a low-energy thermal bath promotes the energy transfer [47]. Similarly, Liu and Kühn found a moderate acceleration of the exciton transfer in the FMO complex in the case of faster vibrational relaxation [54]. Furthermore, Irish *et al.* pointed out that the damping of a resonant vibrational mode can enhance the energy transfer by generating directionality in the energy flow [45].

DOI:10.15774/PPKE.ITK.2018.009

2.6 The sketch of the road from the Schrödinger equation to the models of the exciton energy transfer

The following sections outline the road from the *ab initio* models to the models of the photosynthetic exciton energy transfer. We will start with the closed quantum systems (Sec. 2.7), which do not interact with their environment. Provided that they are in a pure state, their dynamics can be formulated by the Schrödinger equation. As a next step, the density matrix formalism and the Liouville–von Neumann equation will be introduced, which provide a more general approach inasmuch as they are also able to describe the dynamics of systems being in a mixed state. Finally, taking the interaction with the environment into account, we will arrive at the models of the open quantum systems (Sec. 2.8), among which we will primarily focus on the Lindblad master equation.

2.7 Theoretical description of closed quantum systems

2.7.1 The postulates of quantum mechanics and the Schrödinger equation

Quantum mechanics is built on the following postulates [79]:

1. The state of any quantum system is described by a wave function $\psi\left(q_1, q_2, \ldots, q_f, t\right)$, which maps the generalized coordinates q_i of the system as well as time t to complex numbers.

2. The probability that the system is in the volume element $\mathrm{d}\mathbf{r}$ of the configuration space is given by $\psi^*\psi\mathrm{d}\mathbf{r}$, where the asterisk (*) denotes the complex conjugate of the wave function.

3. There is a linear operator $\hat{L}$ for each observable L. The results of the measurements of a physical quantity can only be the eigenvalues λ of the corresponding operator:

$$\hat{L}\psi = \lambda\psi. \tag{2.1}$$

4. The expectation value of an observable L is

$$\langle L \rangle = \int \psi^* \hat{L} \psi \mathrm{d}\mathbf{r}. \tag{2.2}$$

DOI:10.15774/PPKE.ITK.2018.009

5. The time-evolution of the state of a closed quantum system is given by the time-dependent Schrödinger equation

$$\mathrm{i}\hbar\frac{\partial\psi\left(\mathbf{r},t\right)}{\partial t}=\hat{H}\psi\left(\mathbf{r},t\right), \tag{2.3}$$

where $\hbar$ denotes the reduced Planck constant, and $\hat{H}$ is the Hamiltonian, *i.e.,* the operator of the total energy of the system. For one particle, the Hamiltonian can be formulated as

$$\hat{H}=-\frac{\hbar^2}{2m}\nabla^2+V\left(\mathbf{r}\right), \tag{2.4}$$

where the first term expresses the kinetic energy, and the second term is the potential energy as a function of the spatial coordinates; m denotes the mass of the particle, and ∇ is the nabla operator, which, in Cartesian coordinates, is equal to $\frac{\partial}{\partial x}\mathbf{i}+\frac{\partial}{\partial y}\mathbf{j}+\frac{\partial}{\partial z}\mathbf{k}$.[4]

From the mathematical point of view, the wave functions ψ describing the possible states of a quantum system form a Hilbert space. To represent the wave-functions ψ and their complex conjugates ψ^*, Dirac introduced $|\psi\rangle$ and $\langle\psi|$, called ket and bra, respectively. Dirac derived these terms splitting the word "bra-ket", referring to the bracket that he used to denote the inner product

$$\langle\psi|\psi\rangle=\int\psi^*\psi\mathrm{d}\mathbf{r}. \tag{2.5}$$

The mathematical description of the elements of a Hilbert space requires a basis. A commonly used one is the energy basis. It is formed by the eigenvectors of the Hamiltonian, which can be obtained by solving the time-independent Schrödinger equation

$$\hat{H}\psi=E\psi. \tag{2.6}$$

In any basis, we can express any element ψ of the Hilbert space as the linear combination of the basis functions ϕ_i; that is, in the form

$$\psi=\sum_{i=1}^{n}c_i\phi_i, \tag{2.7}$$

[4] In general, the Hamiltonian itself can also be time-dependent. See also footnote 2 on page 18.

DOI:10.15774/PPKE.ITK.2018.009

where the coefficients c_i are the complex amplitudes, for which $\sum_{i=1}^{n} = |c_i|^2$. Then, the ket representing the state can be expressed as a column vector

$$|\psi\rangle = \begin{bmatrix} c_1 \\ c_2 \\ \vdots \\ c_n \end{bmatrix}, \tag{2.8}$$

and the corresponding bra, as a row vector

$$\langle\psi| = \begin{bmatrix} c_1^* & c_2^* & \dots & c_n^* \end{bmatrix}. \tag{2.9}$$

In this approach, an operator $\hat{A}$ can be represented by a matrix A with complex elements [80]

$$A_{ij} = \langle\psi_i| \hat{A} |\psi_j\rangle. \tag{2.10}$$

An important example of the operators is the unitary time-evolution operator $\hat{U}(t, t_0)$, which maps the initial state $|\psi(t_0)\rangle$ to state $|\psi(t)\rangle$ at time t according to the equation

$$|\psi(t)\rangle = \hat{U}(t, t_0) |\psi(t_0)\rangle, \tag{2.11}$$

expressing the formal solution of the Schrödinger equation (2.3) [38].

2.7.2 The Hamilton operator of a molecular system

For a molecular system composed of pointlike nuclei and electrons, the Hamilton operator in general takes the form

$$\hat{H}_{mol} = \hat{T}_{el} + \hat{T}_{nucl} + \hat{V}_{el-el} + \hat{V}_{el-nucl} + \hat{V}_{nucl-nucl}, \tag{2.12}$$

where

$$\hat{T}_{el} = \sum_{j=1}^{N_{el}} -\frac{\hbar^2}{2m_{el}} \nabla_j^2, \tag{2.13}$$

$$\hat{T}_{nucl} = \sum_{n=1}^{N_{nucl}} -\frac{\hbar^2}{2M_n} \nabla_n^2 \tag{2.14}$$

are the kinetic energy operators of the electrons of mass m_{el} and nuclei of mass M_n;

DOI:10.15774/PPKE.ITK.2018.009

$$\hat{V}_{el-el} = \frac{1}{2}\sum_{i\neq j}\frac{e^2}{|\mathbf{r}_i - \mathbf{r}_j|}, \tag{2.15}$$

$$\hat{V}_{el-nucl} = -\frac{1}{2}\sum_{i,n}\frac{Z_n e^2}{|\mathbf{r}_i - \mathbf{R}_n|}, \tag{2.16}$$

$$\hat{V}_{nucl-nucl} = \frac{1}{2}\sum_{m\neq n}\frac{Z_m Z_n e^2}{|\mathbf{R}_m - \mathbf{R}_n|} \tag{2.17}$$

are the potential energy operators derived from the Coulomb forces acting between two electrons, between an electron and a nucleus, and between two nuclei; $\mathbf{r}_j$ and $\mathbf{R}_j$ denote the spatial coordinates of the j-th electron and n-th nucleus, respectively, while e is the elementary charge and Z_n is the atomic number of the n-th nucleus [65].

2.7.3 The density matrix and the Liouville–von Neumann equation

The systems discussed so far were in a so called pure state, meaning that they could be described by a single wave function ψ (or correspondingly, a ket $|\psi\rangle$). If, however, our knowledge about the state of a system is incomplete, for instance, because we do not know how certain factors have influenced the system, or we have an inhomogeneous ensemble, then we say that the system is in a mixed state. Let as assume that all we know about the system is that it is in state $|\psi_1\rangle$ with classical probability p_1, in $|\psi_2\rangle$ with classical probability p_2 and so on. To formulate the state of the system in a concise manner, we can use the density matrix (or density operator), defined as [80]

$$\hat{\rho} = \sum_i p_i \left|\psi_i\right\rangle \left\langle\psi_i\right|. \tag{2.18}$$

The diagonal elements of the density matrix are called populations; the element ρ_{jj} gives the probability that the system is in basis state ϕ_j, introduced above. The off-diagonal elements are called coherences; ρ_{kl} expresses a kind of a coexistence of basis states ϕ_k and ϕ_l.

By means of the corresponding operators, we can extract the ensemble average of the expectation value of any observable quantity A according to

$$\overline{\langle L\rangle} = \mathrm{tr}\left(\hat{\rho}\hat{L}\right), \tag{2.19}$$

where

DOI:10.15774/PPKE.ITK.2018.009

$$\mathrm{tr}\hat{A} = \sum_i \langle \phi_i | \hat{A} | \phi_i \rangle = \sum_i A_{ii} \tag{2.20}$$

denotes the trace of operator $\hat{A}$, being equal to the sum of the diagonal elements of the representing matrix. For the density matrix, as it follows from its definition (Eq. (2.18)), it holds that

$$\mathrm{Tr}\hat{\rho} = 1. \tag{2.21}$$

To determine the time-evolution of a system being in a mixed state, we can of course use the Schrödinger equation (2.3) for each state $|\psi_i\rangle$, and then average the outcomes using the weight factors p_i. This is what the Liouville–von Neumann or simply von Neumann equation

$$\frac{\mathrm{d}\hat{\rho}(t)}{\mathrm{d}t} = -\frac{\mathrm{i}}{\hbar}\left[\hat{H}(t), \hat{\rho}(t)\right], \tag{2.22}$$

expresses in a compact form, when it describes the time-evolution of the density matrix [38], [80]. The bracket in the equation denotes the commutator of the two operators, which is defined as $\left[\hat{A}, \hat{B}\right] = \hat{A}\hat{B} - \hat{B}\hat{A}$. Since the effect of the environment on a quantum system is usually known only in an averaged manner, this formalism is especially useful to describe the behavior of open quantum systems, as we will see it in the following sections.

2.8 Derivation of the Lindblad master equation, a widely used model of open quantum systems

Based on Refs. [38] and [81], this section summarizes the derivation of two quantum master equations that are widely used to describe the dynamics of open quantum systems. We will depart from the Liouville–von Neumann equation. Then, making the Born and Markov approximations, we will reach the Redfield equation. From this, we will get through the rotating wave approximation to the Lindblad master equation.

2.8.1 The Liouville–von Neumann equation in the interaction picture

Up to this point, we used the so called Schrödinger picture, which describes the time-evolution of a quantum system through a time-varying state vector $|\psi(t)\rangle$ or density matrix $\hat{\rho}(t)$, represented in a fixed basis [79] (see Eqs. (2.3) and (2.22)). On the other hand, in the Heisenberg picture, the state vector $\left|\psi^{(\mathrm{H})}(t_0)\right\rangle$ (or density matrix $\hat{\rho}^{(\mathrm{H})}(t_0)$)

DOI:10.15774/PPKE.ITK.2018.009

is fixed, while the operators $\hat{A}^{(\mathrm{H})}(t)$ are time-dependent. The third, intermediate representation is the so called interaction picture (or Dirac picture [79]). In this approach, the part that describes the interaction between the subsystems is separated within the Hamiltonian: the interaction term governs the time-evolution of the state vector, while the "rest" determines the time-evolution of the operators [82]. The three pictures are equivalent, and it depends on the problem which of them is the most convenient. Note that (H) or (I) in superscript in the notation of the state vectors and operators refer to the Heisenberg and interaction pictures, respectively, while the lack of these symbols indicates the Schrödinger picture.

Following [38] and [81], let us consider an open quantum system S coupled to its environment, modeled as a heat bath B. The Hamiltonian of the total arrangement is given in the Schrödinger picture as

$$\hat{H}_{tot}(t) = \underbrace{\hat{H}_S \otimes \hat{I}_B + \hat{I}_S \otimes \hat{H}_B}_{\hat{H}_0} + \hat{H}_{SB}(t), \tag{2.23}$$

where $\hat{H}_S$ and $\hat{H}_B$ are the Hamiltonians of the system and the bath, respectively, which together form the free system Hamiltonian $\hat{H}_0$, $\hat{H}_{SB}$ is the Hamiltonian of the interaction between the system and the bath, $\hat{I}_S$ and $\hat{I}_B$ stand for the identity operators of the two subsystems, while $\otimes$ denotes tensor product. For the composite system, the Schrödinger picture Liouville–von Neumann equation (2.22) takes the form

$$\frac{\mathrm{d}\hat{\rho}_{tot}(t)}{\mathrm{d}t} = -\frac{\mathrm{i}}{\hbar}\left[\hat{H}_0 + \hat{H}_{SB}(t), \hat{\rho}_{tot}(t)\right], \tag{2.24}$$

where $\hat{\rho}_{tot}$ denotes the density matrix of the total system. In the following, this equation will be transformed to its interaction picture equivalent, in which the time-evolution of the density operator is governed by the interaction Hamiltonian $\hat{H}_{SB}^{(\mathrm{I})}(t)$.

Expanding the commutator, as well as left and right multiplying the equation by the unitary time-evolution operators $\hat{U}_0(t,0) = e^{-\mathrm{i}\hat{H}_0 t/\hbar}$ and $\hat{U}_0^{\dagger}(t,0) = e^{\mathrm{i}\hat{H}_0 t/\hbar}$, respectively, we get

$$\begin{aligned} &e^{\mathrm{i}\hat{H}_0 t/\hbar}\frac{\mathrm{d}\hat{\rho}_{tot}(t)}{\mathrm{d}t}e^{-\mathrm{i}\hat{H}_0 t/\hbar} = \\ &\quad -\frac{\mathrm{i}}{\hbar}\left(e^{\mathrm{i}\hat{H}_0 t/\hbar}\hat{H}_0 \underset{\uparrow}{}\hat{\rho}_{tot}(t)\, e^{-\mathrm{i}\hat{H}_0 t/\hbar} - e^{\mathrm{i}\hat{H}_0 t/\hbar}\hat{\rho}_{tot}(t) \underset{\uparrow}{}\hat{H}_0 e^{-\mathrm{i}\hat{H}_0 t/\hbar}\right) \\ &\quad -\frac{\mathrm{i}}{\hbar}\left(e^{\mathrm{i}\hat{H}_0 t/\hbar}\hat{H}_{SB}(t) \underset{\uparrow}{}\hat{\rho}_{tot}(t)\, e^{-\mathrm{i}\hat{H}_0 t/\hbar} - e^{\mathrm{i}\hat{H}_0 t/\hbar}\hat{\rho}_{tot}(t) \underset{\uparrow}{}\hat{H}_{SB}(t)\, e^{-\mathrm{i}\hat{H}_0 t/\hbar}\right). \end{aligned} \tag{2.25}$$

DOI:10.15774/PPKE.ITK.2018.009

Let us insert $e^{-\mathrm{i}\hat{H}_0 t/\hbar}e^{\hat{H}_0 t/\hbar} = \hat{I}$ as a multiplying factor at the positions marked with the arrows, between the Hamiltonians and the density operators. Then we obtain

$$\begin{aligned} e^{\mathrm{i}\hat{H}_0 t/\hbar}\frac{\mathrm{d}\hat{\rho}_{tot}(t)}{\mathrm{d}t}e^{-\mathrm{i}\hat{H}_0 t/\hbar} = \\ -\frac{\mathrm{i}}{\hbar}\Big(e^{\mathrm{i}\hat{H}_0 t/\hbar}\hat{H}_0 e^{-\mathrm{i}\hat{H}_0 t/\hbar}e^{\hat{H}_0 t/\hbar}\hat{\rho}_{tot}(t)\,e^{-\mathrm{i}\hat{H}_0 t/\hbar} \\ -e^{\mathrm{i}\hat{H}_0 t/\hbar}\hat{\rho}_{tot}(t)\,e^{-\mathrm{i}\hat{H}_0 t/\hbar}e^{\hat{H}_0 t/\hbar}\hat{H}_0 e^{-\mathrm{i}\hat{H}_0 t/\hbar}\Big) \\ -\frac{\mathrm{i}}{\hbar}\Big(e^{\mathrm{i}\hat{H}_0 t/\hbar}\hat{H}_{SB}(t)\,e^{-\mathrm{i}\hat{H}_0 t/\hbar}e^{\hat{H}_0 t/\hbar}\hat{\rho}_{tot}(t)\,e^{-\mathrm{i}\hat{H}_0 t/\hbar} \\ -e^{\mathrm{i}\hat{H}_0 t/\hbar}\hat{\rho}_{tot}(t)\,e^{-\mathrm{i}\hat{H}_0 t/\hbar}e^{\hat{H}_0 t/\hbar}\hat{H}_{SB}(t)\,e^{-\mathrm{i}\hat{H}_0 t/\hbar}\Big). \end{aligned} \tag{2.26}$$

This equation can be recast as

$$\begin{aligned} \frac{\mathrm{d}}{\mathrm{d}t}\Big(e^{\mathrm{i}\hat{H}_0 t/\hbar}\hat{\rho}_{tot}(t)\,e^{-\mathrm{i}\hat{H}_0 t/\hbar}\Big) = \\ -\frac{\mathrm{i}}{\hbar}\left[e^{\mathrm{i}\hat{H}_0 t/\hbar}\hat{H}_0 e^{-\mathrm{i}\hat{H}_0 t/\hbar}, e^{\mathrm{i}\hat{H}_0 t/\hbar}\hat{\rho}_{tot}(t)\,e^{-\mathrm{i}\hat{H}_0 t\hbar}\right] \\ -\frac{\mathrm{i}}{\hbar}\left[e^{\mathrm{i}\hat{H}_0 t/\hbar}\hat{H}_{SB}(t)\,e^{-\mathrm{i}\hat{H}_0 t/\hbar}, e^{\mathrm{i}\hat{H}_0 t/\hbar}\hat{\rho}_{tot}(t)\,e^{-\mathrm{i}\hat{H}_0 t\hbar}\right], \end{aligned} \tag{2.27}$$

where it has been considered that

$$e^{\mathrm{i}\hat{H}_0 t/\hbar}\frac{\mathrm{d}\hat{\rho}_{tot}(t)}{\mathrm{d}t}e^{-\mathrm{i}\hat{H}_0 t/\hbar} = \frac{\mathrm{d}}{\mathrm{d}t}\Big(e^{\mathrm{i}\hat{H}_0 t/\hbar}\hat{\rho}_{tot}(t)\,e^{-\mathrm{i}\hat{H}_0 t/\hbar}\Big). \tag{2.28}$$

In Eq. (2.27), the first commutator on the right hand side diminishes, as $e^{\pm\mathrm{i}\hat{H}_0 t}$ commutes with $\hat{H}_0$, and thus $e^{\mathrm{i}\hat{H}_0 t/\hbar}\hat{H}_0 e^{-\mathrm{i}\hat{H}_0 t/\hbar} = \hat{I}$. Introducing the notations

$$\hat{H}_{SB}^{(\mathrm{I})}(t) = e^{\mathrm{i}\hat{H}_0 t/\hbar}(t)\,\hat{H}_{SB}(t)\,e^{-\mathrm{i}\hat{H}_0 t/\hbar}, \tag{2.29}$$

$$\hat{\rho}_{tot}^{(\mathrm{I})}(t) = e^{\mathrm{i}\hat{H}_0 t/\hbar}\hat{\rho}_{tot}(t)\,e^{-\mathrm{i}\hat{H}_0 t/\hbar} \tag{2.30}$$

and substituting them to the remaining terms of Eq. (2.27), we arrive at the interaction picture Liouville–von Neumann equation

$$\frac{\mathrm{d}}{\mathrm{d}t}\hat{\rho}_{tot}^{(\mathrm{I})}(t) = -\frac{\mathrm{i}}{\hbar}\left[\hat{H}_{SB}^{(\mathrm{I})}(t), \hat{\rho}_{tot}^{(\mathrm{I})}(t)\right], \tag{2.31}$$

which thus contains explicitly only the interaction Hamiltonian.

Let us put Eq. (2.31) in the integral form

DOI:10.15774/PPKE.ITK.2018.009

$$\hat{\rho}_{tot}^{(\mathrm{I})}(t) = \hat{\rho}_{tot}^{(\mathrm{I})}(0) - \frac{\mathrm{i}}{\hbar}\int_0^t \left[\hat{H}_{SB}^{(\mathrm{I})}(\tau), \hat{\rho}_{tot}^{(\mathrm{I})}(\tau)\right] d\tau. \tag{2.32}$$

Inserting this formula back into the right hand side of Eq. (2.31), we obtain

$$\frac{\mathrm{d}}{\mathrm{d}t}\hat{\rho}_{tot}^{(\mathrm{I})}(t) = -\frac{1}{\hbar}\left[\hat{H}_{SB}^{(\mathrm{I})}, \hat{\rho}_{tot}^{(\mathrm{I})}(0)\right] - \frac{1}{\hbar^2}\int_0^t \left[\hat{H}_{SB}^{(\mathrm{I})}(t), \left[\hat{H}_{SB}^{(\mathrm{I})}(\tau), \hat{\rho}_{tot}^{(\mathrm{I})}(\tau)\right]\right] d\tau. \tag{2.33}$$

The density matrix $\hat{\rho}_{tot}^{(\mathrm{I})}$, occurring in the above equations, represents the state of the total system–bath composite. From this, the so called reduced density matrix $\hat{\rho}_S^{(I)}$ of the system can be extracted by taking the partial trace of $\hat{\rho}_{tot}^{(\mathrm{I})}$ over the degrees of freedom of the bath, that is,

$$\hat{\rho}_S^{(I)}(t) = \mathrm{tr}_B \hat{\rho}_{tot}^{(I)}(t). \tag{2.34}$$

Accordingly, if we take the partial trace of Eq. (2.33) with respect to the bath, then, assuming that[5]

$$\mathrm{tr}_B\left[\hat{H}_{SB}^{(\mathrm{I})}(t), \hat{\rho}_{tot}^{(\mathrm{I})}(0)\right] = 0, \tag{2.35}$$

we obtain

$$\frac{\mathrm{d}}{\mathrm{d}t}\hat{\rho}_S^{(\mathrm{I})}(t) = -\frac{1}{\hbar^2}\int_0^t \mathrm{tr}_B\left[\hat{H}_{SB}^{(\mathrm{I})}(t), \left[\hat{H}_{SB}^{(\mathrm{I})}(\tau), \hat{\rho}_{tot}^{(\mathrm{I})}(\tau)\right]\right] d\tau. \tag{2.36}$$

2.8.2 Born approximation

Let $\hat{\rho}_{B,0}$ denote the initial density matrix of the bath. Then, we may express the state of the system–bath composite at time t as

$$\hat{\rho}_{tot}^{(\mathrm{I})}(t) = \hat{\rho}_S^{(\mathrm{I})}(t) \otimes \hat{\rho}_{B,0} + \mathcal{O}\left(\hat{H}_{SB}\right), \tag{2.37}$$

where the last term represents the correction that is required because the interaction causes changes in the state of the bath as time goes on. If the system–bath coupling

[5] As $\hat{H}_{SB}^{(\mathrm{I})}$ is determined by $\hat{H}_{SB}$ (see Eq. (2.29)), which in turn depends on the operators $\hat{B}_\alpha(t)$ of the bath (see Eq. (2.44)), the condition stated in Eq. (2.35) can be traced back to the properties of the bath. If $\left\langle \hat{B}_\alpha \right\rangle = \mathrm{tr}_B\left\{\hat{B}_\alpha(t)\hat{\rho}_{B,0}\right\} = 0$, then Eq. (2.35) holds [38], [83].

DOI:10.15774/PPKE.ITK.2018.009

is weak, then these changes are negligible. Accordingly, in the Born approximation, we omit the correction term $\mathcal{O}\left(\hat{H}_{SB}\right)$. Then, the substitution of the approximate formula

$$\hat{\rho}_{tot}^{(\mathrm{I})}(t) \approx \hat{\rho}_{S}^{(\mathrm{I})}(t) \otimes \hat{\rho}_{B,0} \tag{2.38}$$

into Eq. (2.36) gives

$$\frac{\mathrm{d}}{\mathrm{d}t}\hat{\rho}_{S}^{(\mathrm{I})}(t) = -\frac{1}{\hbar^2}\int_0^t \mathrm{tr}_B\left[\hat{H}_{SB}^{(\mathrm{I})}(t), \left[\hat{H}_{SB}^{(\mathrm{I})}(\tau), \hat{\rho}_{S}^{(\mathrm{I})}(\tau) \otimes \hat{\rho}_{B,0}\right]\right] d\tau, \tag{2.39}$$

which is the second order approximation of the equation of motion.

2.8.3 Markov approximation—Redfield equation

The next, so called Markov approximation also assumes that the bath undergoes only small changes during the interaction with the system, or, to be more precise, that the changes of the bath (as it is large and it is in thermal equilibrium) decay over a time scale much shorter than the time scale of the dynamics of the system. In other words, we consider the bath memoryless. Under such circumstances, the evolution of the system does not depend on the past of the system, but solely on its present state. Therefore, we can replace $\hat{\rho}_{S}^{(\mathrm{I})}(\tau)$ with $\hat{\rho}_{S}^{(\mathrm{I})}(t)$ in Eq. (2.39), which yields the Redfield equation

$$\frac{\mathrm{d}}{\mathrm{d}t}\hat{\rho}_{S}^{(\mathrm{I})}(t) = -\frac{1}{\hbar^2}\int_0^t \mathrm{tr}_B\left[\hat{H}_{SB}^{(\mathrm{I})}(t), \left[\hat{H}_{SB}^{(\mathrm{I})}(\tau), \hat{\rho}_{S}^{(\mathrm{I})}(t) \otimes \hat{\rho}_{B,0}\right]\right] d\tau. \tag{2.40}$$

2.8.4 Secular or rotating wave approximation—Lindblad equation

To eliminate the dependence of the evolution on the selection of the initial time, let us replace τ by $t-\tau$ in the integrand and t by ∞ in the upper limit of the integral assuming. The latter step means that we consider $\hat{H}_{SB}^{(\mathrm{I})}$ on the interval $[-\infty, t]$. This can be done because we assumed that the bath correlation functions decay fast compared to the time scale of the system dynamics. So, we obtain

$$\frac{\mathrm{d}}{\mathrm{d}t}\hat{\rho}_{S}^{(\mathrm{I})}(t) = -\frac{1}{\hbar^2}\int_0^\infty \mathrm{tr}_B\left[\hat{H}_{SB}^{(\mathrm{I})}(t), \left[\hat{H}_{SB}^{(\mathrm{I})}(t-\tau), \hat{\rho}_{S}^{(\mathrm{I})}(t) \otimes \hat{\rho}_{B,0}\right]\right] d\tau. \tag{2.41}$$

Let us express the Schrödinger picture interaction Hamiltonian as

DOI:10.15774/PPKE.ITK.2018.009

$$\hat{H}_{SB} = \sum_{\alpha} \hat{A}_{\alpha} \otimes \hat{B}_{\alpha}, \tag{2.42}$$

where the Hermitian operators $\hat{A}_{\alpha}$ and $\hat{B}_{\alpha}$ reflect which states the system–bath interaction α couples within the system and within the bath. As a next step, we decompose the operators $\hat{A}_{\alpha}$ to the eigenoperators $\hat{A}_{\alpha}(\omega)$ of the Schrödinger picture system Hamiltonian $\hat{H}_S$ in the form

$$\hat{A}_{\alpha} = \sum_{\alpha,\omega} \hat{A}_{\alpha}(\omega), \tag{2.43}$$

according to the energy difference ω between the coupled eigenstates. These operators enable us to rewrite the interaction picture interaction Hamiltonian as

$$\hat{H}_{SB}^{(\mathrm{I})}(t) = \sum_{\alpha,\omega} e^{-\mathrm{i}\omega t} \hat{A}_{\alpha}(\omega) \otimes \hat{B}_{\alpha}(t), \tag{2.44}$$

where

$$\hat{B}_{\alpha}(t) = e^{\mathrm{i}\hat{H}_B t} \hat{B}_{\alpha} e^{-\mathrm{i}\hat{H}_B t}. \tag{2.45}$$

Substituting the formula given in Eq. (2.44) into Eq. (2.41) yields

$$\begin{aligned} \frac{\mathrm{d}}{\mathrm{d}t}\hat{\rho}_S^{(\mathrm{I})}(t) = \sum_{\omega,\omega'}\sum_{\alpha,\beta} e^{\mathrm{i}(\omega'-\omega)t} \hat{\Gamma}_{\alpha\beta}(\omega) \Big(& \hat{A}_{\beta}(\omega) \hat{\rho}_S^{(\mathrm{I})}(t) \hat{A}_{\alpha}^{\dagger}(\omega') \\ & - \hat{A}_{\alpha}^{\dagger}(\omega) \hat{A}_{\beta}(\omega) \hat{\rho}_S^{(\mathrm{I})}(t) \Big) + \mathrm{h.c.} \end{aligned} \tag{2.46}$$

In the equation, h.c. stands for the Hermitian conjugate of the preceding expression, and

$$\hat{\Gamma}_{\alpha\beta}(\omega) = \int_0^{\infty} e^{\mathrm{i}\omega s} \left\langle \hat{B}_{\alpha}^{\dagger}(t) \hat{B}_{\beta}(t-s) \right\rangle ds \tag{2.47}$$

is the one-sided Fourier transform of the bath correlation functions

$$\left\langle \hat{B}_{\alpha}^{\dagger}(t) \hat{B}_{\beta}(t-s) \right\rangle = \mathrm{tr}_B \left\{ \hat{B}_{\alpha}^{\dagger}(t) \hat{B}_{\beta}(t-s) \hat{\rho}_{B,0} \right\}. \tag{2.48}$$

.

In Eq. (2.46), those terms in which $\omega \neq \omega'$ exhibit fast oscillation. Provided that the time scale of these oscillations is short compared to the time scale of the system

DOI:10.15774/PPKE.ITK.2018.009

dynamics, these terms can be omitted. Making this so called secular or rotating wave approximation, we obtain the interaction picture Lindblad equation

$$\frac{\mathrm{d}}{\mathrm{d}t}\hat{\rho}_S^{(\mathrm{I})}(t) = -\frac{\mathrm{i}}{\hbar}\left[\hat{H}_{LS}^{(\mathrm{I})}, \hat{\rho}_S^{(\mathrm{I})}(t)\right] + \mathcal{D}\left(\hat{\rho}_S^{(\mathrm{I})}(t)\right). \tag{2.49}$$

Here,

$$\hat{H}_{LS}^{(\mathrm{I})} = \sum_{\omega}\sum_{\alpha,\beta}\frac{1}{2\mathrm{i}}\left(\hat{\Gamma}_{\alpha\beta}(\omega) - \hat{\Gamma}_{\beta\alpha}^{\dagger}(\omega)\right) \tag{2.50}$$

is the Lamb shift Hamiltonian, reflecting the alteration of the energy levels of the system and the bath due to their coupling. The superoperator

$$\mathcal{D}\left(\rho_S^{(\mathrm{I})}(t)\right) = \sum_{\omega}\sum_{\alpha,\beta}\hat{\gamma}_{\alpha\beta}\left(\hat{A}_{\beta}(\omega)\,\hat{\rho}_S^{(\mathrm{I})}(t)\,\hat{A}_{\alpha}^{\dagger}(\omega')\right.$$
$$\left. -\frac{1}{2}\hat{A}_{\alpha}^{\dagger}(\omega)\,\hat{A}_{\beta}(\omega)\,\hat{\rho}_S^{(\mathrm{I})}(t) - \frac{1}{2}\hat{\rho}_S^{(\mathrm{I})}(t)\,\hat{A}_{\alpha}^{\dagger}(\omega)\,\hat{A}_{\beta}(\omega)\right), \tag{2.51}$$

called the dissipator, represents the non-unitary processes in the system, induced by the interaction with the environment, where

$$\hat{\gamma}_{\alpha\beta} = \hat{\Gamma}_{\alpha\beta}(\omega) + \hat{\Gamma}_{\beta\alpha}^{\dagger}(\omega). \tag{2.52}$$

Finally, converting Eq. (2.49) to the Schrödinger picture, we obtain

$$\frac{\mathrm{d}}{\mathrm{d}t}\hat{\rho}_S(t) = -\frac{\mathrm{i}}{\hbar}\left[\hat{H}_{LS} + \hat{H}_S, \hat{\rho}_S(t)\right] + \mathcal{D}\left(\hat{\rho}_S(t)\right), \tag{2.53}$$

which can be simplified to the form

$$\frac{\mathrm{d}}{\mathrm{d}t}\hat{\rho}_S(t) = -\frac{\mathrm{i}}{\hbar}\left[\hat{H}_{LS} + \hat{H}_S, \hat{\rho}_S(t)\right] \tag{2.54}$$
$$+\sum_j \gamma_j\left(\hat{A}_j\hat{\rho}_S(t)\,\hat{A}_j^{\dagger} - \frac{1}{2}\hat{A}_j^{\dagger}\hat{A}_j\hat{\rho}_S(t) - \frac{1}{2}\hat{\rho}_S(t)\,\hat{A}_j^{\dagger}\hat{A}_j\right), \tag{2.55}$$

where the rate constants γ_j are non-negative numbers, and $\hat{A}_j$ denote the Lindblad operators, representing the system–bath coupling.

DOI:10.15774/PPKE.ITK.2018.009

2.9 Effect of the environment

Excited molecules relax after a while passing their excess energy in a radiative or non-radiative way to their surroundings. This phenomenon is called T_1 (longitudinal) damping, and it leads to the exponential decay of the population of the excited state. In this thesis, I will refer to this process as relaxation. On the other hand, we talk about T_2 (transverse) damping when the elastic collision of the atoms and the interaction with molecular vibrations disturb only the phase of the wave functions of the molecules causing only decoherence without the occurrence of population transfer [84]. For the latter process, I will use the term pure dephasing.

2.10 Comparison of Redfield equation, Lindblad equation, and hierarchical equation of motion

As it was presented in Sec. 2.8, both the Redfield and the Lindblad equation treat the system–environment interaction in a second-order approximation. The main advantage of the Lindblad equation is that it guarantees the physical meaningfulness of the density matrix keeping its diagonal elements positive and its trace 1. On the other hand, the Redfield equation is more general in the sense that it does not require the secular approximation, but in this case one has to describe the system–bath interaction with special care so that the physicality of the model will be preserved [85].

Although the aforementioned two methods are widely used for the modeling of photosynthetic exciton energy transfer, it must be kept in mind that they fail as they overestimate the transfer rate when the system–environment coupling is strong and thus the error of the Markov approximation is increased [86]. To handle this shortcoming, *Ishizaki* and *Fleming* [66] adapted a model published by *Tanimura* [87]. This approach is known today as the hierarchical equation of motion (HEOM). Using auxiliary operators, the model describes the dynamics of the system interacting with the coupled bath in a formally exact manner. In practice, however, the number of the auxiliary operators taken into consideration has to be limited. Moreover, due to the large computational complexity of the method, its applicability is restricted to smaller systems [28].

DOI:10.15774/PPKE.ITK.2018.009

Chapter 3

Simulation Model

3.1 Outline of the model

In this Chapter, I present the general model that I constructed to study how intramolecular vibrational modes influence the dynamics of photosynthetic exciton energy transfer, focusing particularly on the impact of vibrational relaxation on the efficiency of the process.

I approached the problem using the Lindblad formalism, presented in Sec. 2.8, which enabled me to construct a simple, clear-cut model to explore the characteristics of the energy transfer. The framework of my model is the following (see also Fig. 3.1):

1. The prototype systems are built up of N pigment molecules (sites). Each site has two electronic states, coupled with an explicit intramolecular vibrational mode (which is thus incorporated into the system, not into the bath). The vibronic state of each site is given as the product of its electronic and vibrational states. The state of the system is in turn formulated as the product of the states of the sites.

2. The dipole–dipole interaction between two sites is formulated as the coupling between the corresponding vibronic states of the system, considering the Franck–Condon principle.

3. I assume a memoryless environment[1], whose effect on the system is described phenomenologically as incoherent relaxation and—if the temperature is higher than zero—excitation.

[1] This assumption is required for the Born and Markov approximations, presented in Secs. 2.8.2 and 2.8.3.

DOI:10.15774/PPKE.ITK.2018.009

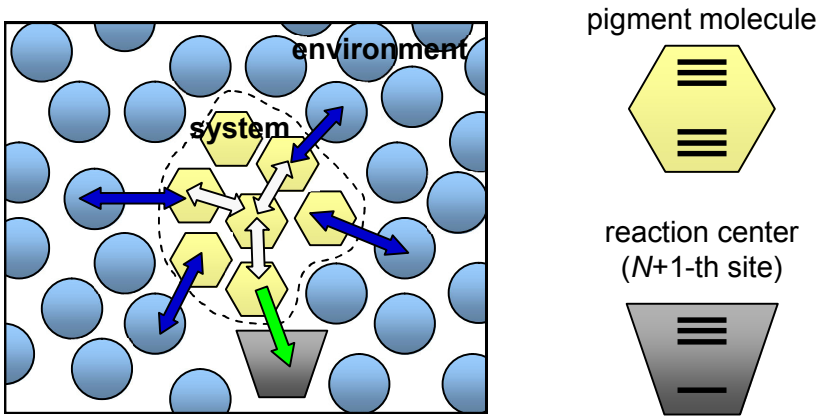

Figure 3.1: General scheme of the model arrangement. The system is built up of N pigment molecules (sites) (yellow hexagons), which are coupled to each other, to the reaction center ($N+1$-th site) (gray trapezoid), and to the surrounding molecules (blue circles).

4. To assess the efficiency of energy transfer, I introduce an extra, $N+1$-th site, which acts as an incoherent energy sink [45], [52], [54], [70]. This site corresponds to the reaction center, where the exciton energy is trapped by charge separation [88].

Several of the articles cited in Sec. 2.5 applied vibronic models [41], [42], [45]–[47], [50], [52] (resembling feature #1), some considering the Franck–Condon overlap integrals as well [40], [44], [48], [49], [53], [54]. Combining these two features with the third and fourth ones enables the direct investigation of how vibrational relaxation influences the energy transfer efficiency.

I was about to finish this project when I discovered Ref. [45] and Ref. [54]. The models applied in these papers resemble mine in many aspects. Nevertheless, the model in the first paper contains no more than one intramolecular vibrational mode with two levels, which means that there is only one extra state compared to a purely electronic model. The second paper, in turn, applies a more complicated model to describe the system–bath interaction than I do, which corresponds to pure dephasing, that is, this model model does not reckon with longitudinal damping.

3.2 Basis of the Hilbert space

Applying the Born–Oppenheimer approximation, I express the vibronic basis states of each site i as the product of its electronic and vibrational eigenstates [89], *i.e.*, $\left|\varphi_{\varepsilon\nu}^{(i)}\right\rangle = \left|\phi_{\varepsilon}^{(i)}\right\rangle \left|\chi_{\varepsilon\nu}^{(i)}\right\rangle$, where I have omitted the tensor product operator $\otimes$ for the sake of simplicity; $\varepsilon = \{g, e\}$ denotes the ground or excited electronic state, and ν indicates the

DOI:10.15774/PPKE.ITK.2018.009

vibrational states, out of which I consider the $V^{(i)}$ lowest ones during the simulations (*i.e.*, $\nu = 0, 1, \ldots, V^{(i)} - 1$). (The notations of states are summarized in Table A.1 of the Appendix.) The vibrational mode is modeled as a harmonic oscillator. The shape of the potential surface and thus the frequency of the harmonic oscillator are assumed to be independent of the electronic state (*i.e.*, $\omega_{vib}^{(i,g)} = \omega_{vib}^{(i,e)} = \omega_{vib}^{(i)}$); however, the potential surface of the harmonic oscillator can be shifted when the site is in the excited electronic state with respect to the case when it is in the ground electronic state (Fig. 3.2). The vibrational eigenenergies as well as the vibrational eigenstates belonging to the ground and excited electronic states are given as

$$E_{g\nu}^{(i)} = E_{e\nu}^{(i)} = \hbar\omega_{vib}^{(i)}\left(\nu + \frac{1}{2}\right), \tag{3.1}$$

$$\chi_{g\nu}^{(i)}(x) = N_{\nu}^{(i,g)} H_{\nu}(\xi) \exp\left(-\frac{\xi^2}{2}\right), \tag{3.2}$$

$$\chi_{e\nu}^{(i)}(x) = N_{\nu}^{(i,e)} H_{\nu}(\xi - d) \exp\left(-\frac{\left(\xi - d^{(i)}\right)^2}{2}\right), \tag{3.3}$$

respectively [89], where $\xi = \alpha^{(i)} x$ is the dimensionless coordinate, and $d^{(i)} = \alpha^{(i)}\left(\Delta x^{(i)}\right)$ is the dimensionless displacement between the two potential surfaces. The latter is expressed as $d^{(i)} = \sqrt{2S^{(i)}}$ from Huang–Rhys factor $S^{(i)}$ [48]. (Since in the presented simulations I use the same Huang–Rhys factor S for each site, I will drop the index (i) from its notation.) In Eqs. (3.2) and (3.3), $H_{\nu}(\xi)$ denotes the ν-th Hermite polynomial, whereas

$$N_{g\nu}^{(i)} = N_{e\nu}^{(i)} = \sqrt{\frac{\alpha^{(i)}}{\sqrt{\pi} 2^{\nu} \nu!}} \tag{3.4}$$

stands for a normalization factor with $\alpha^{(i)} = (m^{(i)} k^{(i)}/\hbar^2)^{1/4}$. In the following, only the overlap integrals of the vibrational states will be needed (see Eq. (3.10)), in which $\alpha^{(i)}$ cancels. Consequently this coefficient can simply be set to 1, and it is needless to determine the value of the force constant $k^{(i)}$ and the mass $m^{(i)}$ of the vibrating particles.

An arbitrary state of the i-th site can be expressed as the linear combination $\left|\varphi^{(i)}\right\rangle = \sum_{\varepsilon=g,e} \sum_{\nu} c_{\varepsilon\nu}^{(i)} \left|\varphi_{\varepsilon\nu}^{(i)}\right\rangle$ of its vibronic basis states. I assume that there is no electron transfer between the sites; therefore, the wave functions of different sites do not overlap, and the basis vectors of the system can be constructed as $|\Psi_m\rangle = \left|\varphi_p^{(1)}\right\rangle \otimes \left|\varphi_q^{(2)}\right\rangle \otimes \ldots \otimes \left|\varphi_s^{(N)}\right\rangle \otimes \left|\varphi_t^{(N+1)}\right\rangle$, where p, q, $\ldots$, s, t run over the basis vectors of sites 1, 2, $\ldots$, $N+1$,

DOI:10.15774/PPKE.ITK.2018.009

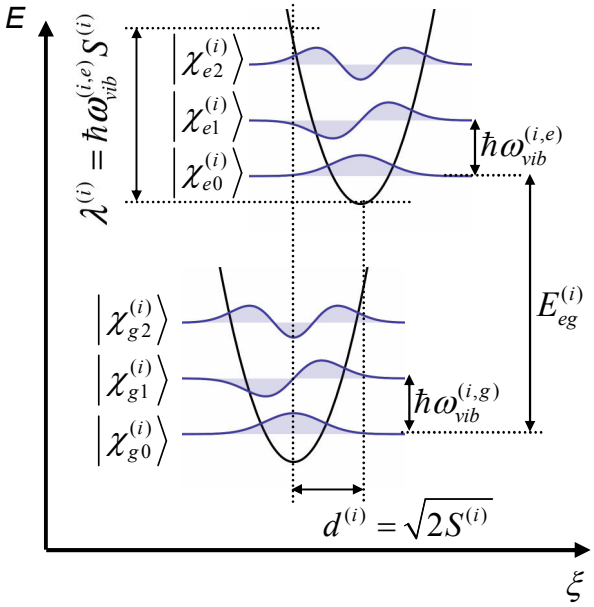

Figure 3.2: Vibrational states of the i-th site. Each site has two electronic states (namely a ground and an excited state), coupled with a vibrational mode, which is modeled as a harmonic oscillator. The shape of the potential surface and thus the frequency of the harmonic oscillator are assumed to be independent of the electronic state (*i.e.*, $\omega_{vib}^{(i,g)} = \omega_{vib}^{(i,e)} = \omega_{vib}^{(i)}$); however, there is a displacement $d^{(i)}$ between the potential surfaces belonging to the ground and to the excited electronic state. The horizontal axis depicts the dimensionless space coordinate ξ. $E_{eg}^{(i)}$, $\lambda^{(i)}$, and $S^{(i)}$ denote the site energy, the reorganization energy, and the Huang–Rhys factor, respectively. [1]

respectively. Thus, the basis vectors of the system can be represented by a tuple formed of $N+1$ elements, each expressing the state of a site.

To reduce the dimension of the state space, I restrict this set to the single-exciton basis, which is composed of those state vectors in which at most one site is in the excited electronic state. This simplification is justified by the idea that I aim to simulate the transfer of one exciton, being present at the beginning at a predefined starting site, for instance, site 1. Accordingly, I choose $|\Psi(0)\rangle = \left|\varphi_{e0}^{(1)}, \varphi_{g0}^{(2)}, \ldots, \varphi_{g0}^{(N+1)}\right\rangle$ as the initial state of the system at zero temperature. (For the initial state at nonzero temperature, see Sec. 5.5.2.) Assuming that the site energies are of the same order of magnitude, the system does not contain enough energy to reach a double-exciton state.

In the case of the simulations performed on the heptamer model, I apply the two-particle approximation, meaning that I narrow the state space even more to those configurations in which there is one electronically excited site, and among the other sites (being in the ground electronic state) there is at most one that is vibrationally excited [54], [90].

DOI:10.15774/PPKE.ITK.2018.009

3.3 Master equation

To describe the time-evolution of the system, I use the Lindblad master equation (2.55). Thus, assuming that $\hat{H}_{LS} = 0$, the master equation expressing the time evolution of the density matrix $\hat{\rho}_S$ of model system takes the form

$$\frac{\mathrm{d}}{\mathrm{d}t}\hat{\rho}_S(t) = -\frac{\mathrm{i}}{\hbar}\left[\hat{H}_S, \hat{\rho}_S(t)\right] + \sum_j \gamma_j \left(\hat{A}_j \hat{\rho}_S(t)\, \hat{A}_j^\dagger - \frac{1}{2}\hat{A}_j^\dagger \hat{A}_j \hat{\rho}_S(t) - \frac{1}{2}\hat{\rho}_S(t)\, \hat{A}_j^\dagger \hat{A}_j\right). \quad (3.5)$$

I recall that in Eq. (3.5) $\hat{H}_S$ denotes the Hamiltonian of the system, which contains the electronic and the vibrational energies as well as the couplings between the sites, and which determines the unitary (coherent) dynamics of the system (see Sec. 3.4). On the other hand, the Lindblad operators $\hat{A}_j$ together with the rate constants γ_j—following Ref. [91], I will refer to their contracted forms, $\hat{C}_j = \sqrt{\gamma_j}\hat{A}_j$, as "collapse operators"—formulate the environment-induced, non-unitary (incoherent) evolution. My model involves five types of incoherent processes: the relaxation of the electronic state, the relaxation of the vibrational state (*i.e.*, the damping of the vibrational modes), the excitation of the vibrational state (at nonzero temperature), pure dephasing, and the sink effect of the reaction center. (The first four are explicated in Sec. 3.5; the last one, in Sec. 3.6).

I determine the population of state $\left|\varphi_{e\nu}^{(i)}\right\rangle$ (*i.e.*, the probability that the i-th site is in the excited electronic state and in vibrational state ν) from the density matrix as

$$P_{e\nu}^{(i)} = \sum_{|\Psi_m\rangle \in \left\{\ldots\otimes\left|\varphi_{e\nu}^{(i)}\right\rangle\otimes\ldots\right\}} \langle\Psi_m|\,\hat{\rho}\,|\Psi_m\rangle\,, \quad (3.6)$$

where the summation is performed on all the basis states $|\Psi_m\rangle$ in which the i-th site is in state $\left|\varphi_{e\nu}^{(i)}\right\rangle$, while the state of other sites is arbitrary. Similarly, the probability that the i-th site is in the excited electronic state regardless of its vibrational state (*i.e.*, the site population) is calculated as

$$P_e^{(i)} = \sum_\nu \sum_{|\Psi_m\rangle \in \left\{\ldots\otimes\left|\varphi_{e\nu}^{(i)}\right\rangle\otimes\ldots\right\}} \langle\Psi_m|\,\hat{\rho}\,|\Psi_m\rangle = \sum_\nu P_{e\nu}^{(i)}. \quad (3.7)$$

DOI:10.15774/PPKE.ITK.2018.009

3.4 Unitary evolution: the Hamiltonian of the system

I define the Hamiltonian occurring in Eq. (3.5) as

$$\hat{H}_S = \sum_{i=1}^{N} E_{eg}^{(i)} \hat{a}^{(i)\dagger} \hat{a}^{(i)} + \sum_{i=1}^{N} \hbar\omega_{vib}^{(i)} \hat{b}^{(i)\dagger} \hat{b}^{(i)} + \sum_{m,n} J_{nm} \left|\Psi_n\right\rangle \left\langle\Psi_m\right| . \tag{3.8}$$

The first and second terms on the right side express the energies of the electronic and the vibrational states, respectively (omitting the zero-point energy $\hbar\omega_{vib}^{(i)}/2$ from Eq. (3.1)). They are expressed by means of the annihilation (creation) operators $\hat{a}^{(i)}$ and $\hat{b}^{(i)}$ ($\hat{a}^{(i)\dagger}$ and $\hat{b}^{(i)\dagger}$), acting on the electronic and on the vibrational states of the i-th site, respectively, and are represented by diagonal matrices. In the above equation, $E_{eg}^{(i)}$ denotes , while $\hbar\omega_{vib}^{(i)}$ is the energy quantum of the vibrational mode. (In the presented simulations, I use the same vibrational frequency for each site and thus I will drop the index (i) from the notation.)

The third, off-diagonal term of Eq. (3.8) formulates the coupling between vibronic basis states $|\Psi_m\rangle$ and $|\Psi_n\rangle$. Since I consider only dipole–dipole coupling in this study, the coupling strength J_{nm} is nonzero solely when $|\Psi_m\rangle$ and $|\Psi_n\rangle$ differ from each other in the state of two sites, *e.g.,* A and B, so that

$$\begin{aligned} |\Psi_m\rangle &= \left|\ldots, \varphi_{e\nu}^{(A)}, \ldots, \varphi_{g\mu}^{(B)}, \ldots\right\rangle, \\ |\Psi_n\rangle &= \left|\ldots, \varphi_{g\nu'}^{(A)}, \ldots, \varphi_{e\mu'}^{(B)}, \ldots\right\rangle, \end{aligned} \tag{3.9}$$

where the ellipses $(\ldots)$ denote sites being in the same state in $|\Psi_m\rangle$ and $|\Psi_n\rangle$. Thus, when the system goes through the transition $|\Psi_m\rangle \to |\Psi_n\rangle$, the energy is transferred from site A (behaving as the donor) to site B (behaving as the acceptor), and vice versa in the case of the reverse transition (see Fig. 3.3(a)). Assuming that the Coulomb matrix element $J^{(AB)}$ (given as an input parameter) is independent of nuclear coordinates, the dipole–dipole coupling between states $|\Psi_m\rangle$ and $|\Psi_n\rangle$ can be expressed as

$$J_{nm} = J^{(AB)} \left\langle \chi_{g\nu'}^{(A)} \middle| \chi_{e\nu}^{(A)} \right\rangle \left\langle \chi_{e\mu'}^{(B)} \middle| \chi_{g\mu}^{(B)} \right\rangle, \tag{3.10}$$

where the inner products of the vibrational states are known as Franck–Condon overlap integrals [65]. Since the shape of the potential surface of the harmonic oscillator and thus the shape of the vibrational wave functions are assumed to be independent of the electronic state, the overlap integral of a given pair of states depends solely on

DOI:10.15774/PPKE.ITK.2018.009

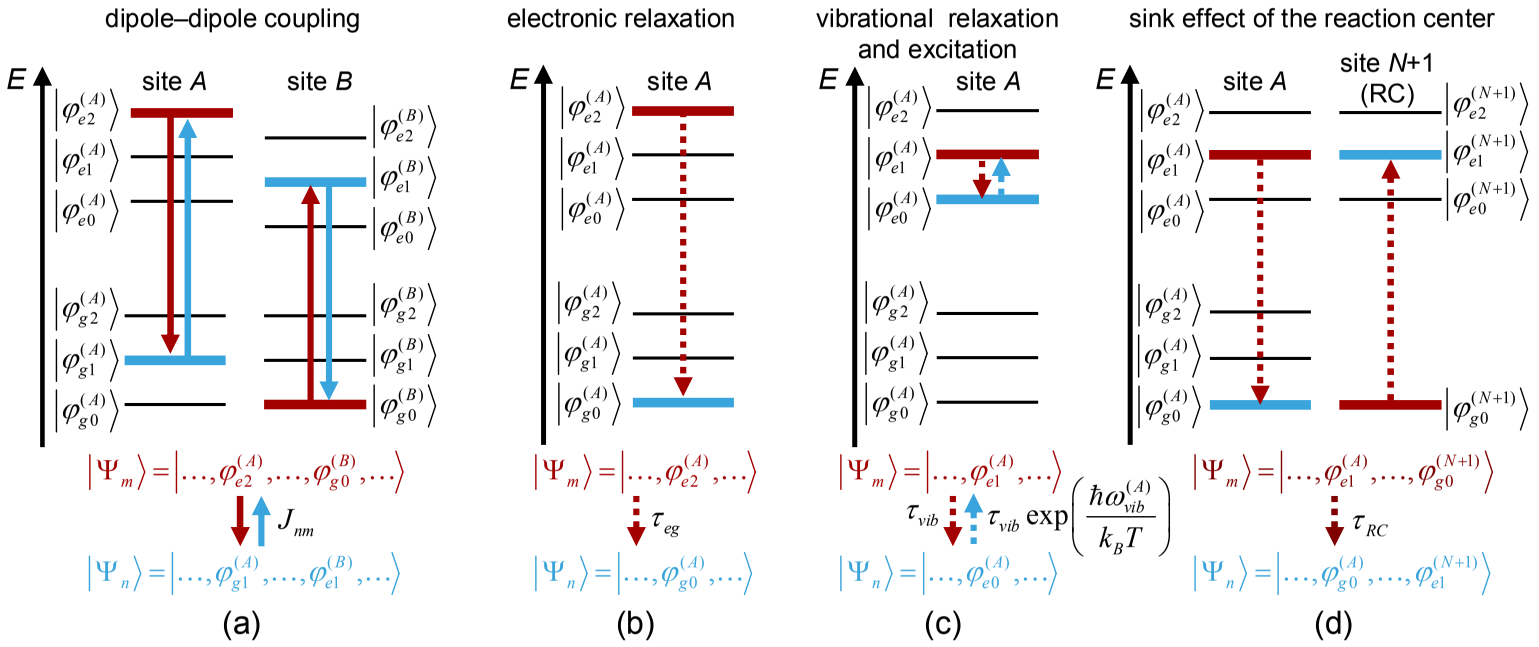

Figure 3.3: Types of state transitions occurring in the model. (a): Dipole–dipole coupling between states $|\Psi_m\rangle$ and $|\Psi_n\rangle$. The red arrows denote a state transition during which site A goes from the excited to the ground electronic state, while site B, from the ground to the excited electronic state. Consequently, the exciton is transferred from site A to site B. The blue arrows denote the reverse process. (b)–(d): Non-unitary state transitions formulated by collapse operators. The interaction with the environment induces relaxation from the excited electronic state to (the lowest vibrational level of) the ground electronic state (b), as well as vibrational relaxation and excitation (c). The reaction center is modeled as an $N+1$-th site, behaving as an energy sink, which captures the exciton from a specified site A: while the latter site returns to the ground state, the sink site gets to the excited electronic state (d). There is also a fifth incoherent process that occurs in this study, namely, pure dephasing, during which coherences are damped, but population transition does not take place. Note that solid and dotted arrows indicate unitary (coherent) and non-unitary (incoherent) processes, respectively. Ellipsis (...) denotes sites whose state is not affected in the given transition; J_{nm} is the dipole–dipole coupling strength; τ_{eg}, τ_{vib}, and τ_{RC} are the time constants of the non-unitary processes. [1]

DOI:10.15774/PPKE.ITK.2018.009

the Huang–Rhys factor, as listed in Table A.2 of the Appendix for the three lowest vibrational eigenstates. Note that if the Huang–Rhys factor is zero, then the vibrational eigenstates are orthonormal and thus the Franck–Condon overlap integrals can be expressed as $\left\langle \chi^{(i)}_{g\nu'} \middle| \chi^{(i)}_{e\nu} \right\rangle = \delta_{\nu\nu'}$.

3.5 Non-unitary processes induced by the environment

I treat the environment as a heat bath, whose change due to the interaction with the system is negligible. Thus, I assume that the Born and Markov approximations, presented in Secs. 2.8.2 and 2.8.3, are reasonable. I model the effect of the bath on the system as incoherent electronic and vibrational relaxation and—if the temperature is higher than zero—vibrational excitation. (I neglect electronic excitation since the corresponding energy gaps are much larger than the product k_BT of the Boltzmann constant and the temperature.) I describe these transitions by collapse operators defined as

$$\hat{C}_{nm} = \sqrt{\gamma_{nm}}\hat{A}_{nm} = \sqrt{\gamma_{nm}}\,|\Psi_n\rangle\langle\Psi_m|\,, \tag{3.11}$$

where $\hat{A}_{nm} = |\Psi_n\rangle\langle\Psi_m|$ $(m \neq n)$ denote Lindblad operators. In the Lindblad equation (3.5), each collapse operator formulates the exponential decay of population $\hat{\rho}_{m,m}$ to population $\hat{\rho}_{n,n}$ with time constant $\tau_{nm} = \gamma_{nm}^{-1}$ as well as the decay of all the off-diagonal elements (coherences) in the m-th row and in the m-th column of the density matrix as it is shown in Eq. (A.1) of the Appendix. Thus, each collapse operator $\hat{C}_{nm}$ results in a transition $|\Psi_m\rangle \to |\Psi_n\rangle$ together with dephasing.

Note that the presented model does not contain any random steps as it treats the stochastic effects of the environment on the system on population average.[2]

3.5.1 Electronic relaxation

Electronic relaxation gets the electron from the excited to the ground electronic state. To model this process, I define an incoherent transition $|\Psi_m\rangle \to |\Psi_n\rangle$ for each pair of states that differ from each other only in the state of site A, so that $|\Psi_m\rangle = \left|\ldots, \varphi^{(A)}_{e\nu}, \ldots\right\rangle$ and $|\Psi_n\rangle = \left|\ldots, \varphi^{(A)}_{g0}, \ldots\right\rangle$ (Fig. 3.3(b)). (Note that, for simplicity, all these transitions lead to the ground vibrational state, that is, some of them involves vibrational relaxation

[2] In contrast, in the so called Monte Carlo method, the effect of the environment is modeled by instantaneous state transitions occurring in randomly chosen time steps of the simulation. The shorter the time constant of a transition, the more probable that the transition occurs in a given time step. In principle, repeating the simulation many times, the average of the results approaches to the result of the single run of the population-average-based simulation.

DOI:10.15774/PPKE.ITK.2018.009

as well.) These transitions are formulated by collapse operators $\hat{C}_{nm} = \sqrt{\gamma_{nm}}\,|\Psi_n\rangle\langle\Psi_m|$, where γ_{nm} is the inverse of τ_{eg}, which is in turn the time constant of the electronic relaxation: an input parameter, chosen for the sake of simplicity to be the same for each site and vibrational state ν.

3.5.2 Vibrational relaxation and vibrational excitation

In a harmonic oscillator, selection rules allow transitions only between neighboring states, for which $\Delta\nu = \pm 1$ [92]. For each pair of states that differ from each other only in the vibrational state of site A, so that $|\Psi_m\rangle = \left|\ldots, \varphi^{(A)}_{\epsilon\nu}, \ldots\right\rangle$ and $|\Psi_n\rangle = \left|\ldots, \varphi^{(A)}_{\epsilon\nu-1}, \ldots\right\rangle$, I define a collapse operator $\hat{C}_{nm} = \sqrt{\gamma_{nm}}\,|\Psi_n\rangle\langle\Psi_m|$, which expresses the vibrational relaxation $|\Psi_m\rangle \to |\Psi_n\rangle$ (Fig. 3.3(c)). I assume that the rate constant γ_{nm} of the vibrational relaxation is proportional to $\left|\left\langle \chi^{(A)}_{\varepsilon\nu-1}\right|\hat{\mu}\left|\chi^{(A)}_{\varepsilon\nu}\right\rangle\right|^2$, where the inner product is the transition dipole moment of the involved vibrational states, being proportional to $\sqrt{\nu}$ [92]. Thus, the rate constant of the vibrational relaxation is given as $\gamma_{nm} = \nu\tau_{vib}^{-1}$, where the time constant τ_{vib} is an input parameter, assumed to be temperature-independent and chosen to be the same for each site and both electronic states.

If the temperature is nonzero, the reverse transition, *i.e.*, vibrational excitation $|\Psi_n\rangle \to |\Psi_m\rangle$, also takes place. This process is formulated by the collapse operator $\hat{C}_{mn} = \sqrt{\gamma_{mn}}\,|\Psi_m\rangle\langle\Psi_n|$. Considering that the state populations in thermal equilibrium follow the Boltzmann distribution, the rate constant of the vibrational exciton can be expressed as

$$\gamma_{mn} = \gamma_{nm} \exp\left(-\frac{\hbar\omega_{vib}}{k_B T}\right). \tag{3.12}$$

3.5.3 Pure dephasing

Let us replace each collapse operator $\hat{C}_{nm}$ and $\hat{C}_{mn}$ introduced in Sec. 3.5.2 with $\hat{C}^{\times}_{nm} = \sqrt{\gamma_{nm}}\,|\Psi_m\rangle\langle\Psi_m|$ and $\hat{C}^{\times}_{mn} = \sqrt{\gamma_{mn}}\,|\Psi_n\rangle\langle\Psi_n|$, respectively, setting the rate constant $\gamma_{nm} = \nu\tau_{pd}^{-1}$ to the same value as in Sec. 3.5.2 (*i.e.*, $\tau_{pd} = \tau_{vib}$). The new operators formulate pure dephasing: they damp the off-diagonal elements of the density matrix exactly like the original collapse operators; however, they do not induce population transfer (compare Eqs. (A.1) and (A.2) of the Appendix). In this study, I apply such operators only in five simulation cases (indicated with "×" behind their number), namely to determine how dephasing pertaining to vibrational relaxation (and excitation) contributes to the investigated effects (see Secs. 5.4 and 6.2).

DOI:10.15774/PPKE.ITK.2018.009

3.5.4 Non-Markovian character of the vibrational degrees of freedom

In my model, most vibrational degrees of freedom are treated as components of a Markovian (memoryless) bath, but some of them (namely, the intramolecular vibrational modes) are modeled explicitly and thus have memory, which means that the description of the totality of the vibrations is non-Markovian. The coupling strength between a site and the bath (comprising all the vibrational degrees of freedom) is commonly expressed in the literature by the reorganization energy $\lambda^{(i)}$. In the present model, this coupling has two parts: the couplings between the electronic states of the sites and the explicit intramolecular vibrational modes, described by the Huang–Rhys factor $S^{(i)}$; and the couplings between the vibronic states of the system and the Markovian bath, causing vibrational relaxation and excitation, characterized by the time constant τ_{vib}. In the present approach, the reorganization energy is related to the Huang–Rhys factor as

$$\lambda^{(i)} = \hbar\omega_{vib}^{(i)} S^{(i)} \tag{3.13}$$

(see Fig. 3.2).

3.6 Reaction center acting as a sink—the measure of the energy transfer efficiency

Similarly to Refs. [45], [52], [70], I model the reaction center as an energy sink. I introduce it as an extra, $N+1$-th site, having a ground electronic state with one vibrational level and an excited electronic state with as many vibrational levels as the specified site A has. The energy levels of the energy sink site correspond to those of site A. The sink site is not exposed to environment-induced transitions, nor is it coupled to any of the "normal" sites through the off-diagonal elements of the Hamiltonian, but it is linked exclusively to site A via collapse operators $\hat{C}_{nm} = \sqrt{\gamma_{RC}}\,|\Psi_n\rangle\langle\Psi_m|$ constructed for every pair of basis states for which

$$\begin{aligned} |\Psi_m\rangle &= \left|\ldots, \varphi_{e\nu}^{(A)}, \ldots, \varphi_{g0}^{(N+1)}\right\rangle, \\ |\Psi_n\rangle &= \left|\ldots, \varphi_{g0}^{(A)}, \ldots, \varphi_{e\nu}^{(N+1)}\right\rangle, \end{aligned} \tag{3.14}$$

where the state of the sites denoted by ellipses is the same in $|\Psi_m\rangle$ and $|\Psi_n\rangle$. These collapse operators formulate transitions $|\Psi_m\rangle \to |\Psi_n\rangle$, during which the exciton energy is transferred irreversibly from the system to the sink site (Fig. 3.3(d)). Consequently,

DOI:10.15774/PPKE.ITK.2018.009

the time-evolution of the population $\hat{\rho}_{n,n}$ of state $|\Psi_n\rangle$ will be a monotonically increasing function indicating the efficiency of energy transfer. To quantify the efficiency, I simply divide the expectation value of the energy stored by the sink site at time t by the energy being present initially at the starting site, say, site 1:

$$\eta(t) = \frac{\left\langle E^{(N+1)}(t) \right\rangle}{\left\langle E^{(1)}(0) \right\rangle}, \tag{3.15}$$

where

$$\left\langle E^{(i)}(t) \right\rangle = \mathrm{Tr}\left[\hat{\rho}\,(t)\left(E_{eg}^{(i)}\hat{a}^{(i)\dagger}\hat{a}^{(i)} + \hbar\omega_{vib}^{(i)}\hat{b}^{(i)\dagger}\hat{b}^{(i)}\right)\right]. \tag{3.16}$$

Evidently, the efficiency defined herein depends decisively on the time constant $\tau_{RC} = \gamma_{RC}^{-1}$ of the sink effect of the reaction center, which is one of the input parameters of the model.

The above presented model of the reaction center is slightly modified in the case of the heptamer, discussed in Chapter 6: first, there are two "normal" sites there that are coupled to the sink site; and second,—since in the two-particle approximation those configurations in which one or more "normal" sites are vibrationally excited, but none of them is in the excited electronic state are excluded from the Hilbert space—all the "normal" sites ($i = 1, 2, \ldots, 7$) are in the ground state both electronically and vibrationally in state $|\Psi_n\rangle$ appearing in Eq. (3.14).

DOI:10.15774/PPKE.ITK.2018.009

Chapter 4

Implementation of the Simulation Software

4.1 Outline of the simulation algorithm

Following the model delineated in the previous chapter, I implemented a simulation software, which determines the state dynamics of the model system by solving the Lindblad equation (3.5) numerically. I wrote the program code in *Python* making use of *Quantum Toolbox in Python (QuTiP)* [91], [93] (version 3.1.0), an open-source, well documented library, widely used in the scientific community[1].

The algorithm consists of the following major steps:

1. Reading the input parameters[2] from a csv file.
2. Determination of the basis states.
3. Construction of the matrices representing the operators listed in the next step.
4. Running *QuTiP*'s Lindblad equation solver

   `mesolve(H, rho0, tlist, c_ops, e_ops)`,

   where `H` is the Hamiltonian of the system (denoted by $\hat{H}_S$ in Eq. 3.5), `rho0` is the density matrix of the initial state ($\hat{\rho}(0)$), and `c_ops` denotes the applied collapse operators ($\hat{C}_j$). The function returns the state populations selected by the evaluation operators `e_ops`, in time instances enumerated in `tlist`.
5. Construction of diagrams, saving the results to files.

[1] For a list of papers using *QuTiP*, see `http://qutip.org/users.html`.
[2] The input parameters are listed in Tables 5.1, 5.2, 6.1, and 6.2.

DOI:10.15774/PPKE.ITK.2018.009

4.2 Verification of the implemented simulator program

Based on the widespread use of *QuTiP*, I assumed that its built-in Lindblad equation solver works correctly. On the other hand, to verify the correctness of my own simulation program, I checked in several test cases whether the matrices generated by the program correspond to the ones specified by the model.

DOI:10.15774/PPKE.ITK.2018.009

Chapter 5

Simulation Results on Dimers

5.1 Outline of the chapter

In this chapter, first I investigate on dimer model systems how the presence of an undamped intramolecular vibrational mode affects the energy transfer (Sec. 5.2). Then, I study the impact that the damping of the vibrational mode exerts on the transfer (Sec. 5.3). Afterwards, I compare the influence of vibrational relaxation and pure dephasing (Sec. 5.4), and I close the chapter examining the scope of the effects presented in the previous sections (Sec. 5.5).

I performed the simulations presented in this chapter on various dimer arrangements (*i.e.*, $N = 2$), considering the $V = 3$ or 5 lowest levels of the vibrational modes (see Table 5.1 and Fig. 5.1). The efficiencies of the different model systems are compared based on $\eta(2\,\mathrm{ps})$, that is, the proportion of energy that arrives to the reaction center within 2 ps (see Eq. (3.15)). The simulation cases are listed in Table 5.2. Relying on data published in the literature, I endeavored to use parameters that fall into the physically relevant range. However, the chosen values do not belong to any particular photosynthetic complex since my aim in this chapter is to reveal some general characteristics of the energy transfer process.

DOI:10.15774/PPKE.ITK.2018.009

Table 5.1: List of dimer ($N = 2$) arrangements applied in the simulations. $E_{eg}^{(i)}$: energy difference between the excited and the ground electronic state of the i-th site, $\hbar\omega_{vib}$: energy quantum of the vibrational modes (same for each site), $J^{(12)}$: strength of dipole–dipole coupling between sites 1 and 2, S: Huang–Rhys factor (same for each site, dimensionless), τ_{vib}: time constant of vibrational relaxation (same for each site; ∞ means that the transition is blocked). Asterisk (*) after the roman numeral of the arrangement denotes that the sites are subject to vibrational relaxation and—if the temperature is nonzero—vibrational excitation. Expressions "resonant" and "detuned" in the description of the arrangements refer to the electronic levels. See Fig. 5.1 for the energy level diagrams of the arrangements. [1]

Arr.	Description	$E_{eg}^{(1)}$ (cm^{-1})	$E_{eg}^{(2)}$ (cm^{-1})	$\hbar\omega_{vib}$ (cm^{-1})	$J^{(12)}$ (cm^{-1})	S (1)	τ_{vib} (ps)
I	resonant dimer	15000	15000	300	100	0	∞
II	detuned dimer	15000	14700	300	100	0	∞
III	detuned dimer with undamped vibrational modes	15000	14700	300	100	0.5	∞
III*	detuned dimer with damped vibrational modes	15000	14700	300	100	0.5	0.2

In each arrangement, the reaction center is coupled to site 2.

5.2 Energy mismatch of the sites compensated by undamped intramolecular vibrational modes

Consider a system composed of two coupled sites, isolated from its environment at zero temperature. Let us assume that it is initially in the state $|\Psi(0)\rangle = \left|\varphi_{e0}^{(1)}\varphi_{g0}^{(2)}\right\rangle$ and that the frequencies of the vibrational modes of the two sites are the same ($\hbar\omega_{vib}^{(1)} = \hbar\omega_{vib}^{(2)} = \hbar\omega_{vib}$). In the resonant case, that is, when the site energies of the two coupled sites are equal ($E_{eg}^{(1)} - E_{eg}^{(2)} = \Delta E = 0\,\mathrm{cm}^{-1}$) (Arrangement I), the exciton oscillates back and forth between the sites, being present periodically with unit probability at site 1 and then at site 2 (sim. #1, Fig. 5.1(a)). If, however, the energy levels are detuned (Arrangement II), the amplitudes of the oscillations of the site populations and thus the degree of the "dislocation" of the exciton to site 2 will decrease (sim. #2, Fig. 5.1(b)). As the Huang–Rhys factors S of the sites are zero in the aforementioned simulation cases, the Franck–Condon overlap integrals $\left\langle \chi_{g\nu'}^{(i)} \middle| \chi_{e\nu}^{(i)} \right\rangle$ ($i = 1, 2$) are also zero for $\nu \neq \nu'$ because of the orthonormality of the vibrational eigenstates. Accordingly, the states with vibrational levels higher than 0 are unreachable from the initial state, which corresponds to the case when there are no intramolecular vibrational modes in the model.

DOI:10.15774/PPKE.ITK.2018.009

Table 5.2: List of simulations performed on dimers. Arr.: the index of the site arrangement (see Table 5.1 for details), V: number of vibrational states taken into consideration in each vibrational mode (same for each site), τ_{eg} : time constant of electronic relaxation (same for each site), τ_{RC}: time constant of the sink effect of the reaction center, T : temperature. Infinite time constant means that the transition is blocked (its rate constant is zero). Ellipsis (...) means parameter sweep, var./vars. denotes variant(s). [1]

Sim.	Arrangement	V	τ_{eg} (ps)	τ_{RC} (ps)	T (K)	Fig.
1	I	3 (1)[§]	∞	∞	0	5.1(a)
2	II	3 (1)[§]	∞	∞	0	5.1(b)
3	III	3	∞	∞	0	5.1(c), 5.2(a)
4[a)]	III*	3	∞	∞	0	5.1(d), 5.2(b)
5[b)]	I	3 (1)[§]	1.6	0.8	0	5.1(e), 5.3
6[b)]	II	3 (1)[§]	1.6	0.8	0	5.1(f)
7[b)]	III	3	1.6	0.8	0	5.1(g), 5.2(c), 5.3
8[a),b)]	III*	3	1.6	0.8	0	5.1(h), 5.2(d), 5.3
9a	III	5	1.6	0.8	0...400	5.5
9b	III*	5	1.6	0.8	0...400	5.5
9c	III var.[c)]	5	1.6	0.8	0...400	5.5
9d	III* var.[c)]	5	1.6	0.8	0...400	5.5
10a	III* vars.[d)]	5	1.6	0.8	0	5.6
10b	III* var.[d)]	5	1.6	0.8	300	5.6
11a	I	5	0.8	0.2...1.2	300	5.7(a)
11b	III	5	0.8	0.2...1.2	300	5.7(a)
11c	III*	5	0.8	0.2...1.2	300	5.7(a)
12a	I	5	1.6	0.2...1.2	300	5.7(b)
12b	III	5	1.6	0.2...1.2	300	5.7(b)
12c	III*	5	1.6	0.2...1.2	300	5.7(b)
13a	I	5	2.4	0.2...1.2	300	5.7(c)
13b	III	5	2.4	0.2...1.2	300	5.7(c)
13c	III*	5	2.4	0.2...1.2	300	5.7(c)
14a	III vars.[e)]	5	1.6	0.8	300	5.8(a)
14b	III* vars.[e)]	5	1.6	0.8	300	5.8(a)
15a	III vars.[f)]	5	1.6	0.8	300	5.8(b)
15b	III* vars.[f)]	5	1.6	0.8	300	5.8(b)
16a	III vars.[g)]	5	1.6	0.8	300	5.8(c)
16b	III* vars.[g)]	5	1.6	0.8	300	5.8(c)
17	I	5	1.6	0.8	300	5.8(a)–(c)

[§]: At zero temperature, when the Huang–Rhys factors of the sites are zero, only the lowest ($\nu = 0$) vibrational levels participate in the energy transfer, because the higher ones are unreachable from the initial state $|\Psi(0)\rangle$.

Modifications of the arrangements:

[a)]: sims. #4 and #8 were rerun as sims. #4[×] and #8[×], respectively, after substituting vibrational relaxation with pure dephasing of the same time constant (Figs. 5.4(a) and (b))

[b)]: sims. #5 to #8 were rerun after modifying either $E_{eg}^{(1)}$ and $E_{eg}^{(2)}$ by $\pm 5000\,\mathrm{cm}^{-1}$ or $J^{(12)}$ by $\pm 50\,\mathrm{cm}^{-1}$ (see Sec. 5.5.1; no figures are included)

[c)]: $E_{eg}^{(2)} = 14400\,\mathrm{cm}^{-1}$, $\hbar\omega_{vib} = \Delta E = 600\,\mathrm{cm}^{-1}$

[d)]: $\tau_{vib} = 0.1 \ldots 50\,\mathrm{ps}, \infty$

[e)]: $E_{eg}^{(2)} = 14950 \ldots 14000\,\mathrm{cm}^{-1}$, $\hbar\omega_{vib} = \Delta E = 50 \ldots 1000\,\mathrm{cm}^{-1}$

[f)]: $\hbar\omega_{vib} = 100 \ldots 600\,\mathrm{cm}^{-1}$ ($\Delta E = 300\,\mathrm{cm}^{-1}$ fixed)

[g)]: $S = 0 \ldots 1$

Initial state in each simulation case:

— if $T = 0\,\mathrm{K}$: $|\Psi(0)\rangle = \left|\varphi_{e0}^{(1)}, \varphi_{g0}^{(2)}; \varphi_{g0}^{(3)}\right\rangle$

— if $T > 0\,\mathrm{K}$: $|\hat{\rho}(0)\rangle$, describing the mixed state in which $\left|\varphi_{e\nu}^{(1)}\right\rangle$, $\nu = 0, 1, \ldots, V-1$, as well as $\left|\varphi_{g\mu}^{(2)}\right\rangle$, $\mu = 0, 1, \ldots, V-1$, are in thermal equilibrium, while the reaction center is in state $\left|\varphi_{g0}^{(3)}\right\rangle$.

DOI:10.15774/PPKE.ITK.2018.009

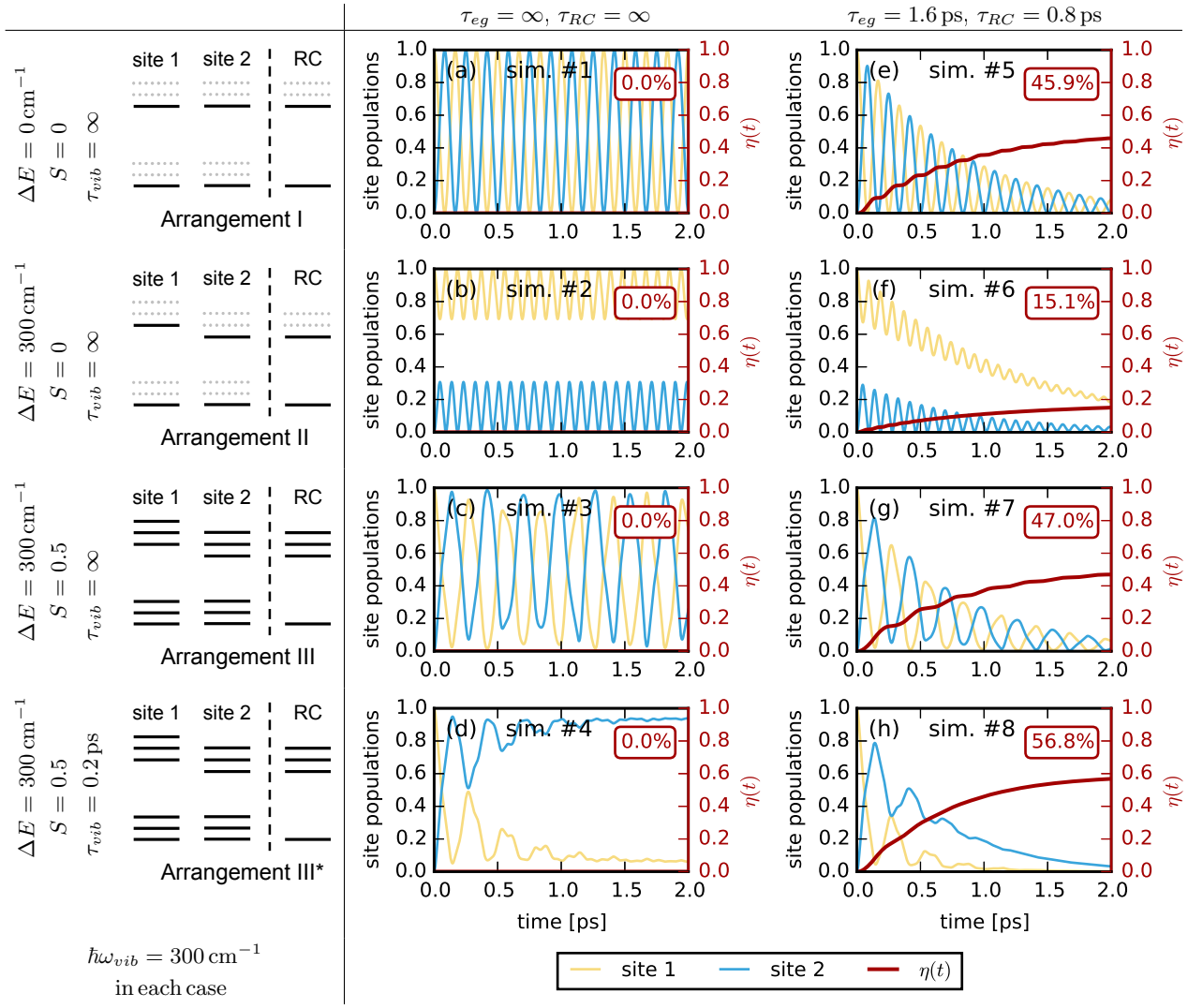

Figure 5.1: Dynamics of the exciton energy transfer in various dimer model systems at $T = 0\,\mathrm{K}$. Yellow and blue curves denote the occupation probabilities of the excited electronic states of sites 1 and 2 (*i.e.*, the site populations), respectively, while the thick red curve, rising monotonically, is the energy transfer efficiency $\eta(t)$. The numerical value in the top right corner of each plot is $\eta\,(2\,\mathrm{ps})$, that is, the proportion of the initial exciton energy that arrives at the reaction center by the end of the simulation. In Arrangements I and II, the states denoted by dotted lines are unreachable from the initial state because the Huang–Rhys factor is zero. In the energetically resonant dimer (Arrangement I), the exciton oscillates back and forth between sites 1 and 2 with maximum amplitude. If the electronic energy levels are detuned (Arrangement II), the degree of exciton transfer declines. This deterioration, however, can be compensated by intramolecular vibrational modes creating resonant vibronic levels at the two sites (Arrangement III). In Arrangement III*, vibrational relaxation traps the exciton at site 2, resulting in an enhanced energy transfer. The electronic relaxation and the energy absorbing effect of the reaction center are disabled in the simulations depicted in the left column and enabled in those ones that are presented in the right column. $\Delta E = E_{eg}^{(1)} - E_{eg}^{(2)}$: energy detuning between the electronic states of sites 1 and 2, S : Huang–Rhys factor, τ_{vib}, τ_{eg}, and τ_{RC}: time constants of vibrational relaxation, electronic relaxation, and the sink effect of the reaction center, respectively, $\hbar\omega_{vib}$: energy quantum of the intramolecular vibrational modes. See Tables 5.1 and 5.2 for the simulation parameters not indicated here. [1]

DOI:10.15774/PPKE.ITK.2018.009

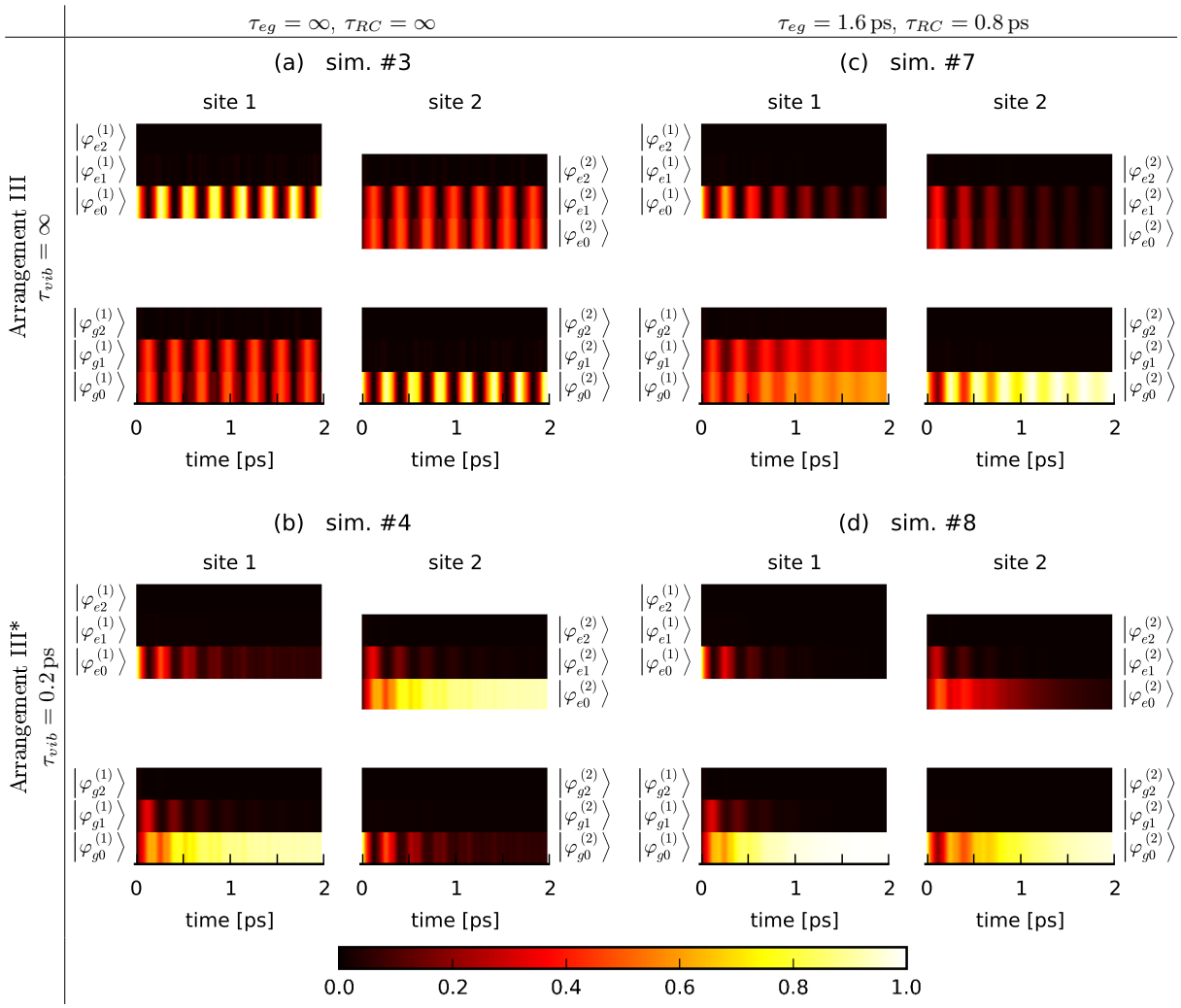

Figure 5.2: Occupation probabilities of the vibronic states of each site over time in dimers at $T = 0\,\mathrm{K}$ if the intramolecular vibrational modes are undamped (Arrangement III) or damped (Arrangement III*). The electronic relaxation and the energy absorbing effect of the reaction center are disabled in the simulations depicted in the left column and enabled in those ones that are presented in the right column. During vibrational-relaxation-enhanced exciton energy transfer (VREEET) (Arrangement III*), the population of state $\left|\varphi_{e0}^{(2)}\right\rangle$ is increased, indicating that the exciton gets stuck at site 2, which enables the reaction center to collect a larger proportion of the exciton energy. See Figs. 5.1(c), (d), (g), (h) for site populations as well as Tables 5.1 and 5.2 for the simulation parameters. [1]

DOI:10.15774/PPKE.ITK.2018.009

Several studies reported that vibrational modes with frequency close to the energy detuning of the electronic states of the two sites can promote the exciton transfer [43]–[50]. Indeed, if the Huang–Rhys factors of the sites are changed to 0.5 (Arrangement III), the amplitudes of the oscillations of the site populations almost reach unity again (sim. #3, Fig. 5.1(c)). Figure 5.2(a) shows the populations of the vibronic states of the two sites over time. The oscillations of the populations originate mainly in dipole–dipole coupling between energetically resonant vibronic states, namely between $\left|\varphi_{e0}^{(1)}\varphi_{g0}^{(2)}\right\rangle$ and $\left|\varphi_{g1}^{(1)}\varphi_{e0}^{(2)}\right\rangle$ as well as between $\left|\varphi_{e0}^{(1)}\varphi_{g0}^{(2)}\right\rangle$ and $\left|\varphi_{g0}^{(1)}\varphi_{e1}^{(2)}\right\rangle$. Both states $\left|\varphi_{g1}^{(1)}\right\rangle$ and $\left|\varphi_{e1}^{(2)}\right\rangle$ are populated considerably during the simulation, which implies that both transition $\left|\varphi_{e0}^{(1)}\right\rangle \leftrightarrow \left|\varphi_{g1}^{(1)}\right\rangle$ and transition $\left|\varphi_{g0}^{(2)}\right\rangle \leftrightarrow \left|\varphi_{e1}^{(2)}\right\rangle$ take place with significant probability. These transitions connect states of different vibrational levels of a site; therefore, they are allowed only if the Huang–Rhys factor of the given site is larger than zero so that the corresponding Franck–Condon overlap integral will be nonzero. If this condition is met, then the involved vibrational modes can compensate the energy mismatch of the electronic states. (Note that the frequency of the oscillation is proportional to the coupling strength of the states. The coupling strength is in turn proportional to the Franck–Condon overlap integrals (see Eq. (3.10)), which depend on the Huang–Rhys factors. This is why the frequency of the oscillations of the site populations are smaller in sim. #3 than in sim. #1.)

To assess the efficiency of the energy transfer, let us also consider now the electronic relaxation (acting on both sites) and the sink effect of the reaction center (acting on site 2), that is, two competing "energy output channels" resulting in the decay of the populations of the excited states. In the presented example model, 45.9% of the initial exciton energy arrives to the reaction center in 2 ps if the electronic energy levels of the two sites are resonant (sim. #5, Fig. 5.1(e)). By contrast, as expected, the detuning of the energy levels drastically deteriorates the energy transfer, resulting in an efficiency of only 15.1% (sim. #6, Fig. 5.1(f)). Nevertheless, the presence of an appropriate vibrational mode (with a frequency equivalent to the energy detuning of the sites, and a large Huang–Rhys factor) restores the efficiency of energy transfer to 47.0% (sim. #7, Fig. 5.1(g)). Looking at the population dynamics of the vibronic states (Fig. 5.2(c)), one can observe a shift towards the ground electronic states in comparison with the system isolated from its environment (Fig. 5.2(a)).

I note that the resonance between the vibrational modes and the detuning of the electronic levels of the coupled sites can in principle also result in the deterioration of the transfer efficiency if it conducts the exciton to a slower or even a blind path.

DOI:10.15774/PPKE.ITK.2018.009

5.3 Exciton transfer enhanced by the damping of intramolecular vibrational modes

In the presented model, in general, the energy of the exciton can reach the reaction center only across some specified site A, while all the sites are exposed to energy dissipation towards the environment. Therefore, the higher the probability (in time average) that site A is in the excited electronic state, the more probable that it is the reaction center that captures the energy of the exciton. That is to say, the optimal energy transfer efficiency could be reached if the exciton stayed at site A all the time. In this case, the efficiency of the energy transfer (supposing that the electronic energies of sites 1 and A are equal) would be

$$\eta_{opt}\left(t\to\infty\right)=\frac{\gamma_{RC}}{\gamma_{RC}+\gamma_{eg}}. \tag{5.1}$$

To approach this optimal value, the exciton has to be transferred as fast as possible to site A and kept there so that the reaction center can "absorb" its energy.

As shown above, the exciton oscillates back and forth among the sites if the system evolves unitarily, isolated from its environment (Figs. 5.1(a)–(c)). Similar but decaying oscillations characterize the systems that are exposed to electronic relaxation and the sink effect of the reaction center (Figs. 5.1(e)–(g)). However, these coherent oscillations become moderate if the intramolecular vibrational modes are damped (Arrangement III*), since vibrational relaxation induces dephasing and, moreover, can bring the exciton to a state that is energetically detuned from the states of the neighboring site. Consequently, the (back) transfer of the exciton from this state to the neighboring site is impeded. This is why the exciton is trapped in state $\left|\varphi_{e0}^{(2)}\right\rangle$ at site 2. If there is neither electronic relaxation nor sink effect in the system, the population of $\left|\varphi_{e0}^{(2)}\right\rangle$ approaches to a value close to 1 (sim. #4, Figs. 5.1(d) and 5.2(b)). If, however, these transitions are active, both sites finish in the ground state, but before then, the population of state $\left|\varphi_{e0}^{(2)}\right\rangle$ is all along increased (sim. #8, Figs. 5.1(h) and 5.2(d)) compared to the dimer with undamped vibrational modes (sim. #7, Figs. 5.1(g) and 5.2(c)). The elevated population of site 2, in turn, enables the reaction center to collect a larger proportion of the exciton energy. Accordingly, vibrational relaxation increases the efficiency of the energy transfer from 47.0% to 56.8%, which means a gain of 21%—a significant advance towards the optimal efficiency of 66.7%, calculated by Eq. (5.1) for the time constants applied in these simulations. (Compared to the resonant dimer, the increment is even slightly more,

DOI:10.15774/PPKE.ITK.2018.009

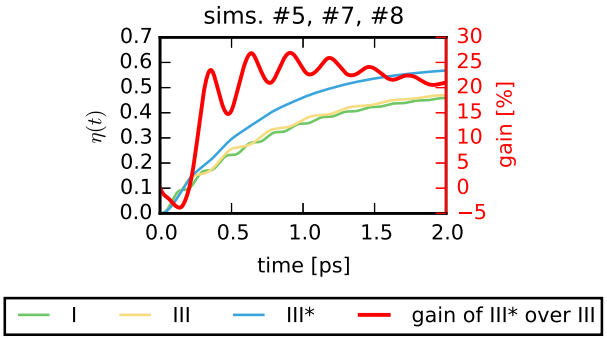

Figure 5.3: Efficiency of the energy transfer over time in the resonant dimer (Arrangement I), the detuned dimer with undamped vibrational modes (Arrangement III), and the detuned dimer with damped vibrational modes (Arrangement III*) at $T = 0\,\mathrm{K}$. The thick red curve depicts the gain caused by vibrational relaxation (scale on the right axis). See Tables 5.1 and 5.2 for the simulation parameters. [1]

namely 24%; whereas the poorly performing detuned dimer of zero Huang–Rhys factor is surpassed by the resonant dimer with damped vibrational modes by 276%.) From now on, I will refer to this kind of exciton propagation occurring in Arrangement III* as *vibrational-relaxation-enhanced exciton energy transfer (VREEET)*. To emphasize its degree, Figure 5.3 depicts the efficiency curves of different arrangements together.

5.4 Vibrational relaxation vs. pure dephasing

As described in Sec. 3.5, the collapse operators expressing vibrational relaxation (or excitation) $|\Psi_m\rangle \to |\Psi_n\rangle$ result both in population transfer from $\hat{\rho}_{m,m}$ to $\hat{\rho}_{n,n}$ and in the decay of the off-diagonal elements $\hat{\rho}_{i,m}$ and $\hat{\rho}_{m,i}$, $i \neq m$, *i.e.*, dephasing. To inspect in what degree the latter process in itself contributes to the enhancement of the energy transfer, I repeated sims. #4 and #8 replacing each of the aforementioned collapse operators with a new one that formulates pure dephasing according to Sec. 3.5.3. The obtained population dynamics are depicted in Figs. 5.4(a) and (b). I found that pure dephasing increased the efficiency of the energy transfer from 47.0% obtained for the undamped case (Fig. 5.1(g)) to 49.8% (Fig. 5.4(b)), while the dimer with damped modes performed at 56.8% (Fig. 5.1(h)). The difference between the two latter cases reveals the importance of the population transfer during vibrational relaxation in VREEET.

DOI:10.15774/PPKE.ITK.2018.009

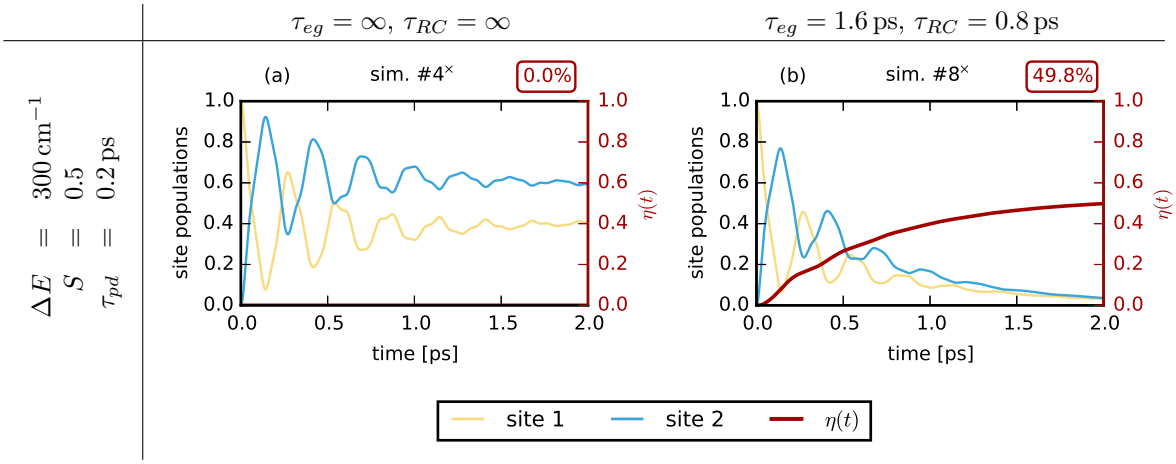

Figure 5.4: Dynamics of the exciton energy transfer in the dimer model system exposed to pure dephasing at $T = 0\,\mathrm{K}$ if electronic relaxation and the energy absorbing effect of the reaction center (a) do not or (b) do take place. η denotes the energy transfer efficiency. The numerical value in the top right corner of each plot is $\eta\,(2\,\mathrm{ps})$, that is, the proportion of the initial exciton energy that arrives at the reaction center by the end of the simulation. The simulations presented here are the modified versions of sims. #4 and #8: the collapse operators describing vibrational relaxation were replaced by new ones that formulate pure dephasing. The efficiency of the energy transfer in the system exposed to pure dephasing (49.8%) (Fig. 5.4(b)) is only slightly higher than the value obtained for the undamped case (47.0%) (Fig. 5.1(g)) and is much lower than the efficiency of the system with damped vibrational modes (56.8%) (Fig. 5.1(h)). These results demonstrate that vibrational relaxation surpasses pure dephasing in the enhancement of the exciton energy transfer. [1]

DOI:10.15774/PPKE.ITK.2018.009

5.5 Scope and robustness of vibrational-relaxation-enhanced exciton energy transfer

5.5.1 Dependence on the electronic energy levels and on the inter-pigment coupling

To inspect how the energy difference $E_{eg}^{(i)}$ between the excited and the ground electronic states of the sites as well as the coupling $J^{(ij)}$ between the sites influence the efficiency of the exciton transfer, I reran sims. #5 to #8 after the considerable modification either of $E_{eg}^{(1)}$ and $E_{eg}^{(2)}$ by $\pm 5000\,\mathrm{cm}^{-1}$ or of $J^{(ij)}$ by $\pm 50\,\mathrm{cm}^{-1}$ (no figures are included).

In each case, the parallel change of the electronic levels of the sites resulted in only a negligible change in the energy transfer efficiency ($\pm 2\%$ with respect to the "original" version of the simulation). In the case of the modified versions of sims. #5, #7, and #8, the impact of the alteration of the inter-pigment coupling strength on the efficiency was also little (the relative changes were $\pm 4\%$).[1] Consequently, the relative enhancement caused by the vibrational relaxation (sim. #8 vs. sim. #7) remained remarkable (between 16% and 22%).

On the other hand, the modified versions of sim. #6 revealed strong dependence on the inter-pigment coupling (setting $J^{(ij)}$ to $50\,\mathrm{cm}^{-1}$, $100\,\mathrm{cm}^{-1}$, and $150\,\mathrm{cm}^{-1}$ leaded to $\eta = 5.0\%$, 15.1%, and 23.9%, respectively). In this case, the electronic levels of the two sites were detuned from each other, which was not compensated by the intramolecular vibrational modes, either, as the Huang–Rhys factor S was zero. This resulted in a poor exciton transfer performance, which, however, could be somewhat compensated by a stronger inter-pigment coupling.

5.5.2 Dependence on the temperature

In the simulations presented up to this point, the temperature was set to zero, meaning that the initial state is a pure state ($\left|\varphi_{e0}^{(1)}, \varphi_{g0}^{(2)}\right\rangle$) and only vibrational relaxation can take place, while vibrational excitation does not occur. This setting resulted in simpler transfer dynamics, which facilitated the explanation of the phenomena. Next, I will investigate the dependence of the efficiency on the temperature, and then I will study the scope and robustness of VREEET by sweeping various model parameters at room temperature.

[1] However, the frequency of the oscillation of the exciton between the two sites varied proportionally to $J^{(12)}$.

DOI:10.15774/PPKE.ITK.2018.009

In my model, the Hamiltonian and the speed of vibrational relaxation are assumed to be temperature-independent, and the influence of the temperature on the transfer dynamics appears through the shift of the thermodynamic equilibrium. Accordingly, for nonzero temperatures, I specify the initial state of the system as a mixed state, in which the vibrational levels of each site—being in either the ground or excited electronic state—are in thermal equilibrium; moreover, together with vibrational relaxation, I also take vibrational excitation into consideration. At this point, I recall Eq. (3.12), which expresses the proportionality between the rates of these two opposite state transitions. With this in view, arrangements with damped vibrational modes (*i.e.*, whose vibrational relaxation time constant τ_{vib} is finite) are better to be called thermalizing arrangements, and those with undamped modes, non-thermalizing arrangements.

Figure 5.5 shows that the increase of the temperature reduces the efficiency of the exciton transfer in both non-thermalizing (sim. #9a) and thermalizing dimers (sim. #9b), while the significant advantage of the latter over the former remains, that is, VREEET occurs even at higher temperatures. Doubling the energy gap $\hbar\omega_{vib}$ between the vibrational levels together with the detuning between the electronic energy levels of the two sites (so that the equation $\Delta E = \hbar\omega_{vib}$ will still be valid) (sims. #9c and #9d) moderates the temperature dependence of the transfer efficiency. In non-thermalizing dimers, the temperature affects only the initial state, and the deterioration of the efficiency with increasing temperature is connected to the fact that I consider limited number of vibrational levels: the decline is intensified if the number of the vibrational levels taken into account is lower (not depicted in the figure). When thermalization also takes place, the rise of the temperature speeds up vibrational excitation, which, on the one hand, speeds up decoherence, and on the other hand, shifts thermal equilibrium and thus the "distribution" of the exciton between the two sites. In this case, considering fewer vibrational levels hardly affects the curves.

5.5.3 Dependence on the time constants of the incoherent processes

Figure 5.6 depicts the dependence of the efficiency of the energy transfer on the time constant τ_{vib} of the vibrational relaxation at 0 K and 300 K (sims. #10a–b). As expected, faster vibrational relaxation results in higher efficiency. For the given parameter set, the enhancement proves to be significant if τ_{vib} is shorter than a few picoseconds.

DOI:10.15774/PPKE.ITK.2018.009

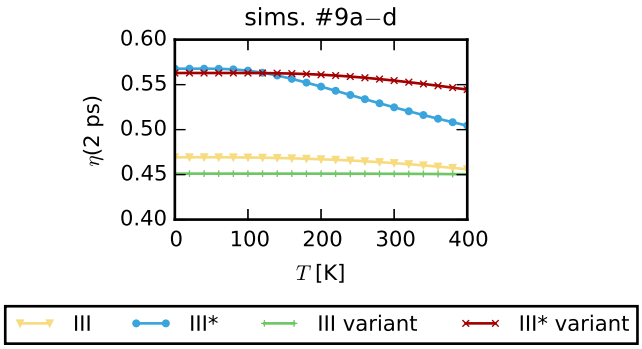

Figure 5.5: Dependence of energy transfer efficiency on the temperature in dimers if vibrational relaxation and excitation (*i.e.*, thermalization) do not (Arrangement III) or do occur (Arrangement III*). In the case of the "variants", the frequency of the intramolecular vibrational modes is doubled together with the detuning between the electronic energy levels of the two sites (so that the equation $\Delta E = \hbar\omega_{vib}$ will remain valid), which makes the exciton energy transfer less dependent on temperature. See Tables 5.1 and 5.2 for the simulation parameters. [1]

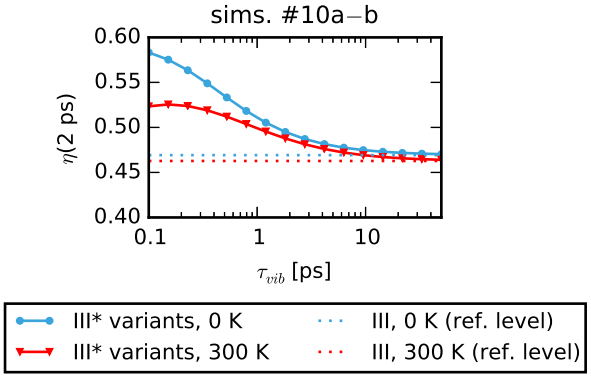

Figure 5.6: Dependence of energy transfer efficiency on the time constant τ_{vib} of the vibrational relaxation in dimers. The dotted lines depict the efficiencies in the undamped cases ($\tau_{vib} = \infty$) as references. See Tables 5.1 and 5.2 for the simulation parameters. [1]

DOI:10.15774/PPKE.ITK.2018.009

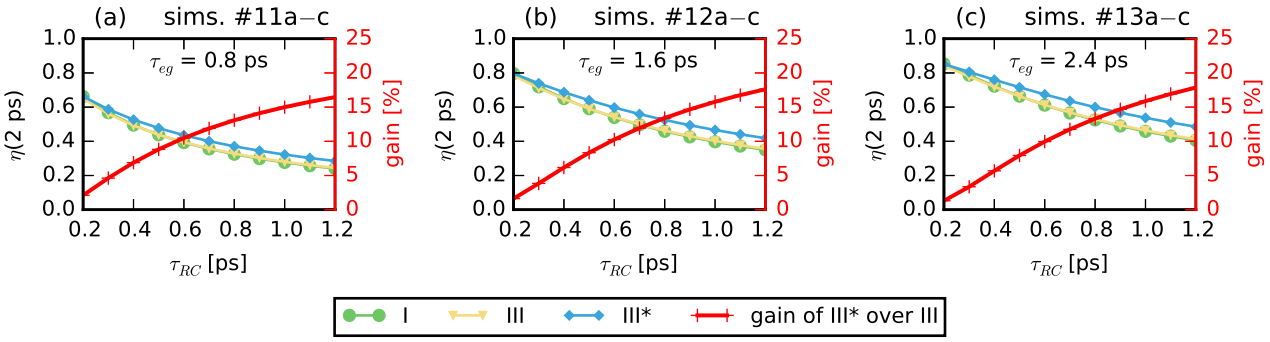

Figure 5.7: Dependence of the energy transfer efficiency on the time constants τ_{eg} and τ_{RC} of the electronic relaxation and the sink effect of the reaction center in dimers at $T = 300\,\mathrm{K}$. Arrangements I, III, and III* are the resonant dimer, the detuned dimer with undamped vibrational modes, and the detuned dimer with damped vibrational modes, respectively. The thick red curves depict the gain caused by vibrational relaxation (scale on the right axis). See Tables 5.1 and 5.2 for the simulation parameters. [1]

Obviously, τ_{eg} and τ_{RC} are decisive for the efficiency of the energy transfer: the slower the electronic relaxation and the faster the sink effect of the reaction center, the more efficient the energy transfer (sims. #11a–13c, Figs. 5.7(a)–(c)). When the reaction center absorbs the energy of the exciton quickly (τ_{RC} is small), there is little difference in the efficiency between the resonant dimer (Arrangement I), the detuned dimer with undamped vibrational modes (Arrangement III), and the detuned dimer with damped vibrational modes (Arrangement III*). However, if the sink is slow, and thus the energy transfer is less efficient, the relative advantage of the dimer with damped vibrational modes over the undamped case becomes significant. I set the time constant τ_{eg} of the electronic relaxation to three different values: the larger this parameter, the more energy arrives to the reaction center; nevertheless, the curves of the relative gain achieved by the damping of the vibrational modes are very similar in the three cases. The curve of the resonant dimer and that of the detuned dimer with undamped vibrational modes run close to one another regardless of τ_{RC} and τ_{eg}, demonstrating that the detuning of the electronic energy levels can be compensated by a resonant vibrational mode all over the investigated parameter range.

From another point of view, one can also interpret Figs. 5.7(a)–(c) in such a way that the system can reach the same energy transfer efficiency with a much slower reaction center if the sites are subject to vibrational relaxation.

DOI:10.15774/PPKE.ITK.2018.009

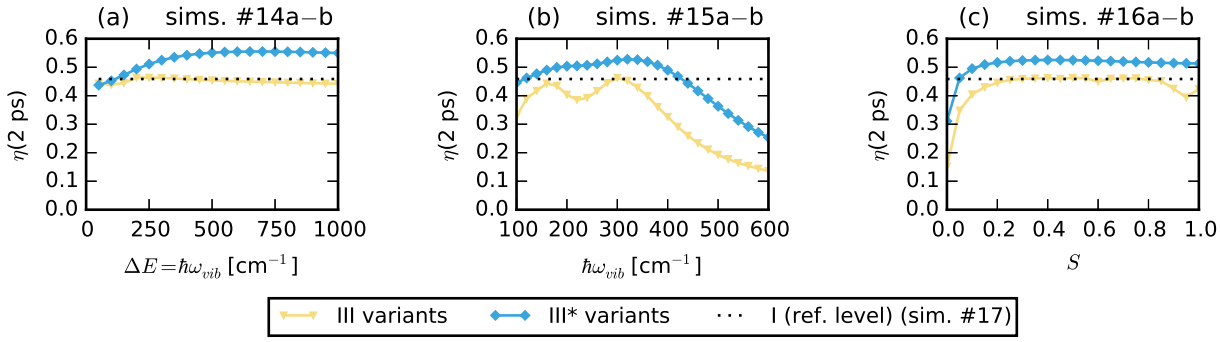

Figure 5.8: Dependence of the energy transfer efficiency in dimers at $T = 300\,\mathrm{K}$ (a) on the energy detuning ΔE between the electronic levels of sites 1 and 2 in the case when the energy quantum $\hbar\omega_{vib}$ of the vibrational mode is kept equal to it, (b) on the energy quantum $\hbar\omega_{vib}$ of the vibrational mode (in this case, ΔE is fixed to $300\,\mathrm{cm}^{-1}$), and (c) on the Huang–Rhys factor S; if the intramolecular modes are undamped (variants of Arrangement III) or damped (variants of Arrangement III*). The reference level, depicted by dotted line, is the efficiency of the resonant dimer (Arrangement I). See Tables 5.1 and 5.2 for the simulation parameters. [1]

5.5.4 Dependence on the detuning of the electronic energy levels

Let us modify now Arrangements III and III* by sweeping the energy detuning and the frequency of the vibrational mode simultaneously so that the energy levels of states $\left|\varphi_{e0}^{(1)}\right\rangle$ and $\left|\varphi_{e1}^{(2)}\right\rangle$ will coincide, or in other words, the equation $\Delta E = \hbar\omega_{vib}$ will be satisfied. For the damped case, energy transfer efficiency increases until $\Delta E = \hbar\omega_{vib} \approx 700\,\mathrm{cm}^{-1}$, then it declines slowly (sim. #14b, Fig. 5.8(a)). To interpret the curve, two factors are to be considered. On the one hand, the energy detuning between states $\left|\varphi_{e0}^{(1)}\right\rangle$ and $\left|\varphi_{e0}^{(2)}\right\rangle$ has to be large enough so that it can efficiently inhibit the back propagation of the exciton from site 2 to site 1. On the other hand, larger $\hbar\omega_{vib}$ means larger energy loss during the vibrational relaxation, which results in lower transfer efficiency. The comparison with the undamped case (sim. #14a) reveals that vibrational relaxation enhances the energy transfer by more than 20% in a wide range of parameter $\Delta E = \hbar\omega_{vib}$.

5.5.5 Dependence on the frequency of the vibrational modes

Figure 5.8(b) demonstrates the efficiency of energy transfer versus the energy quantum $\hbar\omega_{vib}$ of the vibrational modes, when the energy detuning ΔE between the electronic states of sites 1 and 2 is fixed to $300\,\mathrm{cm}^{-1}$ (sims. #15a–b). Optimal efficiency is obtained if $\hbar\omega_{vib}$ or—in the undamped case—$2\hbar\omega_{vib}$ is close to ΔE, meaning that $\left|\varphi_{e0}^{(1)}\right\rangle$ energetically matches $\left|\varphi_{e1}^{(2)}\right\rangle$ or $\left|\varphi_{e2}^{(2)}\right\rangle$, respectively. On the other hand, when $\hbar\omega_{vib}$ is considerably detuned from ΔE, the energy transfer is drastically deteriorated. Neverthe-

DOI:10.15774/PPKE.ITK.2018.009

less, vibrational relaxation boosts the energy transfer in the whole depicted range roughly by one tenth of the initial exciton energy.

5.5.6 Dependence on the Huang–Rhys factor

If the Huang–Rhys factor S is zero, then—because of the orthonormality of the vibrational eigenstates—transitions can occur only between the same vibrational levels of the two electronic states. Conversely, differing vibrational states of the two electronic states—that can participate in resonant transitions between neighboring sites—are coupled only if the Huang–Rhys factor is larger than zero (see Table A.2 of the Appendix). Accordingly, if S is close to zero, dimers with detuned electronic levels exhibit a very poor energy transfer efficiency (sims. #16a–b, Fig. 5.8(c); see also Fig. 5.1(f)) since in this case the couplings between the energetically resonant vibronic levels of the neighboring sites are very week. When, however, S gets larger than approximately 0.05, the coupling between the energetically resonant states $\left|\varphi_{e\nu}^{(1)}\right\rangle$ and $\left|\varphi_{e(\nu+1)}^{(2)}\right\rangle$ becomes strong enough to get the exciton easily to site 2, where it can relax to state $\left|\varphi_{e0}^{(2)}\right\rangle$, which makes the energy transfer in the dimer with damped vibrational mode more efficient than in the resonant dimer. After a steep increase, the curve starts to decline slowly around $S \approx 0.4$. Again, vibrational relaxation considerably enhances the energy transfer in a wide parameter range.

DOI:10.15774/PPKE.ITK.2018.009

Chapter 6

Simulation Results on an FMO-complex-inspired Heptamer

6.1 Outline of the chapter

To investigate the above effects in a more complex and more realistic system, I constructed a heptamer model inspired by the FMO complex of the green sulfur bacterium *Chlorobium tepidum*. I used the Hamiltonian published in Ref. [94] to define the site energies $E_{eg}^{(i)}$ and the dipole–dipole coupling strengths $J^{(ij)}$ between the sites (see Table 6.1). There are two main energy pathways in the FMO complex: one starts at BChl_1, the other, at BChl_6; and both end at BChl_3 and BChl_4 as these are the sites that are connected to the reaction center. (Accordingly, the extra site modeling the reaction center is coupled incoherently to both BChl_3 and BChl_4 by collapse operators. The energy levels of the extra site correspond to those of BChl_3. Thus, there is a minimal energy loss in my model when the reaction center absorbs energy from BChl_4.) I set the energy quantum of each intramolecular vibrational mode to $\hbar\omega = 180\,\mathrm{cm}^{-1}$(Ref. [94]), which is near to the differences between the electronic energy levels of the neighboring sites. Following Ref. [76], I set the constant τ_{eg} of the electronic relaxation to 250 ps, and the time constant τ_{RC} of the reaction center to 2.5 ps. During the simulations performed on the heptamer, I applied the two-particle approximation (see Sec. 3.2). Furthermore, to handle computational complexity, I limited the number of considered vibrational levels in both the ground and excited electronic states to four at BChl_3 and to three at all the other sites.

In the simulations presented hereunder, I varied three parameters: (i) the Huang–Rhys factor S of the sites, (ii) the time constant τ_{vib} of the vibrational relaxation, and (iii)

DOI:10.15774/PPKE.ITK.2018.009

Table 6.1: Parameters of the heptamer model ($N = 7$) inspired by the FMO complex. The site energies $E_{eg}^{(i)}$ (diagonal elements) and the dipole–dipole couplings $J^{(ij)}$ between the sites (off-diagonal elements) are defined in cm^{-1} by the Hamiltonian of *Chlorobium tepidum*, published in Ref. [94]. The dominant terms are written in bold. $V^{(i)}$: number of vibrational levels taken into account at the i-th site, $\hbar\omega_{vib}$: the energy quantum of the intramolecular vibrational mode (same for each site). [1]

	BChl_1	BChl_2	BChl_3	BChl_4	BChl_5	BChl_6	BChl_7
BChl_1	**12410**	**-87.7**	5.5	-5.9	6.7	-13.7	-9.9
BChl_2	**-87.7**	**12530**	**30.8**	8.2	0.7	11.8	4.3
BChl_3	5.5	**30.8**	**12210**	**-53.5**	-2.2	-9.6	6.0
BChl_4	-5.9	8.2	**-53.5**	**12320**	**-70.7**	-17.0	**-63.3**
BChl_5	6.7	0.7	-2.2	**-70.7**	**12480**	**81.1**	-1.3
BChl_6	-13.7	11.8	-9.6	-17.0	**81.1**	**12630**	**39.7**
BChl_7	-9.9	4.3	6.0	**-63.3**	-1.3	**39.7**	**12440**

$V^{(3)} = 4$; $V^{(i)} = 3$ for $i = 1, 2, 4, 5, 6, 7$[a)]

$\hbar\omega_{vib} = 180\,\mathrm{cm}^{-1}$ (Ref. [94])

The reaction center is coupled to sites 3 and 4; its energy levels correspond to those of site 3.

a): If both the temperature and the Huang–Rhys factors are zero, only the lowest ($\nu = 0$) vibrational levels participate in the energy transfer, because the higher ones are unreachable from the initial state $|\Psi(0)\rangle$.

the temperature T. I ran the simulations for 10 ps, a duration chosen arbitrarily. The simulation parameters are summarized in Table 6.2.

6.2 Population dynamics in some characteristic cases

Let us assume that the exciton is initially at site 6. If the Huang–Rhys factor is set to the relatively high value of 0.22 [94], and the time constant of the vibrational relaxation, to 1.5 ps (value chosen from the range given in Ref. [95]), then the FMO model exhibits a quite good efficiency at zero temperature (sim. #19, Fig. 6.1(b)), and it still performs well at 300 K (sim. #22, Fig. 6.1(e)). At both temperatures, changing the Huang–Rhys factor to zero deteriorates the exciton transfer drastically, since it ceases the coupling between the quasi-resonant vibronic states of the neighboring sites (sims. #18 and #21, Figs. 6.1(a) and (d)). "Turning off" the vibrational relaxation also decreases the efficiency considerably, especially at room temperature (sims. #20 and #23, Figs. 6.1(c) and (f)),

DOI:10.15774/PPKE.ITK.2018.009

Table 6.2: List of simulations performed on the FMO model. S: Huang–Rhys factor (same for each site), τ_{vib}: time constant of the vibrational relaxation (same for each site), T: temperature, τ_{eg}: time constant of electronic relaxation (same for each site), τ_{RC}: time constant of the sink effect of the reaction center. Infinite time constant means that the transition is blocked (its rate constant is zero). [1]

Sim.[a]	S (1)	τ_{vib} (ps)	T (K)	Fig.[e]
18 / 18'	0	1.5[d]	0	6.1(a) / A.1(a)
19[b] / 19'	0.22[c]	1.5[d]	0	6.1(b) / A.1(b)
20 / 20'	0.22[c]	∞	0	6.1(c) / A.1(c)
21 / 21'	0	1.5[d]	300	6.1(d) / A.1(d)
22[b] / 22'	0.22[c]	1.5[d]	300	6.1(e) / A.1(e)
23 / 23'	0.22[c]	∞	300	6.1(f) / A.1(f)
24[b] / 24'	0.22[c]	0.1 ... 500, ∞	300	6.4(a)
25 / 25'	0 ... 1.5	1.5[d]	300	6.4(b)
26 / 26'	0.22[c]	1.5[d]	0 ... 320	6.4(c)

In each simulation case:

— $\tau_{eg} = 250\,\text{ps}$, $\tau_{RC} = 2.5\,\text{ps}$ (Ref. [76]),

— initial state (if the exciton is initially at site 6):[f]

– if $T = 0\,\text{K}$: $|\Psi(0)\rangle = \left|\varphi_{g0}^{(1)}, \ldots, \varphi_{g0}^{(5)}, \varphi_{e0}^{(6)}, \varphi_{g0}^{(7)}; \varphi_{g0}^{(8)}\right\rangle$;

– if $T > 0\,\text{K}$: $|\hat{\rho}(0)\rangle$, describing the mixed state in which $\left|\varphi_{e\nu}^{(6)}\right\rangle$, $\nu = 0, 1, 2$, as well as $\left|\varphi_{g\mu}^{(i)}\right\rangle$, $i = 1, 2 \ldots, 5, 7$, $\mu = 0, 1, \ldots, V^{(i)} - 1$, are in thermal equilibrium; while the reaction center is in state $\left|\varphi_{g0}^{(8)}\right\rangle$.

[a]: Plain numbers / numbers with an apostrophe denote simulation cases in which the exciton is initially at site 6 / site 1, respectively.

[b]: Sims. #19, #22, and #24 were rerun as sims. #19×, #22×, and #24×, respectively, after substituting vibrational relaxation with pure dephasing of the same time constant (Figs. 6.2(a), 6.2(b), and 6.3).

[c]: Ref. [94].

[d]: Value chosen from the range given in Ref. [95].

[e]: Figure A.1 can be found in the Appendix.

[f]: The initial state is constructed analogously in the case when the exciton starts from site 1.

DOI:10.15774/PPKE.ITK.2018.009

which points out the significance of this incoherent process: at 300 K, it increases the transfer efficiency by 88%. (Note that if the Huang–Rhys factor is zero, then at 0 K only the lowest vibrational levels ($\nu = 0$) are populated and thus in this case vibrational relaxation has no effect on the system dynamics.)

Figure A.1 in the Appendix depicts the population dynamics for the same settings, assuming that the exciton start from site 1 instead of site 6. The results are similar to the ones presented in the previous paragraph.

After replacing the collapse operators that describe vibrational relaxation with new ones that induced the same dephasing as the original collapse operators but without population transfer, I repeated sims. #18 and #21. The population dynamics is depicted in Figs. 6.2(a) and (b). Comparing the results with the above presented ones, I found that at 0 K pure dephasing increased the efficiency of the energy transfer to 70.3% (Fig. 6.2(a)) from 70.1% obtained in the undamped case (Fig. 6.1(c)), while the system with damped vibrational modes performed at 88.2% (Fig. 6.1(b)). At 300 K, I obtained 50.0%, 36.9%, and 69.4%, respectively (see Figs. 6.2(b), 6.1(f), and 6.1(e)). Confirming my findings on the dimer, these results point out that vibrational relaxation enhances the exciton energy transfer to a much greater extent than pure dephasing. In the next section, I will demonstrate that this is true for a wide range of the time constant of the relaxation / dephasing process.

DOI:10.15774/PPKE.ITK.2018.009

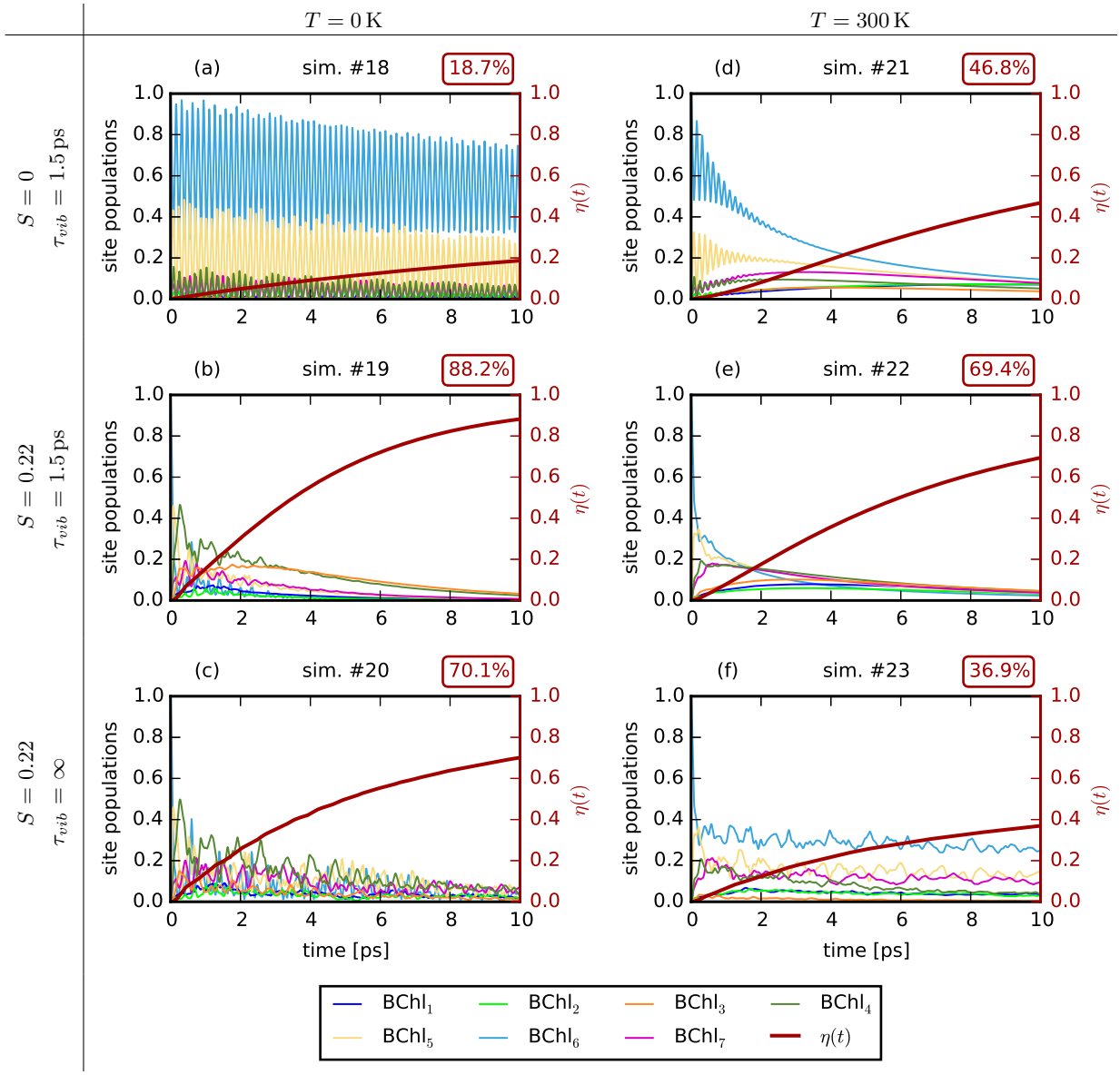

Figure 6.1: Population dynamics in the heptamer model of the FMO complex if the exciton is initially at site 6. The monotonically rising thick red curve denotes the energy transfer efficiency $\eta(t)$. The numerical value in the top right corner of each plot is $\eta\,(10\,\mathrm{ps})$, that is, the proportion of the initial exciton energy that arrived at the reaction center by the end of the simulation. The results demonstrate that the energy transfer efficiency rises when the Huang–Rhys factor S is increased (second vs. first row) and when thermalization occurs (*i.e.*, the time constant τ_{vib} of vibrational relaxation is finite) (second vs. third row). Increasing the temperature enhances the energy transfer if the Huang–Rhys factor is zero (first row), but deteriorates the efficiency, when $S = 0.22$ (second and third rows). See Tables 6.1 and 6.2 for further simulation parameters. Compare this figure with Fig. A.1 of the Appendix, which depicts the case when the exciton starts from site 1. [1]

DOI:10.15774/PPKE.ITK.2018.009

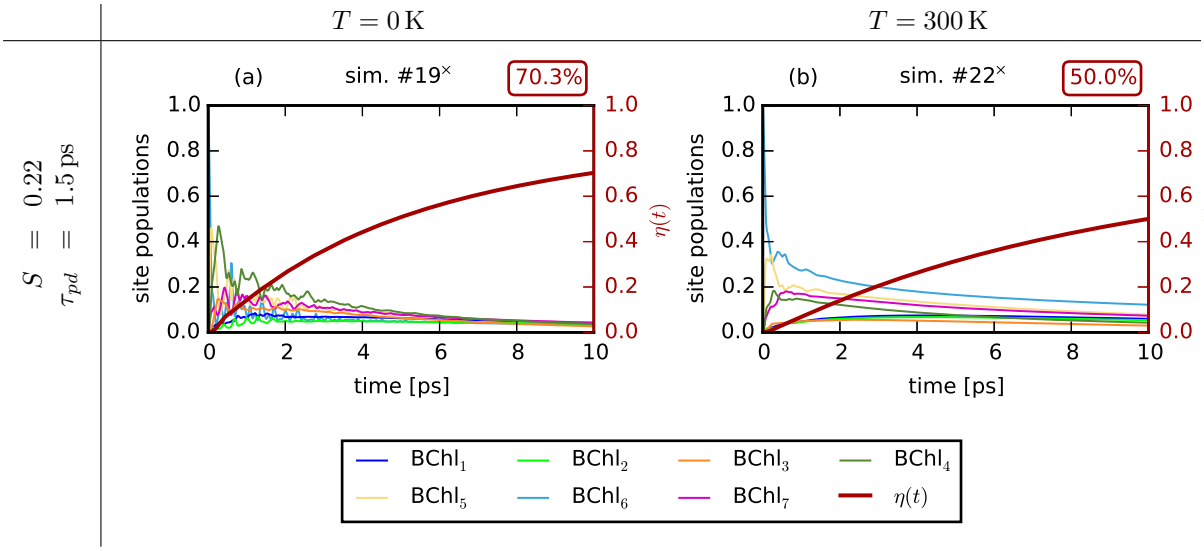

Figure 6.2: Dynamics of the exciton energy transfer in the FMO-complex-inspired heptamer exposed to pure dephasing. Initially, the exciton is at site 6. η denotes the energy transfer efficiency. The numerical value in the top right corner of each plot is $\eta\,(10\,\mathrm{ps})$, that is, the proportion of the initial exciton energy that arrives at the reaction center by the end of the simulation. The simulations presented here are the modified versions of sims. #19 and #22: the collapse operators describing vibrational relaxation were replaced by new ones that formulate pure dephasing. At 0 K, the efficiency of the energy transfer in the system exposed to pure dephasing (70.3%) (Fig. 6.2(a)) is only slightly higher than the value obtained for the undamped case (70.1%) (Fig. 6.1(c)) and is much lower than the efficiency of the system with damped vibrational modes (88.2%) (Fig. 6.1(b)). At 300 K, I obtained 50.0%, 36.9%, and 69.4%, respectively (Figs. 6.2(b), 6.1(f), and 6.1(e)). These results demonstrate that vibrational relaxation surpasses pure dephasing in the enhancement of the exciton energy transfer. [1]

6.3 Dependence on the time constant of the vibrational relaxation, on the reorganization energy, and on the temperature

Figure 6.4(a) (sims. #24 and #24') demonstrates the significance of the vibrational relaxation in the enhancement of the exciton energy transfer. Compared to the undamped case (denoted by dotted line in the figure), depending on the initial condition, the heptamer exhibits a 62% or 96% higher efficiency if the damping of the intramolecular vibrational modes is optimal (τ_{vib} is about 1 ps if the exciton starts from site 1, and 0.5 ps if it is initially at site 6). Besides, also outstripping pure dephasing (Fig. 6.3), VREEET provides a remarkable improvement for the exciton energy transfer in a wide parameter range. When the vibrational relaxation is very fast, the decline of the efficiency occurs presumably because intense decoherence impedes the propagation of the exciton.

DOI:10.15774/PPKE.ITK.2018.009

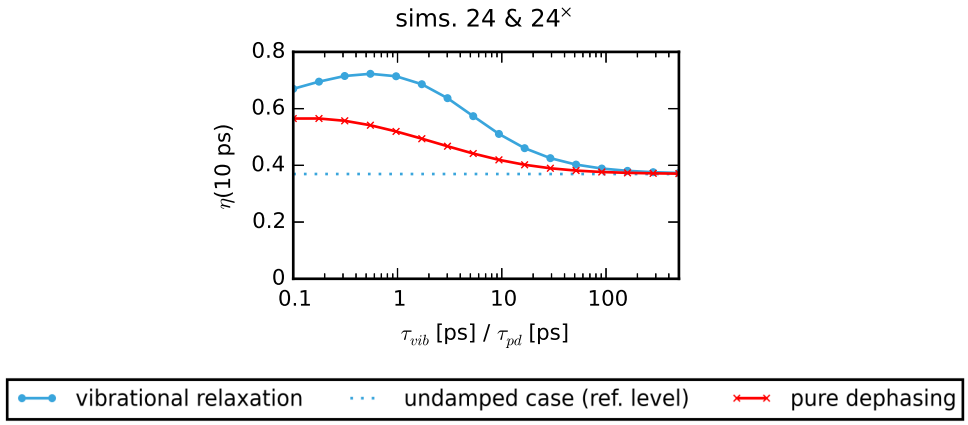

Figure 6.3: Energy transfer efficiency in the heptamer model of the FMO complex if the system is exposed to vibrational relaxation of time constant τ_{vib} or to pure dephasing of time constant τ_{pd}. (The exciton starts from site 6; $T = 300\,\mathrm{K}$.) See Tables 6.1 and 6.2 for simulation parameters.

Figure 6.4(b) (sims. #25 and #25') reveals that the coupling between different vibrational levels created by nonzero reorganization energy (being proportional to the Huang–Rhys factor) is critical for the efficient exciton transfer either if the exciton starts from site 1 or site 6. In both cases, the highest efficiency is achieved with an intermediate reorganization energy. These results are in agreement with the ones obtained by non-Markovian models, such as by the generalized Bloch–Redfield equation [74] and by the hierarchical equations of motion (HEOM) [76], which indicates the non-Markovian character of my model. Around the optimum, the curves are flat; in other words, VREEET is robust robust against the change of the reorganization energy.

The raise of the temperature accelerates dephasing and shifts the thermal equilibrium towards higher states, which can also mean a shift towards sites with higher site energies. Considering these factors, one might predict that the efficiency declines with increasing temperature if the exciton is initially at site 6, from where the energy pathway slopes all along to site 3 and 4, being connected to the reaction center. In accordance with the prediction, I obtained a monotonically declining curve for this case (sim. #26, Fig. 6.4(c)), which corresponds to former results as well [74]. However, in the other pathway, starting at site 1, site 2 forms a hill, the ascent of which is assisted by higher temperature. Thus, one might expect that the optimal efficiency is reached at some nonzero temperature determined by the opposite effects, in agreement with the results of previous studies. [74], [76] Nevertheless, my model results in a monotonically declining curve also for this initial condition (sim. #26', Fig. 6.4(c)).

DOI:10.15774/PPKE.ITK.2018.009

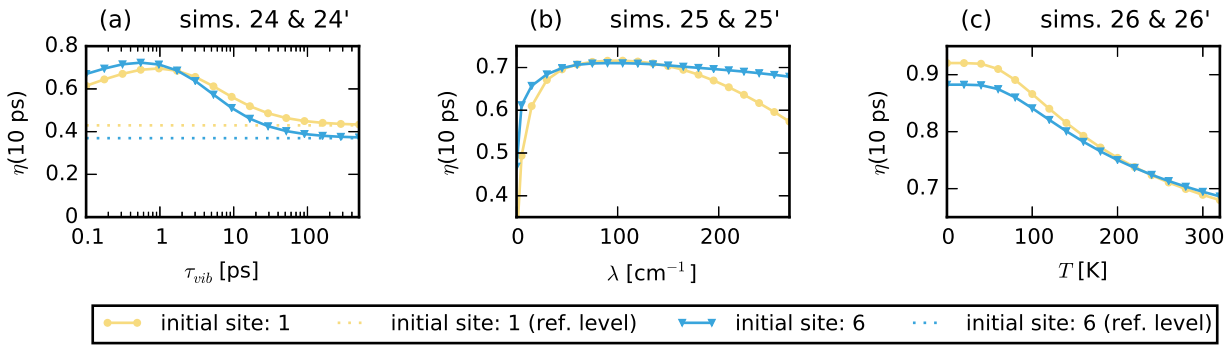

Figure 6.4: Dependence of the energy transfer efficiency in the heptamer model of the FMO complex (a) on the time constant τ_{vib} of the vibrational relaxation ($T = 300\,\mathrm{K}$), (b) on the reorganization energy $\lambda = \hbar\omega_{vib}S$ ($T = 300\,\mathrm{K}$, $\hbar\omega_{vib}$ is fixed to $180\mathrm{cm}^{-1}$), and (c) on the temperature. See Tables 6.1 and 6.2 for simulation parameters. [1]

DOI:10.15774/PPKE.ITK.2018.009

Chapter 7

Discussion

7.1 Running time of the simulations

The running time of the simulations depends primarily on the dimension D of the Hilbert space made up by the possible states of the system as well as on the number of unitary and non-unitary couplings. Running the simulations on a 2.4 GHz dual-core laptop (4 GB RAM, *Windows 7*), I experienced running times between a few tens of seconds (dimer model system, $D = 54$) and about half an hour (heptamer model of the FMO complex, $D = 309$). (In case of parameter sweep, these values obviously multiplied.)

7.2 Comparison with former results

It is known that the efficiency of the photosynthetic exciton energy transfer depends on many factors (*e.g.,* species, light conditions [96], redox potential [97]). As green sulfur bacteria live under extremely low light intensity [27], the efficiency of the photosynthetic energy transfer is vital for them. According to spectroscopic measurements, the efficiency of the energy transfer in these organisms from the antenna complex to the baseplate—under appropriate conditions—approaches 100% [97]. From the baseplate, the energy reaches the FMO complex (Fig. 2.1), which in turn transfers the exciton to the reaction center. The efficiency of the latter step was found to be about 76%—at least for those FMO complexes that were connected to the reaction center [98]. (In the cited study, two-thirds of the FMO complexes were unable to transfer the energy to the reaction center either because of some natural property of the system or because of the experimental preparation of the sample.) Although the simulation results cannot be compared one-to-one with measurement data, the model presented in this thesis qualitatively predicts the high efficiency of the photosynthetic energy transfer process, revealed by the

DOI:10.15774/PPKE.ITK.2018.009

experiments. Besides, as mentioned in Sec. 6.3, the simulation results that I obtained for the heptamer model of the FMO are qualitatively similar in many aspects to those published in Refs. [74] and [76], produced by other models.

7.3 Selection of the intramolecular vibrational modes included in the model

In reality, a pigment molecule has a large number of intramolecular vibrational modes. Including only a few of them to the system model while treating the rest as the part of the bath may seem arbitrary. Nevertheless, the computational complexity strongly limits the number of modes that can be explicitly modeled. Besides, Occam's razor suggests that one should use the simplest model to explain a phenomenon. Accordingly, I included in my model only a "single effective" [94] intramolecular vibrational mode of the spectral density of the FMO complex, which proved to be sufficient in the presented simulations to predict the high efficiency of the exciton energy transfer taking place in the FMO complex.

It is a further question, whether the demonstrated efficiency-enhancing effect of the intramolecular vibrational modes occurs also when there are plenty of them. Based on the investigations performed up to now, I cannot give a definitive answer. It is reasonable to assume that if further intramolecular vibrational modes are included in the model, they behave in the same way as did the single mode in the presented simulations, that is, the couplings between the vibronic states originating from the inclusion of a new intramolecular mode and the states of the neighboring sites create new exciton transfer pathways, whose efficiency depends on whether they are energetically resonant or not. In either case, the exciton can still use the pathways that had already existed before the new intramolecular mode was included.[1] Thus, the newly added intramolecular vibrational mode should at least not hinder the propagation of the exciton. Nevertheless, it is conceivable that the inclusion of a vibrational mode opens up a pathway that takes the exciton to an energy trap that is isolated from the reaction center. This scenario is, however, unlikely because the energy landscapes of the light-harvesting complexes usually slope to the reaction center [27], [36], [45], [75]. Ultimately, therefore, I suspect that the

[1] This statement might not hold true if the exciton occupies the excited vibrational states of the new mode with high probability due to high temperature. After, however, the ground vibrational state is depopulated by the exciton transfer, vibrational relaxation will remove the exciton from the excited vibrational states.

DOI:10.15774/PPKE.ITK.2018.009

findings of this thesis also remain valid for systems with large number of intramolecular vibrational modes.

DOI:10.15774/PPKE.ITK.2018.009

Chapter 8

Conclusions

8.1 Summary of new scientific results

Thesis 1a: I have constructed a general quantum model that describes photosynthetic exciton energy transfer taking intramolecular vibrational modes explicitly into account.

The new model describes a system built up of N pigment molecules (sites) considering two electronic states and an explicitly treated intramolecular vibrational mode at each site. In addition, the model contains an extra site, representing the reaction center. The couplings between the sites are calculated by means of the Franck–Condon overlap integrals. The time-evolution of the model system is described by a Lindblad-type master equation, in which the interaction with the memoryless environment is expressed phenomenologically through Lindblad operators.

Thesis 1b: Based on the new model, I have implemented a simulator program.

According to the particular model system, the implemented simulator program constructs the corresponding Lindblad master equation, which is then solved numerically by means of the built-in functions of *Quantum Toolbox in Python (QuTiP)* [91], [93].

DOI:10.15774/PPKE.ITK.2018.009

Thesis 2: I have surveyed in a uniform study how undamped and damped intramolecular vibrational modes influence the exciton energy transfer and especially its efficiency.

To reveal the role of intramolecular vibrational modes, I have compared various scenarios. In the well-known case of the homodimer, the exciton coherently oscillates back and forth between the two sites, being present periodically with unit probability at site 1 and then at site 2. However, the detuning of the electronic energy levels of the sites decreases the probability of the "dislocation" of the exciton. I have confirmed that this deterioration of the transfer can be compensated by the presence of intramolecular vibrational modes [43]–[52] that create resonant energy states at the two sites, provided that the Huang–Rhys factors are sufficiently large to couple these levels. In addition, I have demonstrated that the damping of these vibrational modes can considerably enhance the energy transfer further. The latter result is in accordance with Refs. [45], [47], [54], but it contradicts the findings of Refs. [50], [52].

The reason for the improvement of the efficiency is that vibrational relaxation can take the exciton to a state that is energetically detuned from all the states of the site from where the exciton arrived, which impedes the propagation of the exciton back to the previous site (Fig. 8.1). Vibrational relaxation can thus unidirect the energy transfer and, moreover, trap the exciton at sites connected to the reaction center, resulting in a higher efficiency. I refer to this kind of transport process as *vibrational-relaxation-enhanced exciton energy transfer* (*VREEET*).

Thesis 2a: I have demonstrated that the relative enhancement of the energy transfer caused by vibrational relaxation is multiple times larger than the relative enhancement caused by pure dephasing.

By omitting the population transferring effect of vibrational relaxation (and excitation), I introduced pure dephasing in the model. I demonstrated that this process can also increase the efficiency of the energy transfer (as it had been formerly described in Refs. [70], [99]); however, the enhancement caused by pure dephasing is notably surpassed by the one caused by vibrational relaxation (both in the dimer model at 0 K and in the heptamer model of the FMO complex at 0 K and at 300 K).

DOI:10.15774/PPKE.ITK.2018.009

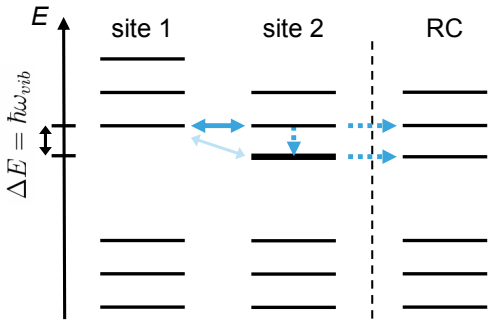

Figure 8.1: The path of vibrational-relaxation-enhanced exciton energy transfer (VREEET) from site 1 to the reaction center (RC) in the dimer model. There is dipole–dipole coupling between energetically resonant states $\left|\varphi_{e0}^{(1)}\right\rangle$ and $\left|\varphi_{e1}^{(2)}\right\rangle$; thus, the exciton can oscillate among them. Vibrational relaxation, however, gets site 2 from $\left|\varphi_{e1}^{(2)}\right\rangle$ to $\left|\varphi_{e0}^{(2)}\right\rangle$ (the latter state is denoted by the thick line), from where the propagation of the exciton back to site 1 (along the thin double arrow) is impeded because of the energy mismatch. In effect, the exciton is trapped at site 2 in state $\left|\varphi_{e0}^{(2)}\right\rangle$, from where the reaction center absorbs its energy. [1]

Thesis 2b: I have demonstrated that vibrational relaxation can considerably and robustly enhance the exciton energy transfer in wide ranges of several parameters.

I have examined the dependence of VREEET on several simulation parameters. Running simulations on dimer model systems at 300 K, I have shown that VREEET is robust both against the parallel change of electronic energy levels of the sites and against the alteration of the strength of the inter-pigment coupling. I demonstrated that faster vibrational relaxation produces larger enhancement of the energy transfer and also that the slower the sink effect of the reaction center, the higher the relative increment of the transfer efficiency. In addition, I have revealed that VREEET exhibits the highest efficiency if the energy detuning between the electronic levels of the neighboring sites is intermediate, the vibrational mode is quasi-resonant with this energy detuning, and the Huang–Rhys factors of the sites are large enough to couple the corresponding vibronic states. I found that the energy transfer efficiency declines with increasing temperature, but the enhancement caused by vibrational relaxation remains considerable at higher temperatures as well. I demonstrated that the increase of the frequency of the vibrational modes (together with the detuning of the electronic levels of the coupled sites so that they remain resonant) reduces the temperature-dependence of the efficiency, since it lowers the occupation probability of higher vibrational levels, through which the backward propagation of the exciton can take place.

DOI:10.15774/PPKE.ITK.2018.009

The results that I obtained for the heptamer model of the FMO complex at 300 K show trends which are similar to those obtained for the dimers, and they demonstrate that vibrational relaxation can enhance the exciton energy transfer in more complex systems as well, even at room temperature, also if the vibronic levels are not strictly resonant. This corroborates that the directionality of the exciton transfer is provided by thermalization [27], [36], [45], [75]. I got values up to 96% for the relative gain caused by vibrational relaxation. Fixing the frequency of the intramolecular vibrational mode and sweeping the Huang–Rhys factor, I found that the energy transfer efficiency of the FMO complex at 300 K depends strongly on the reorganization energy and reaches its maximum at some intermediate value of the reorganization energy, which trend is characteristic of the results provided by non-Markovian models [74], [76]. Finally, I found that the energy transfer efficiency declines monotonically with increasing temperature in the case of both energy pathways of the FMO complex. This corresponds to data published previously on the energy pathway starting at site 6 [74], but differs from former results on the energy pathway starting at site 1 [74], [76].

VREEET occurred in wide ranges of the investigated parameters both in the simple, "constrained" dimer model systems and in the more complicated, "disordered" heptamer model of the FMO complex.. This—presuming that the presented mechanism also works in real systems, built up of molecules with numerous vibrational modes—suggests that VREEET might be prevalent in light-harvesting complexes, and it can contribute to the high efficiency of the exciton energy transfer occurring during the initial stage of photosynthesis.

8.2 Applications

The potential inherent in newly emerging quantum technologies has its root primarily in quantum coherence, that is, in the possibility of the coexistence of various states. Therefore, the comprehension of coherence and environment-induced decoherence is of key importance. The operation of quantum computers requires long-lasting quantum coherence; in other words, the noise of the environment is to be eliminated in their case. On the other hand, the interaction between a quantum system and its environment can also be beneficial, and nature seems to exploit it, for instance, in photosynthesis. The underlying mechanisms—among them those discussed in this thesis—might also be applied in artificial light-harvesting systems [100] and in sensors during the unfolding second quantum revolution.

DOI:10.15774/PPKE.ITK.2018.009

Appendix

A.1 Notations of quantum states in the simulation model

Table A.1: Notations of quantum states in the simulation model. [1]

Notation	Meaning
$\left\|\phi_{\varepsilon}^{(i)}\right\rangle$	ground ($\varepsilon = g$) or excited ($\varepsilon = e$) electronic basis state of the i-th site
$\left\|\chi_{\varepsilon\nu}^{(i)}\right\rangle$	ν-th ($\nu = 0, 1, \ldots, V-1$) vibrational basis state of the i-th site, being in the ground ($\varepsilon = g$) or excited ($\varepsilon = e$) electronic state
$\left\|\varphi_{\varepsilon\nu}^{(i)}\right\rangle =$ $= \left\|\phi_{\varepsilon}^{(i)}\right\rangle \left\|\chi_{\varepsilon\nu}^{(i)}\right\rangle$	vibronic basis state of the i-th site, being in electronic state ε and vibrational state ν
$\left\|\varphi^{(i)}\right\rangle$	arbitrary state of the i-th site
$\|\Psi_m\rangle$	m-th basis state of the system
$\|\Psi\rangle$	arbitrary state of the system

A.2 Effect of the collapse operators on the density matrix

Let us consider the Lindblad operator $\hat{A}_{nm} = |\Psi_n\rangle \langle\Psi_m|$, $m \neq n$, represented by a matrix whose elements are all zero, except the one in the m-th column of the n-th row, which is 1. Introducing a rate constant γ_{nm}, we can define a collapse operator as $\hat{C}_{nm} = \sqrt{\gamma_{nm}}\hat{A}_{nm}$. The effect of this operator on the dynamics of the system is formulated in the Lindblad equation (3.5) (in the main text) by the term

DOI:10.15774/PPKE.ITK.2018.009

$$\gamma_{nm}\left(\hat{A}_{nm}\hat{\rho}(t)\hat{A}_{nm}^{\dagger}-\tfrac{1}{2}\hat{A}_{nm}^{\dagger}\hat{A}_{nm}\hat{\rho}(t)-\tfrac{1}{2}\hat{\rho}(t)\hat{A}_{nm}^{\dagger}\hat{A}_{nm}\right)=\hat{C}_{nm}\hat{\rho}(t)\hat{C}_{nm}^{\dagger}-\tfrac{1}{2}\hat{C}_{nm}^{\dagger}\hat{C}_{nm}\hat{\rho}(t)-\tfrac{1}{2}\hat{\rho}(t)\hat{C}_{nm}^{\dagger}\hat{C}_{nm}=$$

$$=\gamma_{nm}\begin{bmatrix}
0 & \dots & 0 & 0 & 0 & \dots & 0 & -\frac{\hat{\rho}_{1,m}}{2} & 0 & \dots & 0\\
\vdots & \ddots & \vdots & \vdots & \vdots & \ddots & \vdots & \vdots & \vdots & \ddots & \vdots\\
0 & \dots & 0 & 0 & 0 & \dots & 0 & -\frac{\hat{\rho}_{n-1,m}}{2} & 0 & \dots & 0\\
0 & \dots & 0 & \hat{\rho}_{m,m} & 0 & \dots & 0 & -\frac{\hat{\rho}_{n,m}}{2} & 0 & \dots & 0\\
0 & \dots & 0 & 0 & 0 & \dots & 0 & -\frac{\hat{\rho}_{n+1,m}}{2} & 0 & \dots & 0\\
\vdots & \ddots & \vdots & \vdots & \vdots & \ddots & \vdots & \vdots & \vdots & \ddots & \vdots\\
0 & \dots & 0 & 0 & 0 & \dots & 0 & -\frac{\hat{\rho}_{m-1,m}}{2} & 0 & \dots & 0\\
-\frac{\hat{\rho}_{m,1}}{2} & \dots & -\frac{\hat{\rho}_{m,n-1}}{2} & -\frac{\hat{\rho}_{m,n}}{2} & -\frac{\hat{\rho}_{m,n+1}}{2} & \dots & -\frac{\hat{\rho}_{m,m-1}}{2} & -\hat{\rho}_{m,m} & -\frac{\hat{\rho}_{m,m+1}}{2} & \dots & -\frac{\hat{\rho}_{m,D}}{2}\\
0 & \dots & 0 & 0 & 0 & \dots & 0 & -\frac{\hat{\rho}_{m+1,m}}{2} & 0 & \dots & 0\\
\vdots & \ddots & \vdots & \vdots & \vdots & \ddots & \vdots & \vdots & \vdots & \ddots & \vdots\\
0 & \dots & 0 & 0 & 0 & \dots & 0 & -\frac{\hat{\rho}_{D,m}}{2} & 0 & \dots & 0
\end{bmatrix}, \tag{A.1}$$

where D denotes the dimension of the Hilbert space describing the state of the system. Since the left side of the Lindblad equation is the time derivative of the density matrix, $\hat{C}_{nm}$ expresses an exponential decay with time constant $\tau_{nm}=\gamma_{nm}^{-1}$ from population $\hat{\rho}_{m,m}$ (corresponding to basis state $|\Psi_m\rangle$) to population $\hat{\rho}_{n,n}$ (corresponding to basis state$|\Psi_n\rangle$), on the one hand; and the decay of all the off-diagonal elements (called coherences) in the m-th row and in the m-th column of the density matrix with time constant $(\gamma_{nm}/2)^{-1}=2\tau_{nm}$, on the other hand.

On the contrary, with the Lindblad operator $\hat{A}_{mm}=|\Psi_m\rangle\langle\Psi_m|$ and rate constant γ_{nm}, we can define the collapse operator $\hat{C}_{nm}^{\times}=\sqrt{\gamma_{nm}}\hat{A}_{mm}=\sqrt{\gamma_{nm}}\,|\Psi_m\rangle\langle\Psi_m|=\hat{C}_{mm}$, which affects the system dynamics through the term

DOI:10.15774/PPKE.ITK.2018.009

$$\gamma_{nm}\left(\hat{A}_{mm}\hat{\rho}(t)\hat{A}_{mm}^{\dagger}-\tfrac{1}{2}\hat{A}_{mm}^{\dagger}\hat{A}_{mm}\hat{\rho}(t)-\tfrac{1}{2}\hat{\rho}(t)\hat{A}_{mm}^{\dagger}\hat{A}_{mm}\right)=\hat{C}_{nm}^{\times}\hat{\rho}(t)\hat{C}_{nm}^{\times\dagger}-\tfrac{1}{2}\hat{C}_{nm}^{\times\dagger}\hat{C}_{nm}^{\times}\hat{\rho}(t)-\tfrac{1}{2}\hat{\rho}(t)\hat{C}_{nm}^{\times\dagger}\hat{C}_{nm}^{\times}=$$

$$=\gamma_{nm}\begin{bmatrix}
0 & \dots & 0 & 0 & 0 & \dots & 0 & -\frac{\hat{\rho}_{1,m}}{2} & 0 & \dots & 0\\
\vdots & \ddots & \vdots & \vdots & \vdots & \ddots & \vdots & \vdots & \vdots & \ddots & \vdots\\
0 & \dots & 0 & 0 & 0 & \dots & 0 & -\frac{\hat{\rho}_{n-1,m}}{2} & 0 & \dots & 0\\
0 & \dots & 0 & 0 & 0 & \dots & 0 & -\frac{\hat{\rho}_{n,m}}{2} & 0 & \dots & 0\\
0 & \dots & 0 & 0 & 0 & \dots & 0 & -\frac{\hat{\rho}_{n+1,m}}{2} & 0 & \dots & 0\\
\vdots & \ddots & \vdots & \vdots & \vdots & \ddots & \vdots & \vdots & \vdots & \ddots & \vdots\\
0 & \dots & 0 & 0 & 0 & \dots & 0 & -\frac{\hat{\rho}_{m-1,m}}{2} & 0 & \dots & 0\\
-\frac{\hat{\rho}_{m,1}}{2} & \dots & -\frac{\hat{\rho}_{m,n-1}}{2} & -\frac{\hat{\rho}_{m,n}}{2} & -\frac{\hat{\rho}_{m,n+1}}{2} & \dots & -\frac{\hat{\rho}_{m,m-1}}{2} & 0 & -\frac{\hat{\rho}_{m,m+1}}{2} & \dots & -\frac{\hat{\rho}_{m,D}}{2}\\
0 & \dots & 0 & 0 & 0 & \dots & 0 & -\frac{\hat{\rho}_{m+1,m}}{2} & 0 & \dots & 0\\
\vdots & \ddots & \vdots & \vdots & \vdots & \ddots & \vdots & \vdots & \vdots & \ddots & \vdots\\
0 & \dots & 0 & 0 & 0 & \dots & 0 & -\frac{\hat{\rho}_{D,m}}{2} & 0 & \dots & 0
\end{bmatrix}. \tag{A.2}$$

Thus, $\hat{C}_{nm}^{\times}$ describes pure dephasing. It damps the same off-diagonal elements of the density matrix as does $\hat{C}_{nm}$, but it does not induce population transfer. I retained n in the subscript of the notation $\hat{C}_{nm}^{\times}$ to express that there is a pure dephasing operator $\hat{C}_{nm}^{\times}$ to each "population transferring" operator $\hat{C}_{nm}$ $(m \neq n)$.

A.3 Franck–Condon overlap integrals as a function of Huang–Rhys factor

Table A.2: Franck–Condon overlap integrals $\left\langle \chi_{g\nu'}^{(i)} \middle| \chi_{e\nu}^{(i)} \right\rangle$ of the three lowest vibrational states ν and ν' as a function of the Huang–Rhys factor S. [1]

	$\nu=0$	$\nu=1$	$\nu=2$
$\nu'=0$	$\exp(-S/2)$	$-\sqrt{S}\exp(-S/2)$	$\frac{S}{\sqrt{2}}\exp(-S/2)$
$\nu'=1$	$\sqrt{S}\exp(-S/2)$	$-(S-1)\exp(-S/2)$	$(S-2)\sqrt{\frac{S}{2}}\exp(-S/2)$
$\nu'=2$	$\frac{S}{\sqrt{2}}\exp(-S/2)$	$-(S-2)\sqrt{\frac{S}{2}}\exp(-S/2)$	$\frac{S^2-4S+2}{2}\exp(-S/2)$

DOI:10.15774/PPKE.ITK.2018.009

A.4 Supplementary simulation results

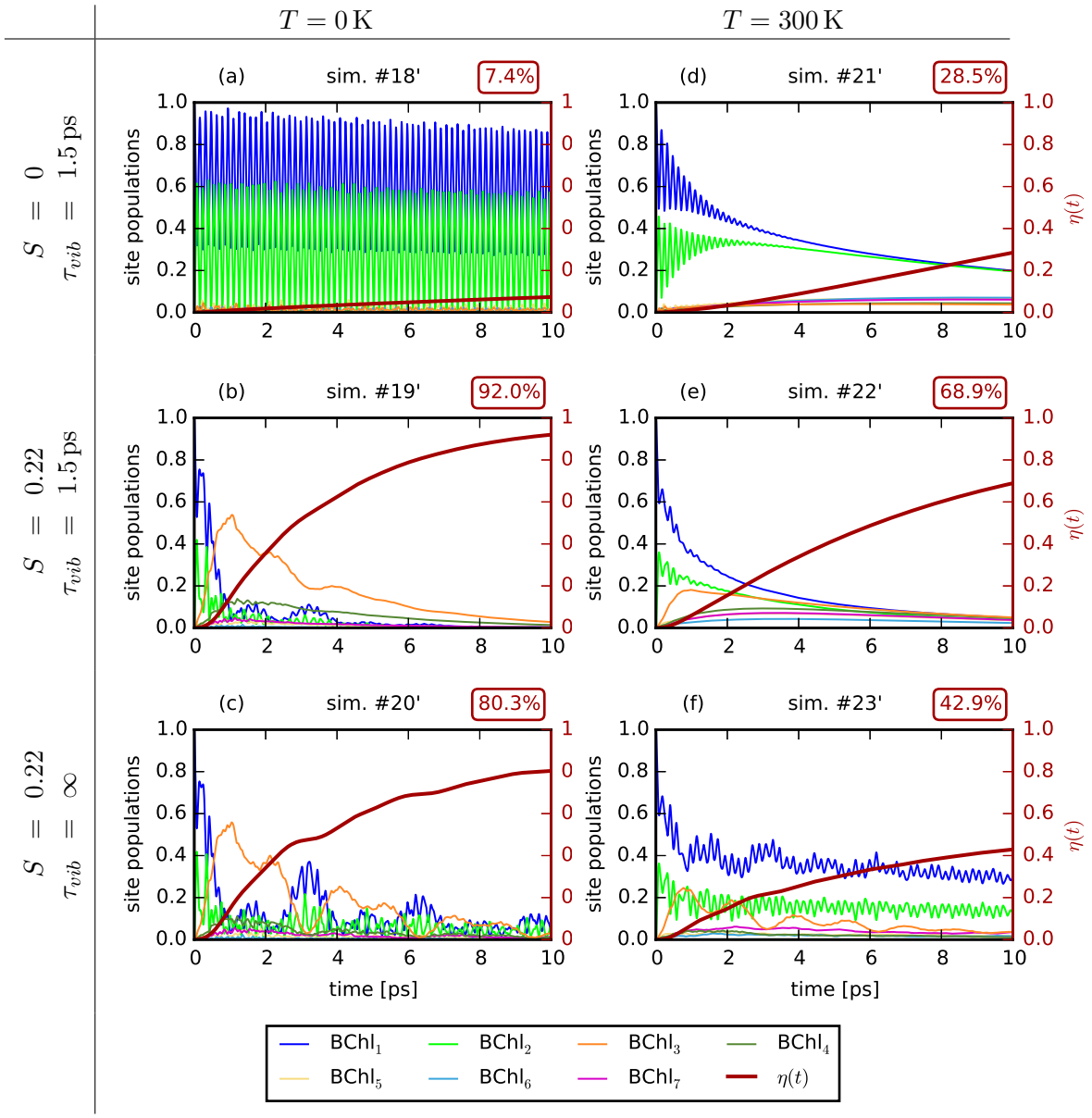

Figure A.1: Population dynamics in the heptamer model of the FMO complex if the exciton is initially at site 1. The monotonically rising thick red curve denotes the energy transfer efficiency $\eta(t)$. The numerical value in the top right corner of each plot is $\eta\,(10\,\mathrm{ps})$, that is, the proportion of the initial exciton energy that arrived at the reaction center by the end of the simulation. The results demonstrate that the energy transfer efficiency rises when the Huang–Rhys factor S is increased (second vs. first row) and when thermalization occurs (*i.e.*, the time constant τ_{vib} of vibrational relaxation is finite) (second vs. third row). Increasing the temperature enhances the energy transfer if the Huang–Rhys factor is zero (first row), but deteriorates the efficiency, when $S = 0.22$ (second and third rows). See Tables 6.1 and 6.2 for further simulation parameters. Compare this figure with Fig. 6.1 in the main text, which depicts the case when the exciton starts from site 6. [1]

DOI:10.15774/PPKE.ITK.2018.009

Glossary

exciton

A quasiparticle that represents the excited state of a molecule.

closed quantum system

A quantum system that does not interact with its environment.

open quantum system

A quantum system that interacts with its environment.

pure state

A quantum state that can be represented by a single wave function.

mixed state

A quantum state that cannot be represented by a single wave function,

Hamiltonian

The total energy operator of a quantum system, which governs the time-evolution of the system.

master equation

An equation that describes the time-evolution of the state of a system.

Schrödinger equation (time-dependent)

A differential equation that describes the time-evolution of closed quantum systems.

Liouville–von Neumann equation

A differential equation that describes the time-evolution of closed quantum systems in the density matrix formalism. It is more general than the Schrödinger equation in the sense that it can also be applied on systems being in a mixed state.

Lindblad equation

An approximate differential equation that describes the time-evolution of open

DOI:10.15774/PPKE.ITK.2018.009

quantum systems. Its derivation is built on the Born, Markov, and rotating wave approximations.

Born approximation

It assumes that the changes of the bath that are caused by the interaction with the system are negligible and thus the density matrix of the system–bath composite can be factorized as the product of the density matrix of the system and that of the bath, where the latter is considered to be constant.

Markov approximation

It assumes that the changes of the bath that are caused by the interaction with the system decay fast and thus the evolution of the system does not depend on the past of system, but solely on its present state.

secular *or* rotating wave approximation

It neglects the off-resonant, fast oscillating terms of the state dynamics assuming that they do not influence the dynamics substantially on the time scale of interest.

quantum coherence

A quantum state is coherent, if it is a linear superposition of two or more basis states. (As it follows from this definition, coherence is base-dependent.) Such a superposition and thus coherence are often related to transitions between the involved basis states, and these transitions frequently lead to oscillatory state dynamics.

decoherence

The decay of the coherent state due to interaction with the environment.

relaxation

Also known as T_1 or longitudinal damping. During this process, the system gets to a lower energy state due to the interaction with the environment.

pure dephasing

Also known as T_2 or transverse damping. During this environment-induced and energy-conserving process, the coherence of the quantum state decays without population transfer.

collapse operator

An operator that describes the system–bath interaction through the non-unitary part of the Lindblad master equation. It is the product of the square of a rate constant and a Lindblad operator.

DOI:10.15774/PPKE.ITK.2018.009

FMO complex

Fenna–Matthews–Olson complex, also known as FMO protein and BChl *a*-protein. A molecule complex in green sulfur bacteria that transfers the exciton energy from the baseplate of the chlorosome to the reaction center.

intramolecular vibrational mode

A particular oscillation of the atomic nuclei within a molecule.

vibronic state

The composite of a vibrational and an electronic state.

Huang–Rhys factor

A parameter that expresses the coupling strength between the electronic state and the intramolecular vibrational mode of a molecule. It is related to the spatial shift between the potential surfaces of the vibrational mode in the ground and in the excited electronic states.

reorganization energy

The electronic excitation of a molecule is often followed by vibrational relaxation so that the molecule will reach the equilibrium point of the potential surface of the vibrational mode belonging to the excited electronic state. The reorganization energy is the energy that the molecule loses during this relaxation. It is proportional to the Huang–Rhys factor.

Franck–Condon overlap integral

The overlap integral of a vibrational state that belongs to ground electronic state and of another one that belongs to the excited electronic state of the same molecule.

DOI:10.15774/PPKE.ITK.2018.009

The Author's Publications

Journal articles

[1] **I. B. Juhász** and Á. I. Csurgay, "Impact of undamped and damped intramolecular vibrations on the efficiency of photosynthetic exciton energy transfer", *AIP Advances*, accepted for publication.

[2] **I. B. Juhász** and Á. I. Csurgay, "Fluorescence in two-photon-excited diffusible samples exposed to photobleaching: A simulation-based study", *Journal of Biomedical Optics*, vol. 20, no. 1, p. 015 001, 2015. DOI: 10.1117/1.JBO.20.1.015001.

[3] Á. I. Csurgay, **I. B. Juhász**, and P. P. Civalleri, "Toward engineering design of quantum circuits", *International Journal of Circuit Theory and Applications*, vol. 45, no. 7, pp. 882–896, 2017. DOI: 10.1002/cta.2358.

Further publications

[4] **I. B. Juhász** and Á. I. Csurgay, "Simulation-based investigation of the three-dimensional distribution of fluorescence and photobleaching in multi-photon excited samples", in *Proceedings of SPIE*, F. Wyrowski, J. T. Sheridan, J. Tervo, and Y. Meuret, Eds., vol. 9131, Brussels, 2014, 91310S. DOI: 10.1117/12.2052243.

[5] **I. B. Juhász**, Á. Fekete, and Á. I. Csurgay, "Engineering QED – Quantum Circuits", in *Proceedings of the Workshop on Information Technology and Bionics: Symposium in Memory of Tamás Roska*, Budapest: Pázmány University ePress, 2015.

[6] **I. B. Juhász**, "Simulation of energy transfer between coupled two-state atoms", in *PhD Proceedings Annual Issues of the Doctoral School*, G. Prószéky and P. Szolgay, Eds., Budapest: Pázmány University ePress, 2015, pp. 145–148.

DOI:10.15774/PPKE.ITK.2018.009

[7] **I. B. Juhász**, "Simulation-based study of the spatial profile of fluorescence and photobleaching in two-photon-excited samples", in *PhD Proceedings Annual Issues of the Doctoral School - 2014*, T. Roska, G. Prószéky, and P. Szolgay, Eds., Budapest: Pázmány University ePress, 2014, pp. 121–125.

[8] **I. B. Juhász**, "Simulation-based Investigation of Temporal and Spatial Characteristics of Photodynamics in Two-Photon Microscope", in *Proceedings of the Interdisciplinary Doctoral School in the 2012-2013 Academic Year*, T. Roska, G. Prószéky, and P. Szolgay, Eds., vol. 8, Budapest: Pázmány University ePress, 2013, pp. 41–45.

[9] **I. B. Juhász**, Á. Fekete, and Á. I. Csurgay, "Two-photon and Stimulated Emission Microscopy: Quantum Electrodynamics in Simulations", conference talk at *Bionics: At the crossroads of Biotechnology and Information Technologies*, Budapest, 2013.

[10] **I. B. Juhász**, "Simulation-based investigation of the effect of two-photon microscope operating parameters on the image quality and photobleaching", poster presentation at *From Medicine to Bionics*, Budapest, 2013.

DOI:10.15774/PPKE.ITK.2018.009

References

[11] J. C. Brookes, "Quantum effects in biology: Golden rule in enzymes, olfaction, photosynthesis and magnetodetection", *Proceedings of the Royal Society A: Mathematical, Physical and Engineering Science*, vol. 473, no. 2201, p. 20 160 822, 2017. DOI: 10.1098/rspa.2016.0822.

[12] E. Schrödinger, *What is life?: With mind and matter and autobiographical sketches*. Cambridge University Press, 1992.

[13] J. D. Watson and F. H. C. Crick, "A Structure for Deoxyribose Nucleic Acid", *Nature*, vol. 171, no. 4356, pp. 737–738, 1953.

[14] G. R. Fleming, G. D. Scholes, and Y.-C. Cheng, "Quantum effects in biology", *Procedia Chemistry*, vol. 3, no. 1, pp. 38–57, 2011. DOI: 10.1016/j.proche.2011.08.011.

[15] P. Ball, "The dawn of quantum biology", *Nature*, vol. 474, pp. 272–274, 2011. DOI: 10.1038/474272a.

[16] N. Lambert, Y.-N. Chen, Y.-C. Cheng, C.-M. Li, G.-Y. Chen, and F. Nori, "Quantum biology", *Nature Physics*, vol. 9, no. 1, pp. 10–18, 2012. DOI: 10.1038/nphys2474.

[17] P.-O. Löwdin, "Proton tunneling in DNA and its biological implications", *Reviews of Modern Physics*, vol. 35, pp. 724–732, 1963.

[18] Y. Cha, C. Murray, and J. Klinman, "Hydrogen tunneling in enzyme reactions", *Science*, vol. 243, no. 4896, pp. 1325–1330, 1989. DOI: 10.1126/science.2646716.

[19] J. P. Klinman and A. Kohen, "Hydrogen Tunneling Links Protein Dynamics to Enzyme Catalysis", *Annual Review of Biochemistry*, vol. 82, no. 1, pp. 471–496, 2013. DOI: 10.1146/annurev-biochem-051710-133623.

DOI:10.15774/PPKE.ITK.2018.009

[20] L. Turin, "A Spectroscopic Mechanism for Primary Olfactory Reception", *Chemical Senses*, vol. 21, no. 6, pp. 773–791, 1996. DOI: 10.1093/chemse/21.6.773.

[21] K. Schulten, C. E. Swenberg, and A. Weller, "A biomagnetic sensory mechanism based on magnetic field modulated coherent electron spin motion", *Zeitschrift für Physikalische Chemie*, vol. 111, pp. 1–5, 1978.

[22] T. Ritz, S. Adem, and K. Schulten, "A Model for Photoreceptor-Based Magnetoreception in Birds", *Biophysical Journal*, vol. 78, no. 2, pp. 707–718, 2000. DOI: 10.1016/S0006-3495(00)76629-X.

[23] K. Maeda, K. B. Henbest, F. Cintolesi, I. Kuprov, C. T. Rodgers, P. A. Liddell, D. Gust, C. R. Timmel, and P. J. Hore, "Chemical compass model of avian magnetoreception", *Nature*, vol. 453, no. 7193, pp. 387–390, 2008. DOI: 10.1038/nature06834.

[24] J. Cai, G. G. Guerreschi, and H. J. Briegel, "Quantum Control and Entanglement in a Chemical Compass", *Physical Review Letters*, vol. 104, no. 22, 2010. DOI: 10.1103/PhysRevLett.104.220502.

[25] E. M. Gauger, E. Rieper, J. J. L. Morton, S. C. Benjamin, and V. Vedral, "Sustained Quantum Coherence and Entanglement in the Avian Compass", *Physical Review Letters*, vol. 106, no. 4, 2011. DOI: 10.1103/PhysRevLett.106.040503.

[26] J. P. Dowling and G. J. Milburn, "Quantum technology: The second quantum revolution", *Philosophical Transactions of the Royal Society A: Mathematical, Physical and Engineering Sciences*, vol. 361, no. 1809, pp. 1655–1674, 2003. DOI: 10.1098/rsta.2003.1227.

[27] R. E. Blankenship, *Molecular mechanisms of photosynthesis*. Oxford: Blackwell Science, 2002.

[28] A. Chenu and G. D. Scholes, "Coherence in Energy Transfer and Photosynthesis", *Annual Review of Physical Chemistry*, vol. 66, no. 1, pp. 69–96, 2015. DOI: 10.1146/annurev-physchem-040214-121713.

[29] T. Förster, "Zwischenmolekulare Energiewanderung und Fluoreszenz", *Annalen der Physik*, vol. 437, no. 1-2, pp. 55–75, 1948. DOI: 10.1002/andp.19484370105.

[30] J. Wu, F. Liu, J. Ma, R. J. Silbey, and J. Cao, "Efficient energy transfer in light-harvesting systems: Quantum-classical comparison, flux network, and robustness analysis", *The Journal of Chemical Physics*, vol. 137, no. 17, p. 174 111, 2012. DOI: 10.1063/1.4762839.

DOI:10.15774/PPKE.ITK.2018.009

[31] A. Ishizaki and G. R. Fleming, "Quantum Coherence in Photosynthetic Light Harvesting", *Annual Review of Condensed Matter Physics*, vol. 3, no. 1, pp. 333–361, 2012. DOI: 10.1146/annurev-conmatphys-020911-125126.

[32] G. S. Engel, T. R. Calhoun, E. L. Read, T.-K. Ahn, T. Mančal, Y.-C. Cheng, R. E. Blankenship, and G. R. Fleming, "Evidence for wavelike energy transfer through quantum coherence in photosynthetic systems", *Nature*, vol. 446, no. 7137, pp. 782–786, 2007. DOI: 10.1038/nature05678.

[33] E. Collini, C. Y. Wong, K. E. Wilk, P. M. G. Curmi, P. Brumer, and G. D. Scholes, "Coherently wired light-harvesting in photosynthetic marine algae at ambient temperature", *Nature*, vol. 463, no. 7281, pp. 644–647, 2010. DOI: 10.1038/nature08811.

[34] G. Panitchayangkoon, D. Hayes, K. A. Fransted, J. R. Caram, E. Harel, J. Wen, R. E. Blankenship, and G. S. Engel, "Long-lived quantum coherence in photosynthetic complexes at physiological temperature", *Proceedings of the National Academy of Sciences*, vol. 107, no. 29, pp. 12 766–12 770, 2010. DOI: 10.1073/pnas.1005484107.

[35] G. Panitchayangkoon, D. V. Voronine, D. Abramavicius, J. R. Caram, N. H. C. Lewis, S. Mukamel, and G. S. Engel, "Direct evidence of quantum transport in photosynthetic light-harvesting complexes", *Proceedings of the National Academy of Sciences*, vol. 108, no. 52, pp. 20 908–20 912, 2011.

[36] A. Ishizaki and G. R. Fleming, "Theoretical examination of quantum coherence in a photosynthetic system at physiological temperature", *Proceedings of the National Academy of Sciences*, vol. 106, no. 41, pp. 17 255–17 260, 2009.

[37] H.-G. Duan, V. I. Prokhorenko, R. J. Cogdell, K. Ashraf, A. L. Stevens, M. Thorwart, and R. J. D. Miller, "Nature does not rely on long-lived electronic quantum coherence for photosynthetic energy transfer", *Proceedings of the National Academy of Sciences*, vol. 114, no. 32, pp. 8493–8498, 2017. DOI: 10.1073/pnas.1702261114.

[38] H.-P. Breuer and F. Petruccione, *The theory of open quantum systems*. New York: Oxford University Press, 2002.

[39] P. P. Civalleri, *Finite-dimensional open quantum systems*, Lecture notes, Politecnico di Torino, 2011.

DOI:10.15774/PPKE.ITK.2018.009

[40] N. Christensson, H. F. Kauffmann, T. Pullerits, and T. Mančal, "Origin of Long-Lived Coherences in Light-Harvesting Complexes", *The Journal of Physical Chemistry B*, vol. 116, no. 25, pp. 7449–7454, 2012. DOI: 10.1021/jp304649c.

[41] M. B. Plenio, J. Almeida, and S. F. Huelga, "Origin of long-lived oscillations in 2d-spectra of a quantum vibronic model: Electronic versus vibrational coherence", *The Journal of Chemical Physics*, vol. 139, no. 23, p. 235 102, 2013. DOI: 10.1063/1.4846275.

[42] J. Lim, D. Paleček, F. Caycedo-Soler, C. N. Lincoln, J. Prior, H. von Berlepsch, S. F. Huelga, M. B. Plenio, D. Zigmantas, and J. Hauer, "Vibronic origin of long-lived coherence in an artificial molecular light harvester", *Nature Communications*, vol. 6, p. 7755, 2015. DOI: 10.1038/ncomms8755.

[43] A. Kolli, E. J. O'Reilly, G. D. Scholes, and A. Olaya-Castro, "The fundamental role of quantized vibrations in coherent light harvesting by cryptophyte algae", *The Journal of Chemical Physics*, vol. 137, no. 17, p. 174 109, 2012. DOI: 10.1063/1.4764100.

[44] Y. Sato and B. Doolittle, "Influence of intra-pigment vibrations on dynamics of photosynthetic exciton", *The Journal of Chemical Physics*, vol. 141, no. 18, p. 185 102, 2014. DOI: 10.1063/1.4901056.

[45] E. K. Irish, R. Gómez-Bombarelli, and B. W. Lovett, "Vibration-assisted resonance in photosynthetic excitation-energy transfer", *Physical Review A*, vol. 90, no. 1, p. 012 510, 2014. DOI: 10.1103/PhysRevA.90.012510.

[46] N. Killoran, S. F. Huelga, and M. B. Plenio, "Enhancing light-harvesting power with coherent vibrational interactions: A quantum heat engine picture", *The Journal of Chemical Physics*, vol. 143, no. 15, p. 155 102, 2015. DOI: 10.1063/1.4932307.

[47] Z. Zhang and J. Wang, "Assistance of Molecular Vibrations on Coherent Energy Transfer in Photosynthesis from the View of a Quantum Heat Engine", *The Journal of Physical Chemistry B*, vol. 119, no. 13, pp. 4662–4667, 2015. DOI: 10.1021/acs.jpcb.5b01569.

[48] P. Malý, O. J. G. Somsen, V. I. Novoderezhkin, T. Mančal, and R. van Grondelle, "The Role of Resonant Vibrations in Electronic Energy Transfer", *ChemPhysChem*, vol. 17, no. 9, pp. 1356–1368, 2016. DOI: 10.1002/cphc.201500965.

DOI:10.15774/PPKE.ITK.2018.009

[49] M. H. Lee and A. Troisi, "Vibronic enhancement of excitation energy transport: Interplay between local and non-local exciton-phonon interactions", *The Journal of Chemical Physics*, vol. 146, no. 7, p. 075 101, 2017. DOI: 10.1063/1.4976558.

[50] E. J. O'Reilly and A. Olaya-Castro, "Non-classicality of the molecular vibrations assisting exciton energy transfer at room temperature", *Nature Communications*, vol. 5, p. 3012, 2014. DOI: 10.1038/ncomms4012.

[51] V. Abramavicius and D. Abramavicius, "Excitation transfer pathways in excitonic aggregates revealed by the stochastic Schrödinger equation", *The Journal of Chemical Physics*, vol. 140, no. 6, p. 065 103, 2014. DOI: 10.1063/1.4863968.

[52] P. Nalbach, C. A. Mujica-Martinez, and M. Thorwart, "Vibronically coherent speed-up of the excitation energy transfer in the Fenna-Matthews-Olson complex", *Physical Review E*, vol. 91, no. 2, p. 022 706, 2015. DOI: 10.1103/PhysRevE.91.022706.

[53] Y. Fujihashi, G. R. Fleming, and A. Ishizaki, "Impact of environmentally induced fluctuations on quantum mechanically mixed electronic and vibrational pigment states in photosynthetic energy transfer and 2D electronic spectra", *The Journal of Chemical Physics*, vol. 142, no. 21, p. 212 403, 2015. DOI: 10.1063/1.4914302.

[54] X. Liu and O. Kühn, "Vibrational and vibronic coherences in the dynamics of the FMO complex", *Chemical Physics*, vol. 481, pp. 272–280, 2016. DOI: 10.1016/j.chemphys.2016.03.021.

[55] G. Hauska, T. Schoedl, H. Remigy, and G. Tsiotis, "The reaction center of green sulfur bacteria", *Biochimica et Biophysica Acta*, pp. 260–277, 2001.

[56] J. M. Olson, "The FMO protein", in *Discoveries in Photosynthesis*, Springer, 2005, pp. 421–427.

[57] A. Ben-Shem, F. Frolow, and N. Nelson, "Evolution of photosystem I - from symmetry through pseudosymmetry to asymmetry", *FEBS Letters*, vol. 564, no. 3, pp. 274–280, 2004. DOI: 10.1016/S0014-5793(04)00360-6.

[58] B. W. Matthews, R. E. Fenna, M. C. Bolognesi, M. F. Schmid, and J. M. Olson, "Structure of a bacteriochlorophyll a-protein from the green photosynthetic bacterium Prosthecochloris aestuarii", *Journal of molecular biology*, vol. 131, no. 2, pp. 259–285, 1979.

DOI:10.15774/PPKE.ITK.2018.009

[59] D. E. Tronrud, J. Wen, L. Gay, and R. E. Blankenship, "The structural basis for the difference in absorbance spectra for the FMO antenna protein from various green sulfur bacteria", *Photosynthesis Research*, vol. 100, no. 2, pp. 79–87, 2009. DOI: 10.1007/s11120-009-9430-6.

[60] D. M. Jonas, "Two-dimensional femtosecond spectroscopy", *Annual Review of Physical Chemistry*, vol. 54, no. 1, pp. 425–463, 2003. DOI: 10.1146/annurev.physchem.54.011002.103907.

[61] S. T. Cundiff and S. Mukamel, "Optical multidimensional coherent spectroscopy", *Physics Today*, vol. 66, no. 7, pp. 44–49, 2013. DOI: 10.1063/PT.3.2047.

[62] G. S. Schlau-Cohen, A. Ishizaki, and G. R. Fleming, "Two-dimensional electronic spectroscopy and photosynthesis: Fundamentals and applications to photosynthetic light-harvesting", *Chemical Physics*, vol. 386, no. 1-3, pp. 1–22, 2011. DOI: 10.1016/j.chemphys.2011.04.025.

[63] T. Brixner, J. Stenger, H. M. Vaswani, M. Cho, R. E. Blankenship, and G. R. Fleming, "Two-dimensional spectroscopy of electronic couplings in photosynthesis", *Nature*, vol. 434, pp. 625–628, 2005.

[64] M. Cho, H. M. Vaswani, T. Brixner, J. Stenger, and G. R. Fleming, "Exciton Analysis in 2d Electronic Spectroscopy", *The Journal of Physical Chemistry B*, vol. 109, no. 21, pp. 10 542–10 556, 2005. DOI: 10.1021/jp050788d.

[65] V. May and O. Kühn, *Charge and Energy Transfer Dynamics in Molecular Systems*, Third. Weinheim: Wiley-VCH Verlag GmbH & Co. KGaA, 2011.

[66] A. Ishizaki and G. R. Fleming, "Unified treatment of quantum coherent and incoherent hopping dynamics in electronic energy transfer: Reduced hierarchy equation approach", *The Journal of Chemical Physics*, vol. 130, no. 23, p. 234 111, 2009. DOI: 10.1063/1.3155372.

[67] M. Mohseni, P. Rebentrost, S. Lloyd, and A. Aspuru-Guzik, "Environment-assisted quantum walks in photosynthetic energy transfer", *The Journal of Chemical Physics*, vol. 129, no. 17, p. 174 106, 2008. DOI: 10.1063/1.3002335.

[68] H. Lee, Y.-C. Cheng, and G. R. Fleming, "Coherence Dynamics in Photosynthesis: Protein Protection of Excitonic Coherence", *Science*, vol. 316, no. 5830, pp. 1462–1465, 2007. DOI: 10.1126/science.1142188.

DOI:10.15774/PPKE.ITK.2018.009

[69] P. Huo and D. F. Coker, "Influence of environment induced correlated fluctuations in electronic coupling on coherent excitation energy transfer dynamics in model photosynthetic systems", *The Journal of Chemical Physics*, vol. 136, no. 11, p. 115 102, 2012. DOI: 10.1063/1.3693019.

[70] M. B. Plenio and S. F. Huelga, "Dephasing-assisted transport: Quantum networks and biomolecules", *New Journal of Physics*, vol. 10, no. 11, p. 113 019, 2008. DOI: 10.1088/1367-2630/10/11/113019.

[71] F. Caruso, A. W. Chin, A. Datta, S. F. Huelga, and M. B. Plenio, "Highly efficient energy excitation transfer in light-harvesting complexes: The fundamental role of noise-assisted transport", *The Journal of Chemical Physics*, vol. 131, no. 10, p. 105 106, 2009. DOI: 10.1063/1.3223548.

[72] A. Shabani, M. Mohseni, H. Rabitz, and S. Lloyd, "Numerical evidence for robustness of environment-assisted quantum transport", *Physical Review E*, vol. 89, no. 4, p. 042 706, 2014. DOI: 10.1103/PhysRevE.89.042706.

[73] F. Caruso, A. W. Chin, A. Datta, S. F. Huelga, and M. B. Plenio, "Entanglement and entangling power of the dynamics in light-harvesting complexes", *Physical Review A*, vol. 81, no. 6, p. 062 346, 2010. DOI: 10.1103/PhysRevA.81.062346.

[74] J. Wu, F. Liu, Y. Shen, J. Cao, and R. J. Silbey, "Efficient energy transfer in light-harvesting systems, I: Optimal temperature, reorganization energy and spatial–temporal correlations", *New Journal of Physics*, vol. 12, no. 10, p. 105 012, 2010. DOI: 10.1088/1367-2630/12/10/105012.

[75] M. Schmidt am Busch, F. Müh, M. E.-A. Madjet, and T. Renger, "The Eighth Bacteriochlorophyll Completes the Excitation Energy Funnel in the FMO Protein", *The Journal of Physical Chemistry Letters*, vol. 2, no. 2, pp. 93–98, 2011. DOI: 10.1021/jz101541b.

[76] C. Kreisbeck, T. Kramer, M. Rodríguez, and B. Hein, "High-Performance Solution of Hierarchical Equations of Motion for Studying Energy Transfer in Light-Harvesting Complexes", *Journal of Chemical Theory and Computation*, vol. 7, no. 7, pp. 2166–2174, 2011. DOI: 10.1021/ct200126d.

[77] V. M. Kenkre, A. Tokmakoff, and M. D. Fayer, "Theory of vibrational relaxation of polyatomic molecules in liquids", *The Journal of Chemical Physics*, vol. 101, no. 12, pp. 10 618–10 629, 1994. DOI: 10.1063/1.467876.

DOI:10.15774/PPKE.ITK.2018.009

[78] H. Fujisaki and J. E. Straub, "Vibrational energy relaxation in proteins", *Proceedings of the National Academy of Sciences*, vol. 102, no. 19, pp. 6726–6731, 2005.

[79] Á. Csurgay and K. Simonyi, *Az információtechnika fizikai alapjai: Elektronfizika*. Budapest: Mérnöktovábbképző Intézet, 1997.

[80] D. A. B. Miller, *Quantum Mechanics for Scientists and Engineers*. Cambridge: Cambridge University Press, 2008.

[81] H. Carmichael, *An Open Systems Approach to Quantum Optics*. Springer-Verlag, 1993.

[82] T. Geszti, *Kvantummechanika*. Budapest: Typotex, 2007.

[83] C. A. Brasil, F. F. Fanchini, and R. d. J. Napolitano, "A simple derivation of the Lindblad equation", *Revista Brasileira de Ensino de Física*, vol. 35, no. 1, 2013. DOI: 10.1590/S1806-11172013000100003.

[84] M. Fox, *Quantum optics: an introduction*, ser. Oxford master series in physics 15. Oxford ; New York: Oxford University Press, 2006.

[85] J. Jeske, D. J. Ing, M. B. Plenio, S. F. Huelga, and J. H. Cole, "Bloch-Redfield equations for modeling light-harvesting complexes", *The Journal of chemical physics*, vol. 142, no. 6, p. 064 104, 2015.

[86] A. Ishizaki and G. R. Fleming, "On the adequacy of the Redfield equation and related approaches to the study of quantum dynamics in electronic energy transfer", *The Journal of Chemical Physics*, vol. 130, no. 23, p. 234 110, 2009, 00296. DOI: 10.1063/1.3155214.

[87] Y. Tanimura, "Stochastic Liouville, Langevin, Fokker–Planck, and Master Equation Approaches to Quantum Dissipative Systems", *Journal of the Physical Society of Japan*, vol. 75, no. 8, p. 082 001, 2006, 00523. DOI: 10.1143/JPSJ.75.082001.

[88] B. Gobets and R. van Grondelle, "Energy transfer and trapping in photosystem I", *Biochimica et Biophysica Acta*, vol. 1507, no. 1, pp. 80–99, 2001.

[89] P. Atkins and R. Friedman, *Molecular quantum mechanics*, 4th. New York: Oxford University Press, 2005.

DOI:10.15774/PPKE.ITK.2018.009

[90] M. Schröter, S. D. Ivanov, J. Schulze, S. P. Polyutov, Y. Yan, T. Pullerits, and O. Kühn, "Exciton–vibrational coupling in the dynamics and spectroscopy of Frenkel excitons in molecular aggregates", *Physics Reports*, vol. 567, pp. 1–78, 2015. DOI: 10.1016/j.physrep.2014.12.001.

[91] J. R. Johansson, P. D. Nation, and F. Nori, "QuTiP: An open-source Python framework for the dynamics of open quantum systems", *Computer Physics Communications*, vol. 183, no. 8, pp. 1760–1772, 2012. DOI: 10.1016/j.cpc.2012.02.021.

[92] K. Yamanouchi, *Quantum Mechanics of Molecular Structures*. Berlin, Heidelberg: Springer-Verlag, 2012.

[93] J. R. Johansson, P. D. Nation, and F. Nori, "QuTiP 2: A Python framework for the dynamics of open quantum systems", *Computer Physics Communications*, vol. 184, no. 4, pp. 1234–1240, 2013. DOI: 10.1016/j.cpc.2012.11.019.

[94] J. Adolphs and T. Renger, "How Proteins Trigger Excitation Energy Transfer in the FMO Complex of Green Sulfur Bacteria", *Biophysical Journal*, vol. 91, no. 8, pp. 2778–2797, 2006. DOI: 10.1529/biophysj.105.079483.

[95] K. R. Shelly, E. A. Carson, and W. F. Beck, "Vibrational coherence from the dipyridine complex of bacteriochlorophyll a: Intramolecular modes in the 10-220-cm-1 regime, intermolecular solvent modes, and relevance to photosynthesis", *Journal of the American Chemical Society*, vol. 125, no. 39, pp. 11 810–11 811, 2003.

[96] E. Wientjes, H. v. Amerongen, and R. Croce, "Quantum Yield of Charge Separation in Photosystem II: Functional Effect of Changes in the Antenna Size upon Light Acclimation", *The Journal of Physical Chemistry B*, vol. 117, no. 38, pp. 11 200–11 208, 2013. DOI: 10.1021/jp401663w.

[97] J. Wang, D. C. Brune, and R. E. Blankenship, "Effects of oxidants and reductants on the efficiency of excitation transfer in green photosynthetic bacteria", *Biochimica et Biophysica Acta (BBA) - Bioenergetics*, vol. 1015, no. 3, pp. 457–463, 1990. DOI: 10.1016/0005-2728(90)90079-J.

[98] G. He, D. M. Niedzwiedzki, G. S. Orf, H. Zhang, and R. E. Blankenship, "Dynamics of Energy and Electron Transfer in the FMO-Reaction Center Core Complex from the Phototrophic Green Sulfur Bacterium *Chlorobaculum tepidum*", *The Journal of Physical Chemistry B*, vol. 119, no. 26, pp. 8321–8329, 2015. DOI: 10.1021/acs.jpcb.5b04170.

DOI:10.15774/PPKE.ITK.2018.009

[99] P. Rebentrost, M. Mohseni, I. Kassal, S. Lloyd, and A. Aspuru-Guzik, "Environment-assisted quantum transport", *New Journal of Physics*, vol. 11, no. 3, p. 033 003, 2009. DOI: 10.1088/1367-2630/11/3/033003.

[100] J.-L. Brédas, E. H. Sargent, and G. D. Scholes, "Photovoltaic concepts inspired by coherence effects in photosynthetic systems", *Nature Materials*, vol. 16, no. 1, pp. 35–44, 2017. DOI: 10.1038/nmat4767.

DOI:10.15774/PPKE.ITK.2018.009

Index

DOI:10.15774/PPKE.ITK.2018.009

DOI:10.15774/PPKE.ITK.2018.009